INFORMATION TO USERS

This manuscript has been reproduced from the microfilm master. UMI films the text directly from the original or copy submitted. Thus, some thesis and dissertation copies are in typewriter face, while others may be from any type of computer printer.

The quality of this reproduction is dependent upon the quality of the copy submitted. Broken or indistinct print, colored or poor quality illustrations and photographs, print bleedthrough, substandard margins, and improper alignment can adversely affect reproduction.

In the unlikely event that the author did not send UMI a complete manuscript and there are missing pages, these will be noted. Also, if unauthorized copyright material had to be removed, a note will indicate the deletion.

Oversize materials (e.g., maps, drawings, charts) are reproduced by sectioning the original, beginning at the upper left-hand corner and continuing from left to right in equal sections with small overlaps.

ProQuest Information and Learning
300 North Zeeb Road, Ann Arbor, MI 48106-1346 USA
800-521-0600

A MULTIMODALITY IMAGE FUSION AND LOCALISATION SYSTEM FOR RADIOSURGERY TREATMENTS OF ARTERIOVENOUS MALFORMATIONS

by

YANIC BERCIER

Medical Physics Unit
McGill University, Montreal
August 2000

A thesis submitted to the
Faculty of Graduate Studies and Research
in partial fulfilment of the requirements
of the degree of Master of Science

Abstract

A multimodality image fusion and localisation system for radiosurgery treatments of arteriovenous malformations (AVM) has been developed and validated. Within this system, three-dimensional magnetic resonance angiography (MRA) and two-dimensional digital subtraction angiography (DSA) vasculature information is combined with three-dimensional magnetic resonance (MR) and/or computed tomography (CT) anatomical information in order to benefit from the functionality of all modalities. MRA/MR/CT datasets are fused, and linked to the DSA images. The consistency of the linking procedure is verified by correlation of the DSA images with two-dimensional ray-traced projections of the MRA datasets. Organ contours are drawn on the MRA images, simultaneously visualised on their MR/CT counterparts, and projected onto the DSA images for visual feedback. This procedure allows users to incorporate both vascular and anatomical information in the three-dimensional target localisation and delineation process. Patient examples illustrating the utility of the system are presented.

Résumé

Un système de fusion d'images et de localisation pour traitements radio-chirurgicaux de malformations artériovéneuses (MAV) a été développé. Avec ce système, l'information vasculaire tri-dimensionnelle de la résonance magnétique angiographique (RMA) et bi-dimensionnelle de l'angiographie par soustraction digitale (ASD) est combinée à l'information anatomique tri-dimensionnelle de la résonance magnétique (RM) et/ou de la tomodensitométrie (TD) pour ainsi bénéficier de la fonctionnalité de tous les modalités. Les volumes RMA/RM/TD sont fusionnés, et liés aux images ASD. La cohérence de la liaison est vérifiée par corrélation des images ASD avec les images de projections bi-dimensionnelles à travers le volume de RMA. Les contours d'organes sont exécutés sur les images de RMA, visualisés simultanément sur leurs parties analogues des images de RM/TD, et projetés sur les images ASD pour rétroaction visuelle. Cette procédure permet aux usagers d'incorporer l'information anatomique et vasculaire pour le processus de localisation et de traçage de contours tri-dimensionnel. Des exemples de patients illustrent l'utilité du système.

Acknowledgements

I would like to express my sincere gratitude to Dr. Dimitre Hristov, my thesis supervisor, for his support, patience and invaluable insight throughout this research. He has provided an excellent blend of guidance and freedom that has allowed me to fulfil my thesis goals with great satisfaction. His help in preparing conference proceedings abstracts as well as this thesis has taught me much and is sincerely appreciated.

I would also like to thank Dr. Ervin Podgorsak for his consideration for and attention to graduate students of the Medical Physics Unit at McGill University. His door was always open to students with questions, concerns and suggestions.

I am also grateful to my colleagues at the Montreal General Hospital. In particular, I thank Philippe Belanger, for his computer expertise and friendship during the past two years. I also thank Horacio Patrocinio, for discussions on radiosurgery and assistance in the acquisition of phantom studies and Gennaro Durante, for discussions on MR and assistance in the acquisition of patient data. I would also like to thank Francois Deblois for his computer expertise, Dr. Tony Falco for his assistance in Chapter 3, and Alexandre Rioux for discussions and his friendship since the beginning of my undergraduate work. I also thank Margery Knewstubb for her administrative help in the past two years.

I would like to extend my thanks to Tania, my parents, and Karine for their patience and understanding in the past two years of my graduate work. I also thank Arie, Remy and Bart for their involvement in Quo Vadis.

Financial support for the research presented in this thesis was provided by the Medical Research Council of Canada and is also gratefully acknowledged.

List of Figures

Figure 1. Schematic diagram of an AVM (with modifications from [1]). The nidus is illustrated as the tangled conglomerate of vessels. 2

Figure 2. Principal mechanisms for neurologic symptoms of cerebral AVMs (with modifications from [2]). The AVM, illustrated in the middle, can induce a series of symptoms as pointed to by the arrows. 3

Figure 3. Percent incidence of symptoms of cerebral AVMs related to age at which they usually appear [2]. It can be seen that approximately 80% of all AVMs become symptomatic by the fourth decade of life. 4

Figure 4. Estimated rate of first appearance of symptoms correlated with the age at which they appear (with modifications from [2]). It can be seen that spontaneous bleeding is the most common symptom of AVMs peaking at approximately 25 years old. 5

Figure 5. Three steps of radiosurgery procedure. DSA projection geometry for target localisation (Step 1) is illustrated in (a) [33]. An MR image with isodose lines for treatment planning (Step 2) is shown in (b), along with the slice fiducial markers obtained from the MR compatible localiser box. Treatment delivery (Step 3) by LINAC is illustrated in (c) [33]. 8

Figure 6. Orthogonal projection DSA images. The non-contrast images (a) and (d), the contrast images (b) and (e) as well as the subtracted images (c) and (f) are illustrated. .. 10

Figure 7. Irregularly shaped AVMs [17]. AVM projections, as they would be seen on DSA images, contain insufficient information about their actual shapes. 11

Figure 8. CT scanning geometry (with modifications from [38]). As the x-ray tube and detector array rotate, samples are taken at different angles through the object and are employed to reconstruct the images. 12

Figure 9. TOF imaging physics. The slice to be imaged becomes saturated due to the application of many rapid RF pulses, as shown in (a). The saturated blood flows out of the slice as fresh bloods flows into it, as shown in (b). Another RF pulse is applied to which only the fresh blood responds, since the static tissue of the slice has remained saturated. 14

Figure 10. The Leksell stereotactic frame with posts and pins for head attachment. The convention for the coordinate system is depicted with the centre of the frame located at 100 mm from the origin along all three axes (with modifications from [53])....18
Figure 11. Four main modules of system....18
Figure 12. Leksell MR/CT localiser. The N-shaped bars on the localiser box are illustrated in (a). The frame space coordinates of vertical rods are given in (b)....20
Figure 13. Panel for fiducial marker selection. The nine fiducial markers can be observed on the image slice....21
Figure 14. MR/CT fiducial marker geometry. The relative position of the middle fiducial marker of the N-shaped bar cross-section between the vertical bars allows the determination of the image slice orientation within the coordinate system defined by the frame. P_1, P_2 and P_3 are the points of intersection of the image plane with the rods. A, B and C are the position of the points of intersection on the image. $Length_{bar}$ and $Separation_{bar}$ are the bar length and bar separation in frame space. V denotes the distance along the Z axis between the middle fiducial marker and the rod extremity. U denotes the distance along X or Y (depending on the localiser box face) between the middle fiducial marker and the rod extremity....22
Figure 15. Slice orientation in frame space before and after reformatting (interpolation). The image slices may be arbitrarily oriented in frame space due to subtle patient movement or scanning imperfections. After reformatting, a regular voxel array is obtained. For voxel (i,j,k), the nearest two slices which bracket the voxel are illustrated in dotted format. Points, which are not between two slices, are padded with zeros....23
Figure 16. Volume extent determination. The extent along the X and Y axes are determined by taking the intersection of the (X,Y) extents of all image slices within the dataset, illustrated in (a). The (X,Y) extent of an image slice, as shown by the shaded area in (b), is the interval between the maximum value of the two X_{min} values and the minimum value of the two X_{max} values, and similarly for the Y direction. The extent along the Z axis is obtained by the minimum and maximum z values of the dataset, as calculated from all the slices (a). The resulting volume extent is illustrated as the dashed rectangle in (a)....24
Figure 17. Reformatting extent determination. Illustrated in (a) are the volume extents of 2 datasets. The volume extents (dashed lines) as well as the reformatting extent (solid

line), obtained by taking the union of the two, are shown in (b). For each volume, interpolation is performed inside the volume extent (white) as shown in c) and d). The region of the reformatting extent which does not intersect the volume extent (black) is padded with zeros (c and d). 25

Figure 18. Interpolation procedure. The voxel intensity is obtained by interpolating between the slices that bracket the voxel. A bilinear interpolation is performed in order to get the image coordinate intensity for each slice. The voxel intensity is then determined by performing a linear interpolation along Z between the two image coordinate intensities, using the distances between the slices and the voxel....26

Figure 19. Leksell DSA localiser. The lead beads on the localiser box are illustrated in (a). A fifth bead, illustrated in shaded form, is found on the anterior plate as well as on the left plate for box face identification on the projection images. The frame space coordinates of the beads are given in (b)....28

Figure 20. Panel for fiducial marker selection. The eight fiducial markers can be observed on the projection image. 29

Figure 21. Perspective projection geometry. Of the eight points, the four obtained from the plate closest to the x-ray tube are more magnified than the four obtained from the plate on the opposite side....30

Figure 22. 3D target delineation. The user delineates the target on the MRA volume (a). The contours appear simultaneously in the MR volume (b). It can be seen that the vasculature is not visible on the MR dataset (b) yet is easily outlined with the help of the fused MRA (a). 33

Figure 23. Ray-tracing through the MRA volume. Employing the DSA projection geometry illustrated in (a), the ray-traced MRA images (b) are correlated with the DSA images (c). The correlation enables the examination of possible inconsistencies between the DSA datasets and the reformatted MRA volume which could arise from MR distortions, frame slippage during the imaging procedure or other sources of image artefacts. 34

Figure 24. Ray-tracing algorithm [59]. The intersection of the ray with the voxels are a subset of the intersections of the ray with the lines [59]. The intersections of the ray with the lines are given by two equally spaced sets: one set for the horizontal lines (filled circles) and one set for the vertical lines (open circles) [59]. 35

Figure 25. Projection geometry. XYZ represents the frame coordinate system. UVW represents the projection coordinate system, where (u,v) are the image coordinates of an image point and w = 0 defines the image plane. The source position is illustrated as point S. The distance between S and the image plane is denoted as f, the focal length. Each image point is the intersection of the image plane and the line connecting S and the corresponding frame point. 36
Figure 26. Geometry for the determination of the source position. 40
Figure 27. Determination of image plane orientation. 42
Figure 28. Determination of the piercing point. 43
Figure 29. Geometry for determination of scale factors. 45
Figure 30. Determination of rotation within the image plane. 46
Figure 31. Coordinate system transformation. The transformation between the frame coordinate system and the beam coordinate system must be provided in order to produce the radiographic image. The transformation accounts for translation, rotation and scaling between the referential systems and defines the beam source position and orientation. 48
Figure 32. Panel for 3D target localisation and delineation and contour correlation. The contours, which are drawn on the MRA (bottom left window), simultaneously appear on the MR (bottom right window) with the help of the 3D target localisation and delineation module. The 3D surface representation of the vasculature is removed when the contours are to be drawn (Figure 22). As the contours are drawn on the MRA, their projections simultaneously appear on the DSA images (top left and right), with the help of the DSA/MRA correlation module, which enables the correlation of the contoured volume with the target extent observable on the DSA images. The contours drawn on the MRA can be modified accordingly. 50
Figure 33. The 3D localisation process comparison between the developed system and the clinically used in-house treatment planning software [62, 63]. A prominent anatomical feature, shown in (a), shows good agreement between the in-house treatment planning software (b) and the developed system with both initial (c) and reformatted (d) images. 53
Figure 34. The 2D localisation process comparison between the developed system and the clinically used in-house treatment planning software [62, 63]. A prominent image

feature, shown in (a) and (b) by the solid arrows, shows good agreement between the in-house treatment planning software (c) and the developed system (d).....54
Figure 35. The positions of the fiducial markers on the image (a) and projected fiducial markers by ray-tracing (b). Since the DSA fiducial markers are user selected, additional errors are introduced in the SVD algorithm and matrix decomposition yielding an error of 1.8 pixels for the ray-tracing algorithm.....55
Figure 36. Phantom employed for the validation. The acrylic box, which was fixed to the stereotactic frame, contains an aluminium rod (solid arrow) as well as an air pocket (dashed arrow) as shown in (a). The air pocket and rod can be visualised on CT images, as shown in (b).....56
Figure 37. CT volume localisation comparison between the BrainScan software and the developed system. The rod tip and air pocket on the superior surface of the phantom are represented by the solid and dashed arrows respectively. The frame space coordinates of the rod tip and air pocket centre obtained with the BrainScan software (a and c) and the developed system for both the initial (b and d) and reformatted volumes (not shown) are in agreement within 1 mm.....57
Figure 38. Target localisation panel. The AP (left) and LAT (right) phantom x-ray projections are employed for conventional target localisation. The rod tip was localised at (109.0, 100.6, 65.4) mm.....58
Figure 39. Ray-traced CT images and x-ray projection images. The ray-traced AP (a,b) and LAT (c,d) images (solid arrows) correlate very well visually with the AP (a,b) and LAT (c,d) x-ray projection images (dashed arrows).....59
Figure 40. 3D target localisation and delineation panel. The contours (solid arrow) of the rod are drawn within the CT data (bottom left window) and may be simultaneously adjusted due to continuous feedback from the visual correlation of the contour projections (dashed arrows) with the target extent on the x-ray projection images (top left and right windows).....60
Figure 41. 3D target localisation and delineation panel. The contours (solid arrow) of the air pocket are drawn within the CT data (bottom left window) and may be simultaneously adjusted due to continuous feedback from the visual correlation of the contour projections (dashed arrows) with the target extent on the x-ray projection images (top left and right windows).....61

Figure 42. Target localisation panel. The AP (left) and LAT (right) DSA images are employed for conventional target localisation. 62

Figure 43. Fused MRA and MR volumes of a patient previously treated with the McGill radiosurgery technique employing only DSA and MR images for which the target was localised at (7.8, 8.1, 9.1) cm in frame space. The MRA coronal (a) and sagittal (b) images are shown with the corresponding MR coronal (c) and sagittal (d) images. The circles on the images illustrate the McGill technique treated volume. The actual treated volume in (a) and (b) seems to include healthy tissue which may be due to the limitations of the DSA localisation method, the treatment technique, or the combination of the two 63

Figure 44. Ray-traced MRA images and DSA images. The AP (a) and LAT (b) ray-traced images (solid arrows) correlate very well visually with the AP (a) and LAT (b) DSA images (dashed arrows) in the vicinity of the AVM. However, there are differences between the images since the modalities offer different vasculature information. The physician must take these considerations into account in the 3D target localisation and delineation process 64

Figure 45. 3D target localisation and delineation panel with probe and 3D vascular representation for patient 1. The MR and DSA images are shown in the bottom right and top windows respectively. The vasculature, shown in the bottom left window by the long-dashed arrow, is superposed onto the MRA images. A probe (solid arrow) guides the physician within the fused volumes by projecting its position (dashed arrows) onto the DSA images. The 3D vascular representation is removed for the contouring process 65

Figure 46. 3D target localisation and delineation panel. The contours, as well as their projections onto the DSA images, are represented by the solid and dashed arrows respectively. The MRA, MR and DSA images are shown in the bottom left, bottom right and top windows respectively. The contour projections correlate well with the AVM extent on the DSA images. Since the contours are drawn on each slice, the target volume is kept at a minimum. 66

Figure 47. Target localisation panel. The AP (left) and LAT (right) DSA images are employed for conventional target localisation. 67

Figure 48. Fused MRA and MR volumes of a patient previously treated with the McGill radiosurgery technique employing only DSA and MR images for which the target was localised at (7.7, 6.3, 9.3) cm in frame space. The MRA coronal (a) and sagittal (b) images are shown with the corresponding MR coronal (c) and sagittal (d) images. The circles on the images illustrate the treated volume by the McGill technique. The treated volume does not seem to include the entire lesion, which may be due to the limitations of the DSA localisation method, the treatment technique, or the combination of the two.....68

Figure 49. Ray-traced MRA images and DSA images. The AP (a) and LAT (b) ray-traced images (solid arrows) correlate very well visually with the AP and LAT DSA images (dashed arrows). There are differences between the images since the modalities offer different vasculature information. However, the ray-traced MRA images suggest a greater AVM volume. The physician will therefore take these considerations into account while drawing the contours. 69

Figure 50. 3D target localisation and delineation panel. The contours, as well as their projections onto the DSA images, are represented by the solid and dashed arrows respectively. The MRA, MR and DSA images are shown in the bottom left, bottom right and top windows respectively. The projected contours, which suggest a greater AVM volume than shown on the DSA images, may be adjusted in order to include the missing lesion portions from the actual treated volume.....70

TABLE OF CONTENTS

ABSTRACT I

RÉSUMÉ II

ACKNOWLEDGEMENTS III

LIST OF FIGURES IV

CHAPTER ONE 1

1 INTRODUCTION 1

1.1 ARTERIOVENOUS MALFORMATIONS 1

1.2 STEREOTACTIC RADIOSURGERY PROCEDURE FOR AVMS 7

1.3 AVM LOCALISATION 9

1.3.1 DSA *9*

1.3.2 CT/CTA *12*

1.3.3 MR *13*

1.3.4 MRA *14*

1.4 THESIS OBJECTIVES AND OUTLINE 15

CHAPTER TWO 17

2 MULTIMODALITY IMAGE FUSION FOR LOCALISATION 17

2.1 INTRODUCTION 17

2.2 VOLUME FUSION 19

2.2.1 FTM generation *19*

2.2.2 Volume reformatting *21*

2.3 DSA TARGET LOCALISATION 27

2.3.1 Projection geometry determination *27*

2.3.2 Target localisation *31*

2.4 3D TARGET LOCALISATION AND DELINEATION 32

2.5 DSA/MRA CORRELATION 33

2.5.1 Ray-tracing *33*

2.5.2 Contour projections *49*

2.6 SUMMARY 51

CHAPTER THREE **52**

3 APPLICATIONS **52**

3.1 INTRODUCTION 52
3.2 VALIDATION 52
3.3 PHANTOM EXAMPLE 55
3.3.1 CT localisation *55*
3.3.2 X-ray projection localisation *58*
3.3.3 Ray-tracing *59*
3.3.4 3D target localisation and delineation *60*
3.4 PATIENT 1 62
3.5 PATIENT 2 66
3.6 SUMMARY 69

CHAPTER FOUR **72**

4 SUMMARY AND FUTURE WORK **72**

4.1 SUMMARY 72
4.2 FUTURE WORK 73

REFERENCES **75**

Chapter One

1 Introduction

1.1 Arteriovenous Malformations

In the normal human circulation, the blood vessels originate from the heart and consist of a branching arrangement of arteries of continually decreasing size which feed into a capillary bed before exiting through small veins, which increase in size prior to returning to the heart. The capillary bed serves an important purpose. Its vascular resistance slows the flow of blood considerably to allow perfusion of oxygen and nutrients to surrounding tissue. One form of cerebrovascular disease is the arteriovenous malformation (AVM). In some cases, the vessels comprising the capillary bed of the brain become malformed during embryonic development and prohibit the opportunity for blood to properly perfuse into the surrounding tissue. Such malformations are termed *arteriovenous malformations* (AVMs).

There are three anatomic components of AVMs that are significant in understanding the anatomy and the treatment of the lesions: (1) the arterial feeders, (2) the nidus and (3) the venous outlow (Figure 1). The nidus represents the tangled conglomerate of weakened and enlarged capillary vessels which serve as direct shunts for blood flow between the high-pressure feeding arterial system and the low pressure draining venous system. The high flow shunting of blood within the AVM without an intervening capillary bed causes the fragile dilated vessels in the nidus to become structurally abnormal and fatigued, to enlarge further, and to possibly rupture. The size of an AVM, denoted as the maximum nidus diameter D,

ranges from 1 to 10 cm. Clinical descriptions of AVM size include small ($D < 3$ cm), medium ($3 < D < 6$ cm) and large ($D > 6$ cm) [1]. Small AVMs have been shown to rupture more frequently than larger AVMs.

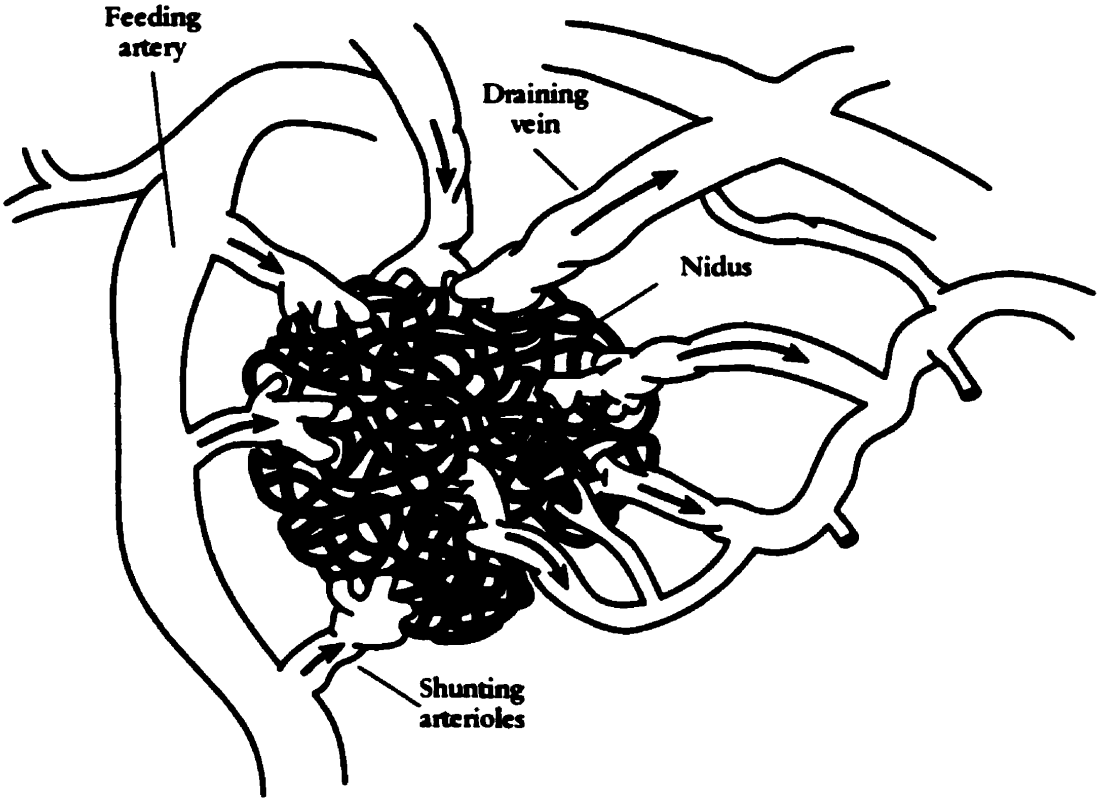

Figure 1. Schematic diagram of an AVM (with modifications from [1]). The nidus is illustrated as the tangled conglomerate of vessels.

AVMs are present in approximately 0.14% of the population [1, 2]. Small AVMs account for 30% of the afflicted population, medium AVMs account for 60% and large AVMs account for 10% [1]. Since AVMs differ in size, location and degree of shunting, the symptoms vary (Figure 2) and become clinically apparent at different ages (Figure 3, Figure 4). Spontaneous bleeding, or hemorrhage, is the most common symptom of AVMs (50%), after which are seizures (25%) [3]. The annual risk of AVM hemorrhage is from 2 to 4% per year [4]. Once

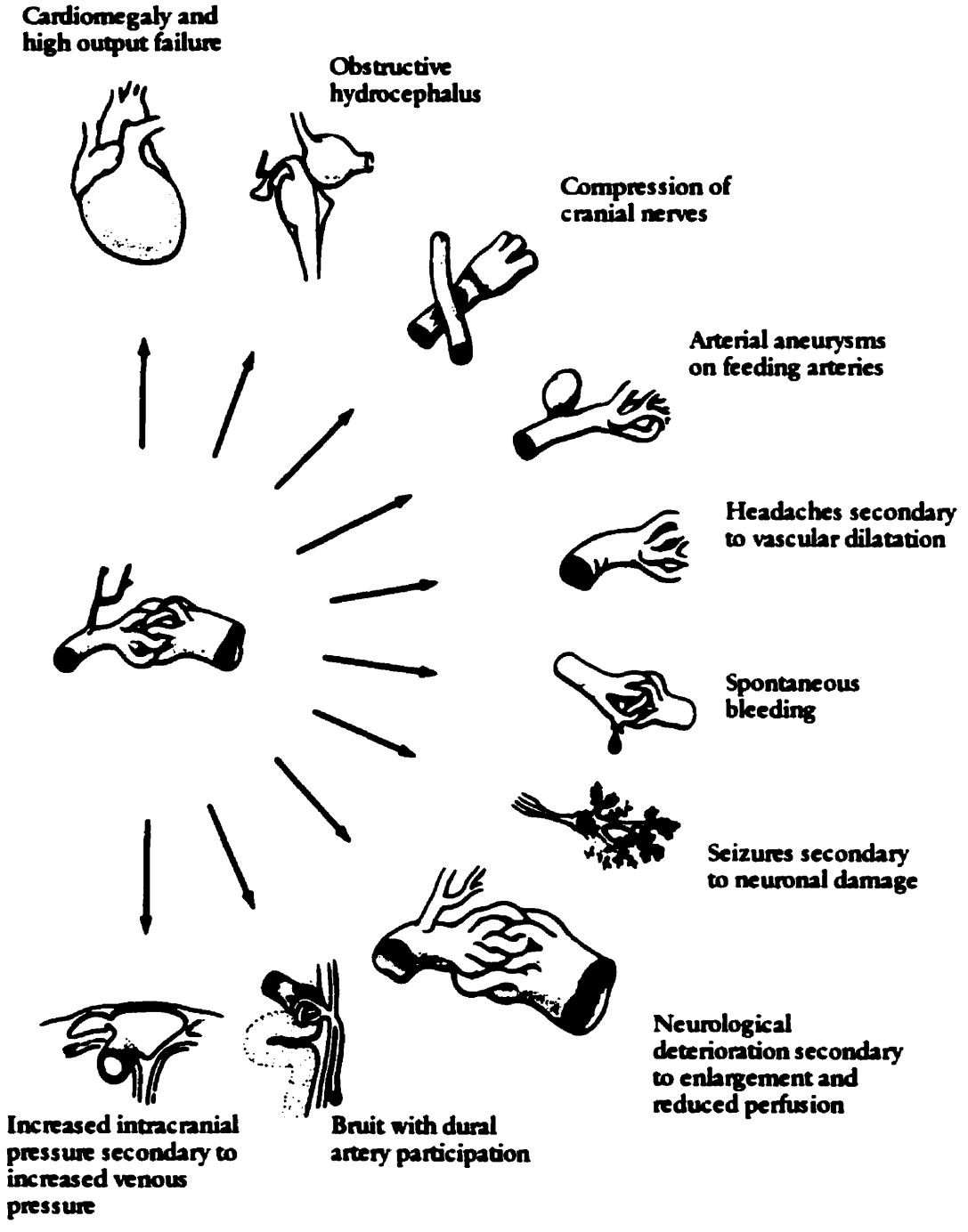

Figure 2. Principal mechanisms for neurologic symptoms of cerebral AVMs (with modifications from [2]). The AVM, illustrated in the middle, can induce a series of symptoms as pointed to by the arrows.

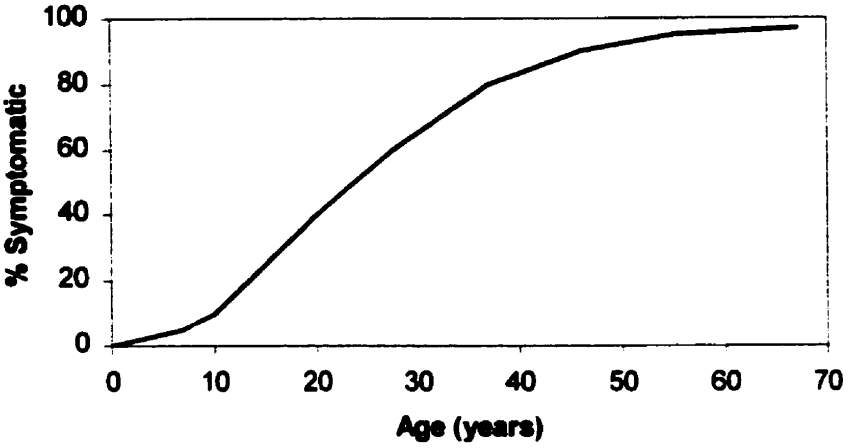

Figure 3. Percent incidence of symptoms of cerebral AVMs related to age at which they usually appear [2]. It can be seen that approximately 80% of all AVMs become symptomatic by the fourth decade of life.

the AVM has bled, the annual risk of recurrent hemorrhage increases to 6% for the first year and increases 2% yearly for subsequent years [2]. Approximately 80% of all AVMs become symptomatic by the end of the fourth decade of life [2]. AVMs pose a significant risk and represent a major life threat when left untreated [3]. A long-term follow-up of persons without interventions indicates a mortality rate of 17% to 19% and a severe disability rate of 20% to 29% over a 15 year to 20 year period [3].

The main objective in treating AVMs is to remove the AVM completely and permanently [3, 5] in a way that (1) the threat of intracranial hemorrhage is eliminated, (2) neurological function is preserved and (3) complications from the treatment are avoided [6]. The three major modalities for the treatment of AVMs are surgery, endovacular embolisation and stereotactic radiosurgery (SR) [5].

In surgery, the first step in the resection of the lesion is the identification of the major arterial feeders [1]. Once the feeders are identified, the surgeon carefully dissects around the volumetric boundary of the AVM, isolating the lesion from the normal brain [1]. Surgery has the advantages of immediate protection from the risk of hemorrhage [6] and cure rates

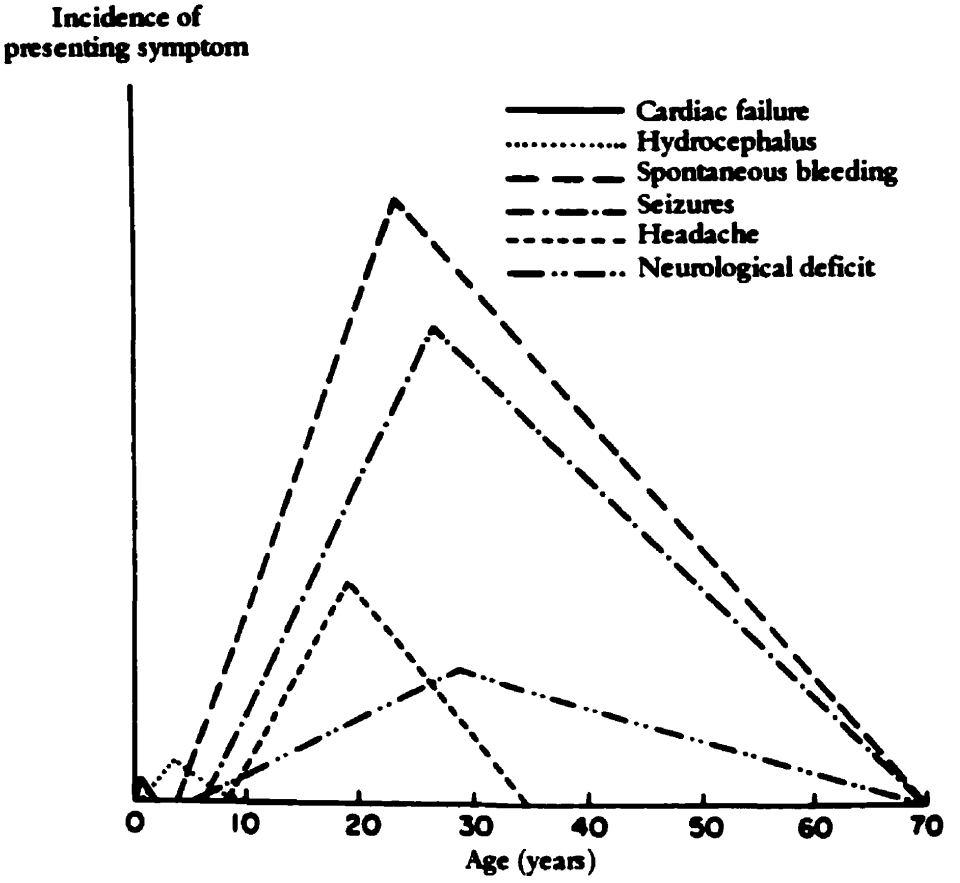

Figure 4. Estimated rate of first appearance of symptoms correlated with the age at which they appear (with modifications from [2]). It can be seen that spontaneous bleeding is the most common symptom of AVMs peaking at approximately 25 years old.

generally exceeding 95% for small AVMs [7]. However, the disadvantages remain the invasiveness of the procedure [8], the possibility of immediate complications [8], the need of general anesthesia and a lengthy recovery time [1]. The risk of treatment-related morbidity is of the order of 5% and mortality of the order of 1% [7]. For reasons including inaccessibility, size, and patient safety, some AVMs, particularly large AVMs, cannot be removed surgically and must therefore be managed by embolisation or radiosurgery.

The role of embolisation in the treatment of AVMs is reserved for problematic AVMs not readily accessible by surgery or that pose a high risk to patient safety [1]. In embolisation, a

chemical or mechanical agent (embolic agent) is delivered to the AVM via the arterial feeders in an attempt to occlude the nidus and redirect blood flow to normal adjacent regions of the brain. The embolic agents, such as silicon spheres, balloons, polyvinyl alcohol, microcoils and acrylic glue [9] are selectively injected via an arterial feeder and permeate a nidus volume dependent on the agent volume, injection pressure and arterial flow [1]. Embolisation procedures have morbidity rates of approximately 11% and mortality rates of approximately 3.5% [3]. Some complications occur at the time of embolisation and are the result of occlusion of normal vessels by the embolic material, while others, such as hemorrhages, occur after a delay of hours to days after embolisation [3]. Unfortunately, total obliteration of the nidus is seldom achieved [3, 5] since the nidus of most AVMs contain portions that are fed by arteries not amenable to embolisation [3]. Thus, this technique is mostly performed to reduce the size or flow of the AVM in preparation for surgery or radiosurgery [3, 5].

Stereotactic radiosurgery, which is a non-interventional approach to AVM therapy [6], is a brain irradiation technique in which narrow beams of ionising radiation are focused onto a small, stereotactically localised target [10]. Its goal is to deliver a single high radiation dose to the target volume, without affecting the surrounding brain tissues [11, 12]. Successful radiosurgery requires accurate target volume determination, accurate spatial dose delivery in the target volume and a very sharp dose fall-off in regions outside the target [1, 11]. The technique is particularly useful in the treatment of areas of the brain which are inaccessible by conventional surgical means [10]. For AVMs which are situated in deep brain locations such as close to the brain stem or near critical organs such as the visual cortex, radiosurgery is especially useful due to its non-invasiveness [4]. The goal for radiosurgical treatment of AVMs is to produce an inflammatory reaction in the vessel walls of the malformation [1]. This reaction is initialised by the delivered high radiation dose which must conform to the nidus volume and exclude the adjacent draining veins and feeding arteries, keeping the target volume at a minimum [4]. Radiation injury to the AVM vessels, produced by the localised deposit of the large amount of energy into the lesion's tissue [1], causes endothelial cell damage and proliferation which leads to obliteration of the AVM [1, 4]. Complete AVM obliteration is obtained when blood flow through the AVM has ceased [1]. Radiosurgery has virtually no morbidity or disruption of the patient's life [13]. High cure rates of approximately 80% [7, 13] as well as low neurological complications of the order of 2% have been reported [13].

However, this treatment modality is progressive, indicating complete obliteration generally occurring over a latency interval of two to three years [6, 13]. Causes for incomplete AVM obliteration after radiosurgery include poor visualisation at the time of radiosurgery, which may be due to incomplete angiography [4], improper assessment of the 3D AVM shape [14, 15] as well as insufficient radiation dose delivered to the target volume [4].

1.2 Stereotactic radiosurgery procedure for AVMs

There are three main steps in the radiosurgery procedure. The first step of AVM radiosurgery is the target localisation. Conventional stereotactic angiography, or digital subtraction angiography (DSA), has been the routine method for AVM localisation [16], as well as for the determination of the nidus diameter [17]. Recent studies of other techniques for cerebral vascular disease localisation include the use of magnetic resonance angiography (MRA) [12, 18-22] and computed tomography angiography (CTA) [23-27] and indicate promising results. Most studies indicate that both modalities give insufficient results to be used alone [20, 22, 24] and give complementary information [26] which, particularly for large lesions, should be employed as a complement to DSA [12, 18, 25]. However, some centres, such as the University of Wisconsin Hospital and Clinics, no longer routinely perform stereotactic DSA before AVM radiosurgery but instead employ MRA for target localisation [12]. During all imaging and treatment procedures, a rigid frame is fixed to the patient's head establishing a coordinate system employed for the determination of the AVM position. A series of fiducial marker plates, to be attached to the frame during imaging, exist for each modality in order to determine the frame position within the datasets. Figure 5a illustrates the DSA projection geometry with the frame and localiser box.

In addition to target localisation, critical structures are localised and delineated with magnetic resonance (MR) and/or computed tomography (CT). A common method to critical structure localisation and delineation is to anatomically fuse MR to CT [28-32] in order to combine the data in a common image space. The CT volume data, employed for dose distribution calculations, is acquired with the localiser box and fused with the anatomy information provided by the MR data.

After the target and critical structures have been properly localised, the treatment planning

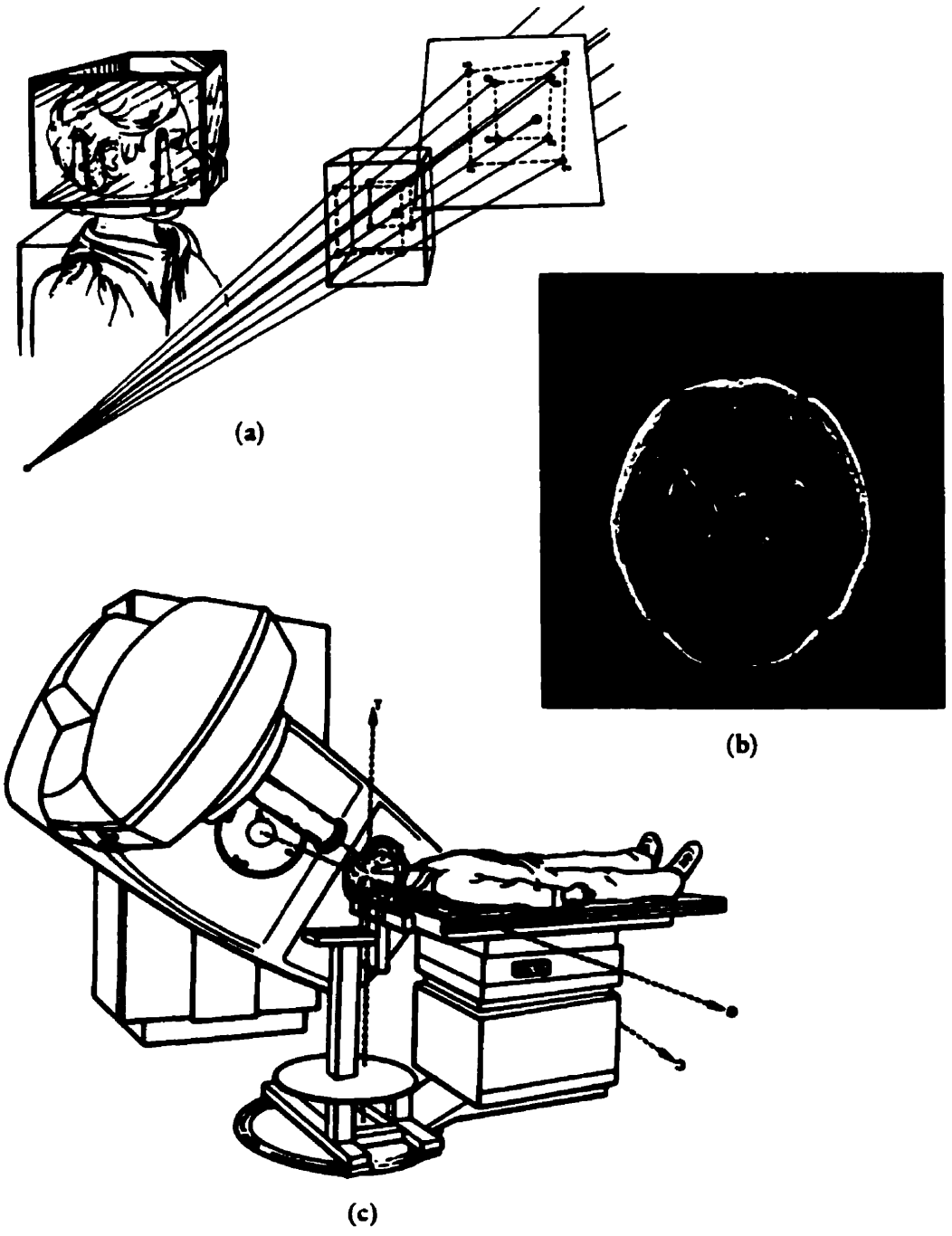

Figure 5. Three steps of radiosurgery procedure. DSA projection geometry for target localisation (Step 1) is illustrated in (a) [33]. An MR image with isodose lines for treatment planning (Step 2) is shown in (b), along with the slice fiducial markers obtained from the MR compatible localiser box. Treatment delivery (Step 3) by LINAC is illustrated in (c) [33].

follows. The planning is conventionally accomplished with the use of MR and/or CT datasets also acquired with the frame and modality compatible localisers. MR is particularly useful in relating the AVM to the surfaces of the brain, the ventricular system and anatomic regions of the brain such as critical organs [3]. The surfaces of the brain are employed for the determination of the AVM depth within the brain in order to calculate dose distributions. The isodose lines of the radiation distribution are employed to evaluate the effect of the plan on organs at risk near the target, which are visible on the MR and/or CT images (Figure 5b).

The final step of AVM radiosugery involves the delivery of the radiation dose. The major devices include the linear accelerator (LINAC) and the gamma knife unit [34] which deliver x-rays and ^{60}Co gamma rays respectively [3]. In the case of LINAC beam delivery, the patient is immobilised on the treatment couch with the use of the frame, with the target at the LINAC's isocentre (Figure 5c). Each technique, which currently include multiple non-coplanar converging arcs, dynamic stereotactic radiosurgery and conical rotation, is characterised by a particular set of individual rotational motions of the LINAC gantry and the couch from given start to given stop angles [34]. In the case of gamma knife beam delivery, the frame is secured into an appropriate collimator helmet and immobilising assembly. The couch, which advances the patient into the unit at the start of the irradiation, is retracted once the treatment time has elapsed [34].

1.3 AVM Localisation

A crucial step of the radiosurgery procedure is the localisation of the AVM. As mentioned previously, the modality most widely used for localisation is DSA. However, CT/CTA and MR/MRA have adjunct roles because they can each offer their own unique features not present in DSA.

1.3.1 DSA

The necessary information for localisation with DSA images is obtained by performing two x-ray projections. The procedure starts by taking a radiograph, for each projection, called the non-contrast image (Figure 6). Selected contrast images demonstrating the arterial and venous phases of the AVM [27], which are obtained by injecting a contrast media agent into the patient, are chosen for subtraction from corresponding non-contrast images (Figure 6). The

location and diameter of the nidus are then determined, with the use of the orthogonal subtraction images, by a multidisciplinary medical team.

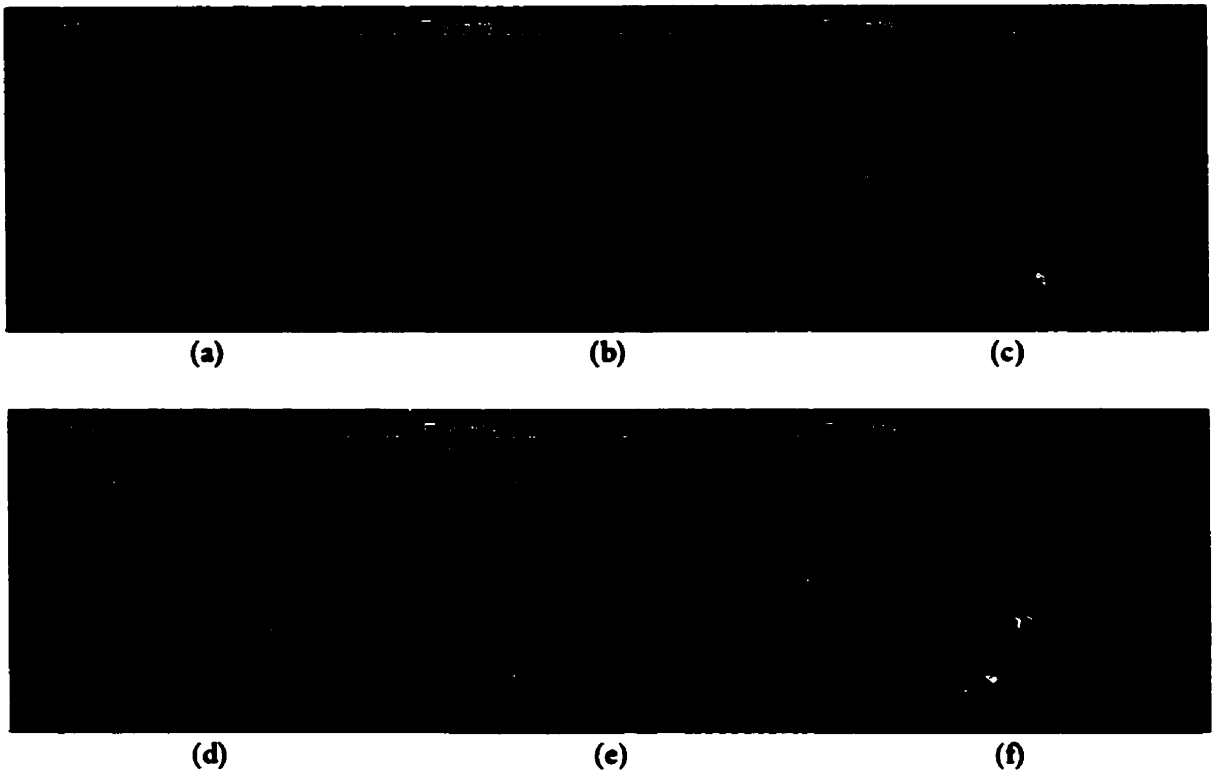

Figure 6. Orthogonal projection DSA images. The non-contrast images (a) and (d), the contrast images (b) and (e) as well as the subtracted images (c) and (f) are illustrated.

For small, spherically shaped AVMs, the modality is generally quite reliable for the delineation of the nidus [27] with anterior-posterior (AP) and lateral (LAT) projections. DSA also provides useful information regarding the distribution of arterial feeding vessels and the venous drainage pattern [27]. However, since this modality presents 2D projections of 3D shapes, there are certain limitations with regard to the determination of the three-dimensional shape of large, complexly shaped or obliquely oriented AVMs [4, 12, 16, 17, 27, 35, 36], as shown in Figure 7. Another disadvantage is the invasiveness of the modality, which demands more medical personnel for the imaging. Significant changes in the target delineation can also occur since the images of the nidus on the different projections are not simultaneous [17]. It is also difficult to delineate the feeding arteries, the nidus and the draining veins precisely, since

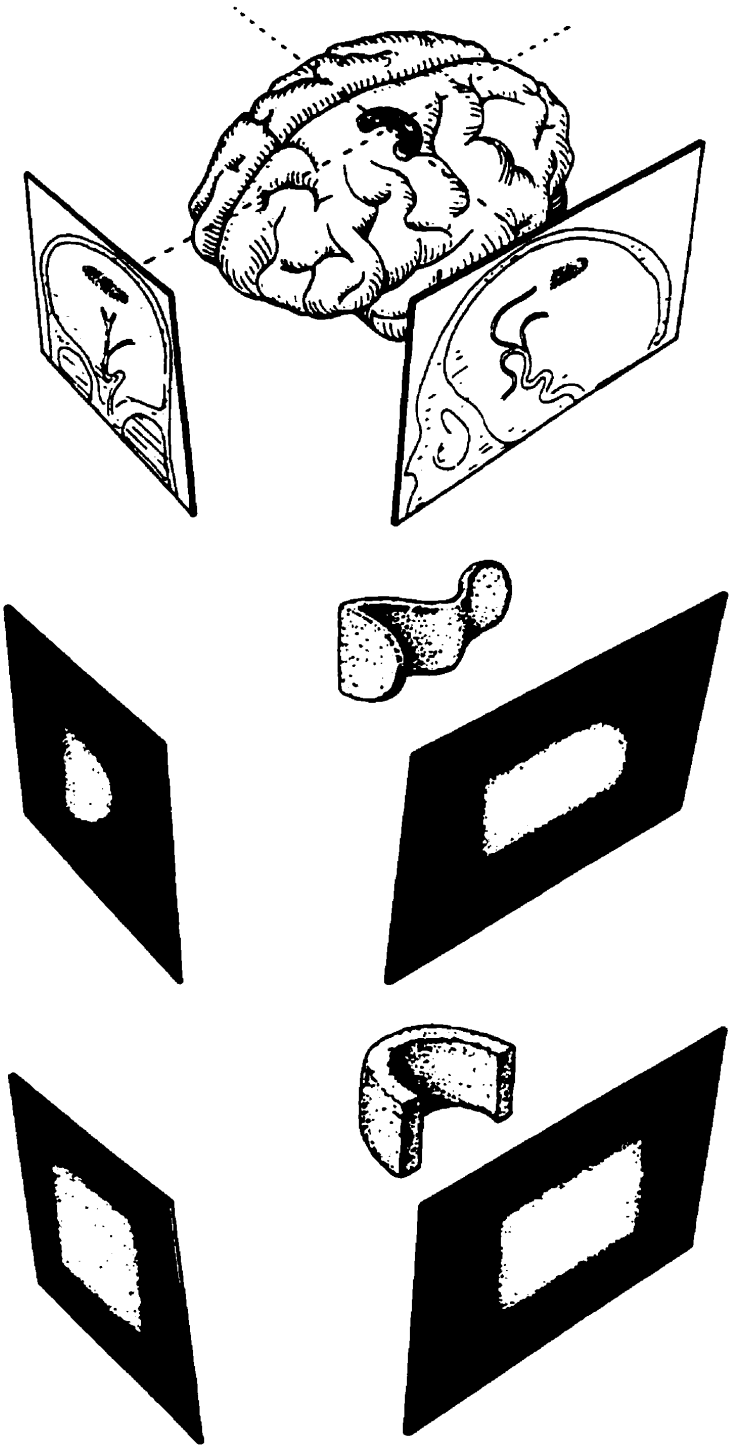

Figure 7. Irregularly shaped AVMs [17]. AVM projections, as they would be seen on DSA images, contain insufficient information about their actual shapes.

they frequently fill with the contrast agent almost simultaneously and since they can overlap on the projected angiographic images [17]. The incomplete information of the DSA images would usually result in a treatment plan that would irradiate tissue which should not be irradiated, or vice-versa (Figure 7).

1.3.2 CT/CTA

Another AVM localisation modality is CT. Contrary to conventional x-ray projection systems, CT provides cross-sectional tomographic images of an object. These images, which are reconstructed from x-ray projections taken at several different angles through the desired object slice as illustrated in Figure 8, produce a volumetric representation of the object linear attenuation coefficient [37].

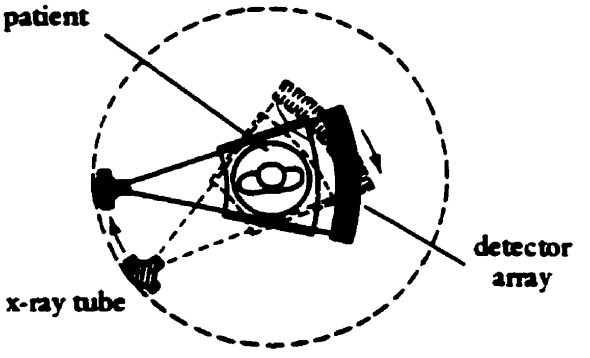

Figure 8. CT scanning geometry (with modifications from [38]). As the x-ray tube and detector array rotate, samples are taken at different angles through the object and are employed to reconstruct the images.

Helical x-ray CT with rapid injection of contrast medium and angiographic reconstruction (CTA) is a recently developed technique [26]. The technique involves a scout scanning which is subtracted from the contrast scanning to produce angiographic data. An advantage of this modality over conventional angiography (DSA) is the 3D information obtained which may be useful for large complexly shaped AVMs. CTA also has several advantages over MRA which include shorter scanning times, lower cost, better depiction of slower flow nidus and veins and

availability for patients for whom MR is contraindicated [26]. CTA, contrary to DSA, lacks temporal information, which is a major drawback [26]. It also involves longer post-processing time and fails to detect certain feeding arteries, presumably due to their smaller diameter compared to veins [26]. Another drawback to CTA is the invasiveness of the technique, which demands more medical personnel for the imaging.

1.3.3 MR

MR uses exterior magnetic fields, both static and in the form of gradients, and excitation radio-frequency (RF) pulses to image objects. As the magnetic field selects the slice to be imaged, RF pulses excite individual magnetised protons within the selected slice [37]. This excitation causes transitions between the nuclear spin states of the protons of the excited system [37, 39]. The system returns to equilibrium at a negative exponential rate by emitting electromagnetic quanta, the number of which is proportional to the amount of excited protons in the sample [37]. These quanta, which are detected by RF antennas, are the sampling signals employed to reconstruct MR images [37]. The reconstructed images are a function of proton density and tissue relaxation times [40] instead of linear attenuation coefficient as in x-ray modalities.

The major advantage of MR, when compared to CT, is its superior ability to differentiate and characterise soft tissues [40]. MR also has the advantage of imaging in the axial, sagittal or coronal slice orientation, unlike CT which is limited to axial images. Since there is no ionising radiation involved, no radiation dose is given to the patient. The disadvantages include longer sampling times with respect to CT as well as long post-processing times. MR is not involved in the localisation of AVMs but is particularly useful in relating the AVM to the surfaces of the brain, the ventricular system and anatomic regions of the brain such as critical organs [3]. However, MRI may yield inaccurate spatial information which may result from (1) system-related distortions, such as magnetic field inhomogeneities or gradient field nonlinearities, and (2) object-induced distortions, such as magnetic susceptibility and chemical shift artefacts [40-42] which are unique for every session [43]. Distortion effects and geometric shifts of a few millimeters have been reported [44-46]. Concerns about the geometric fidelity of MR have led to the development of distortion correction methods [42, 43, 47, 48] which have reduced global shifts to approximately 0.5 to 1 mm [41]. These distortions must be taken into consideration when imaging with this modality.

1.3.4 MRA

MRA is an MR application which provides volumetric vascular data sets allowing 3D visualisation and localisation. The time-of-flight (TOF) is non-invasive technique which is based on the inflow/outflow effect [49]. The MRA acquisition begins by applying many rapid RF pulses [49] that, due to the negative exponential rate of the system returning to equilibrium [39], cause the rate at which nuclei return to a steady state to decrease with each RF pulse. With fewer quanta being emitted, saturation occurs in which sampling becomes minimal [12, 50]. The flowing blood, which is also saturated, moves out of the imaging plane and fresh blood now flows into the slice [12, 50]. Another RF pulse is then triggered and a signal is received originating mostly from the fresh blood which moved into the imaging plane since the rest of the static tissue of the slice has remained saturated [12, 50] (Figure 9). The signal received, which increases with the amount of fresh blood, therefore augments as blood flow velocity increases [12, 49, 50].

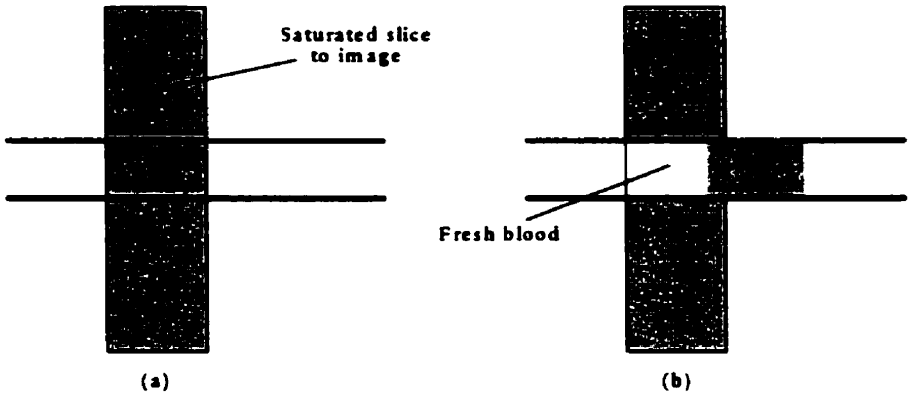

Figure 9. TOF imaging physics. The slice to be imaged becomes saturated due to the application of many rapid RF pulses, as shown in (a). The saturated blood flows out of the slice as fresh bloods flows into it, as shown in (b). Another RF pulse is applied to which only the fresh blood responds, since the static tissue of the slice has remained saturated.

There are two types of TOF imaging, the first being 3D TOF and the second being 2D TOF. The 3D TOF technique, which corresponds to volumetric acquisition, excites thick slabs of tissue to produce thin slices and therefore small voxels [50]. Volumetric sampling provides high resolution with good signal-to-noise ratio (SNR) ideal for looking at small vessels [50] and

fast flow [12], such as the nidus and the feeding arteries of the AVM [12, 16]. The 2D TOF technique, which involves multiple 2D acquisitions, employs slices that are thin compared to the 3D slab thickness but are relatively thick compared to the effective 3D slice thickness [50]. Despite the poor SNR due to the thin sequential 2D slices, 2D TOF produces maximal flow/stationary tissue contrast in each slice [50]. The method is suited for acquiring data over a long segment of vessel without saturation effects and for the investigation of slow flow [50], which is particularly useful for the definition of the large draining veins of the AVM [16].

An advantage of the TOF technique over conventional angiography (DSA) is the 3D information obtained which may be useful for large complexly shaped AVMs [26]. It also has several advantages over CTA such as the non-invasiveness of the technique and the ability to image a volume in axial, sagittal and coronal orientation. Since no x-rays are involved, no dose is delivered to the patient. However, MRA lacks temporal information, which is uncharacteristic of the DSA images [26]. Since the anatomical data of MR and the vascular data of MRA provide important complementary information, MR techniques have assumed a growing role in AVM treatment planning [12].

1.4 Thesis objectives and outline

The aim of this project was to develop a multimodality image fusion system for radiosurgery localisation of large AVMs in order to benefit from the functionality of all imaging modalities. The objectives were:

I. To design a tool for fusion of 3D datasets (MRA/CTA & MR/CT) in order to combine vascular and anatomical information. The fusion is to be based on fiducial markers due to the simplicity of this method. Head contours are needed for radiosurgery planning and image fusion makes the data of all these techniques available for localisation and planning.

II. To develop a tool to simulate projections through the 3D datasets described in I above employing the projection geometry of the x-ray angiograms. A comparison between the numerically projected 2D images and the x-ray angiograms, as well as the projection of the contours drawn on the MRA dataset onto the angiograms, provide a

visual check of potential errors that may be introduced during MRA localisation and definition of the AVM.

III. To evaluate the utility of the system by pursuing patient studies.

The thesis is organised as follows.

Chapter one has given an introduction on AVMs and stereotactic radiosurgery. Localisation imaging modalities for AVMs were also discussed.

In the second chapter, the developed system tools are presented. The system consists of four modules: (1) Volume fusion, (2) DSA target localisation, (3) 3D target localisation and delineation and (4) DSA/MRA correlation. The Volume fusion module fuses the MRA and MR/CT volumes. The DSA target localisation module determines the projection geometry and target position from a pair of DSA images. The next module performs 3D target localisation and delineation within the fused volumes with feedback from the DSA/MRA correlation module, which simultaneously projects the contours onto the DSA images. The DSA/MRA correlation module is also responsible for visual correlation of MRA and DSA data by ray tracing through the MRA volume.

Chapter three validates the developed system tools and presents a phantom example to validate the entire procedure for both the image acquisition and the software. Clinical examples of patients which have previously undergone radiosurgery and that have been planned with the McGill dynamic arc radiosurgery technique employing DSA and MR images are presented by comparing the conventional target localisation method to the 3D target localisation and delineation.

The fourth chapter concludes the thesis by summarising as well as discussing future work.

Aspects of this work have been published in conference proceedings [51, 52].

Chapter Two

2 Multimodality Image Fusion for Localisation

2.1 Introduction

This chapter presents the developed system for multimodality image fusion for radiosurgery localisation of large AVMs. The system is implemented with the AVS 5.4 software (Advance Visual System Inc., Waltham, MA) running on a Pentium II processor (Intel Corporation, Santa Clara, CA) 400 MHz with 256 Megs of RAM. The operational system employed is Red Hat Linux 6.0 (Red Hat Software Inc., North Carolina). The AVS software permits the programming of modules for specific tasks, which are then linked together in networks to complete application programs.

The system supports the Leksell stereotactic coordinate system commonly used for radiosurgery. This coordinate system, which is established by fixing a rigid frame to the patient's head during all imaging procedures and the radiosurgery treatment (Figure 10), identifies all points within the frame coordinate space. The frame also provides a rigid base for immobilisation of the patient during imaging and treatment procedures. Fiducial marker plates exist for each modality and are attached to the frame during imaging in order to determine the frame position within the datasets.

The four main modules of the system are illustrated in Figure 11. The Volume fusion module fuses the MRA and MR/CT volumes. The DSA target localisation module determines the

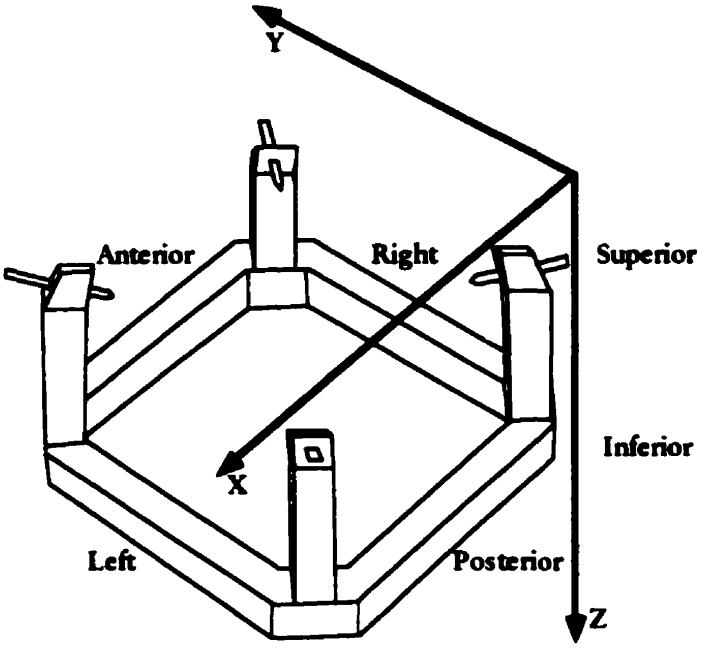

Figure 10. The Leksell stereotactic frame with posts and pins for head attachment. The convention for the coordinate system is depicted with the centre of the frame located at 100 mm from the origin along all three axes (with modifications from [53]).

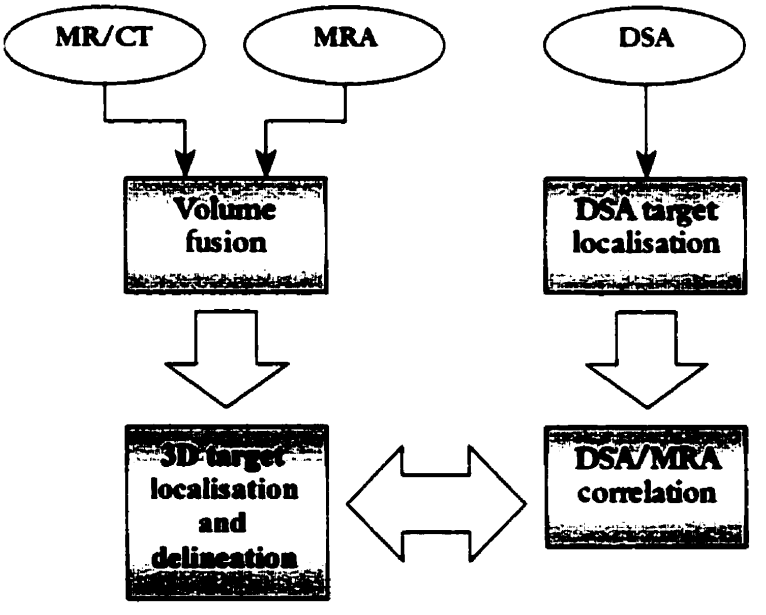

Figure 11. Four main modules of system.

projection geometry and target position from a pair of DSA images. The next module performs 3D target localisation and delineation within the fused volumes with feedback from the DSA/MRA correlation module which simultaneously projects the contours onto the DSA images. In addition, the DSA/MRA correlation module also allows correlation of MRA and DSA data by ray tracing through the MRA volume and overlaying the DSA and ray-traced MRA projection images.

2.2 Volume fusion

In order to fuse the MRA and MR/CT data, the volume fusion module first generates frame transformation matrices (FTMs) and then reformats the MRA and MR/CT volumes in the common stereotactic frame space defined by the stereotactic frame.

2.2.1 FTM generation

The CT and MR localisers contain a set of N-shaped bars (Figure 12a). The frame space coordinates of the vertical rods are given in Figure 12b. The N-shaped bars, when imaged axially, give three collinear image points. With three bars on each frame attachment, nine points are obtained on each image (Figure 13). The nine markers are selected by the user and are defined in image space coordinates as (u_i,v_i).

The 3D frame space coordinates (x_i,y_i,z_i) of the middle fiducial marker of each N-shaped bar cross-section are determined using ratios with respect to the extremity markers (Figure 14). The frame space coordinates of the three middle fiducial markers (x_1,y_1,z_1), (x_2,y_2,z_2), (x_3,y_3,z_3), along with their corresponding image coordinates (u_1,v_1), (u_2,v_2), (u_3,v_3) are used to determine the frame transformation matrix (FTM). The FTM, which is specific to each slice, is obtained by equation (1) [54]. FTM_i allows the determination of the frame space coordinates (x,y,z) corresponding to the image space coordinates (u,v) of slice i by equation (2) [54].

$$\mathbf{FTM} = \begin{bmatrix} u_1 & v_1 & 1 \\ u_2 & v_2 & 1 \\ u_3 & v_3 & 1 \end{bmatrix}^{-1} \begin{bmatrix} x_1 & y_1 & z_1 \\ x_2 & y_2 & z_2 \\ x_3 & y_3 & z_3 \end{bmatrix} \tag{1}$$

$$\begin{bmatrix} x & y & z \end{bmatrix} = \begin{bmatrix} u & v & 1 \end{bmatrix} \cdot \mathbf{FTM} \tag{2}$$

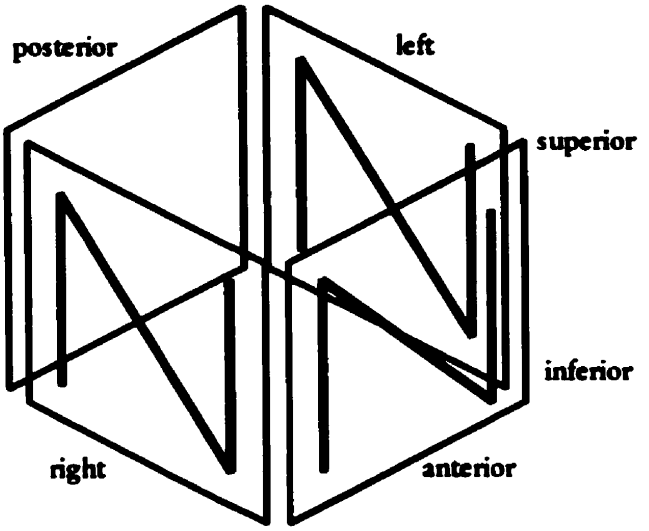

(a)

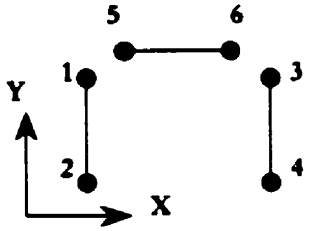

Inferior view

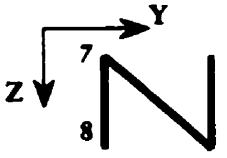

Lateral view

Point	x (mm)	y (mm)	z (mm)
1	5	160	---
2	5	40	---
3	195	160	---
4	195	40	---
5	40	215	---
6	160	215	---
7	---	---	40
8	---	---	160

(b)

Figure 12. Leksell MR/CT localiser. The N-shaped bars on the localiser box are illustrated in (a). The frame space coordinates of vertical rods are given in (b).

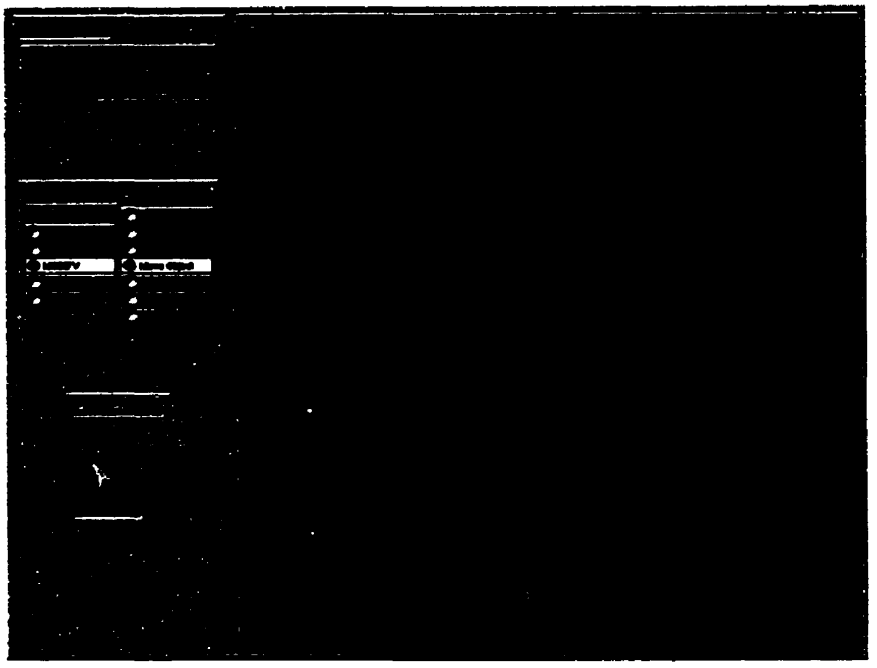

Figure 13. Panel for fiducial marker selection. The nine fiducial markers can be observed on the image slice.

2.2.2 Volume reformatting

After the FTM determination, the MRA and MR/CT volumes are reformatted and fused in frame space. This is necessary because subtle patient movements or scanning imperfections may lead to changes in the mutual orientation of image slices, as shown in Figure 15. Furthermore, reformatting is necessary to obtain the regular voxel array required for ray-tracing in the MRA/DSA correlation module. The reformatting procedure is as follows.

1. Volume extent determination. A frame space volume extent is determined for each dataset.

2. Reformatting extent determination. The volume extents of the datasets are then compared to determine a common reformatting extent, in order to proceed with the interpolation.

3. Interpolation. The volumes are reformatted within the reformatting extent.

For each dataset, the extent along the X and Y axes are determined by taking the interval intersection of the (X,Y) extents of all image slices within the dataset (Figure 16a). The (X,Y)

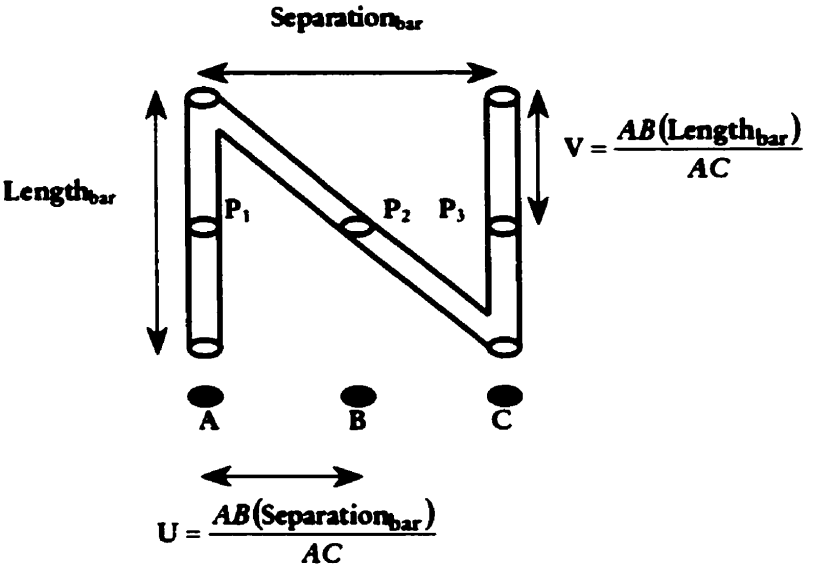

Figure 14. MR/CT fiducial marker geometry. The relative position of the middle fiducial marker of the N-shaped bar cross-section between the vertical bars allows the determination of the image slice orientation within the coordinate system defined by the frame. P_1, P_2 and P_3 are the points of intersection of the image plane with the rods. A, B and C are the position of the points of intersection on the image. $Length_{bar}$ and $Separation_{bar}$ are the bar length and bar separation in frame space. V denotes the distance along the Z axis between the middle fiducial marker and the rod extremity. U denotes the distance along X or Y (depending on the localiser box face) between the middle fiducial marker and the rod extremity.

extent of an image slice is the interval between the maximum value of the two X_{min} values, which are the interval start values along X, and the minimum value of the two X_{max} values, which are the interval end values along X, and similarly for the Y direction (Figure 16b). The Z extent is obtained by the minimum and maximum Z values of the dataset, as calculated from all the slices (Figure 16a).

The frame space extent for which the volume is to be reformatted is termed *reformatting extent*. This extent is determined by taking the union of the volume extents of the datasets to be reformatted, as illustrated in Figure 17a and b. For each volume, the region of the reformatting extent which intersects the volume extent is to be interpolated (Figure 17c and d) and the region of the reformatting extent which does not intersect the volume extent is to be padded with zeros (Figure 17c and d).

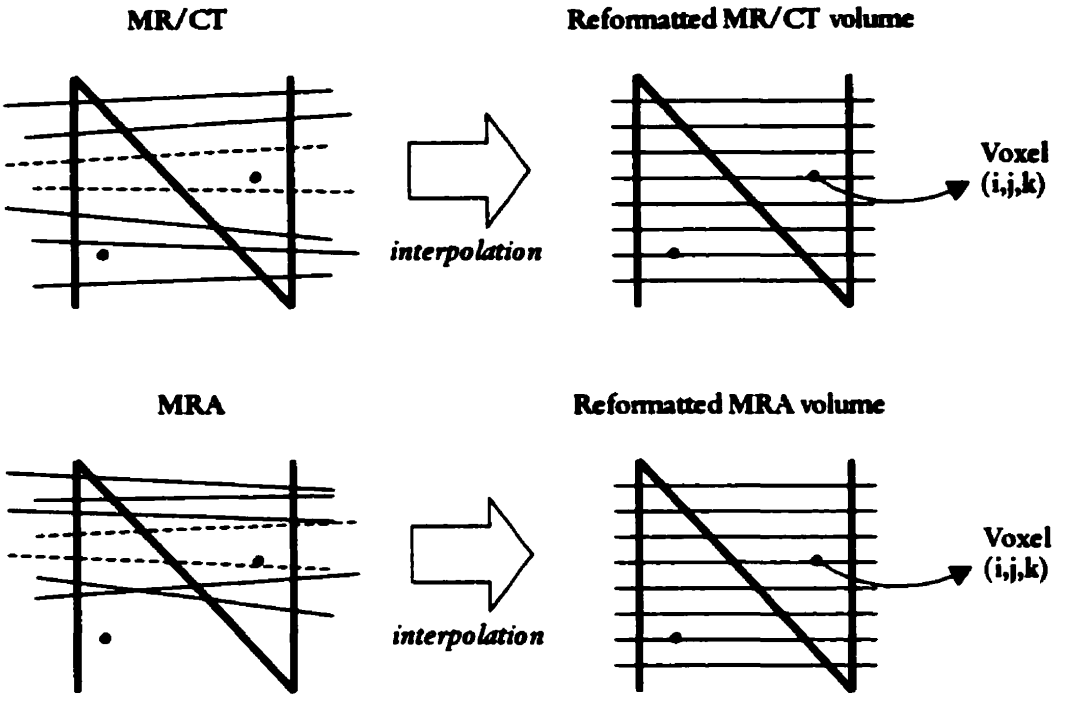

Figure 15. Slice orientation in frame space before and after reformatting (interpolation). The image slices may be arbitrarily oriented in frame space due to subtle patient movement or scanning imperfections. After reformatting, a regular voxel array is obtained. For voxel (i,j,k), the nearest two slices which bracket the voxel are illustrated in dotted format. Points, which are not between two slices, are padded with zeros.

Given the reformatting extent and the voxel sizes (v_x,v_y,v_z) in millimetres as supplied by the user, a regular voxel array is built by interpolation. The intensity of each voxel (i,j,k) within the reformatting extent is interpolated employing the slices of each dataset and their corresponding FTM. For each voxel (i,j,k) within the reformatting extent, which correspond to (x_i,y_j,z_k) in frame space coordinates, the nearest two slices that bracket the voxel, shown in dotted format in Figure 15, are determined. This is accomplished in two steps.

1. Employing the FTMs, the image coordinates (u_s,v_s) which intersect the line parallel to the Z axis passing through (x_i,y_j) in frame space are determined for each slice s.

2. Using the FTMs, the z_s value corresponding to the image coordinates (u_s,v_s) obtained in (1), is determined for each slice.

3. By comparing the z_s values of the (u_i,v_j) coordinates, the slices that bracket the voxel (x_i,y_j,z_k) to be interpolated are determined (Figure 18).

This interpolation method has been chosen among others and has been proven to be robust in cases whereby the image slices are approximately parallel to the XY plane in frame space and that the image slice thickness, as acquired at our centre, does not exceed 2 mm. With the

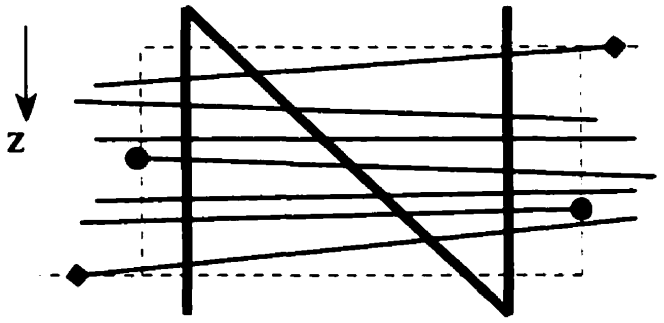

(a)

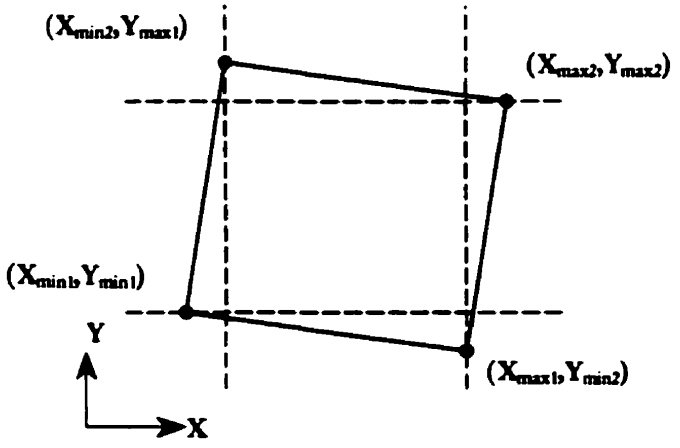

(b)

Figure 16. Volume extent determination. The extent along the X and Y axes are determined by taking the intersection of the (X,Y) extents of all image slices within the dataset, illustrated in (a). The (X,Y) extent of an image slice, as shown by the shaded area in (b), is the interval between the maximum value of the two X_{min} values and the minimum value of the two X_{max} values, and similarly for the Y direction. The extent along the Z axis is obtained by the minimum and maximum z values of the dataset, as calculated from all the slices (a). The resulting volume extent is illustrated as the dashed rectangle in (a).

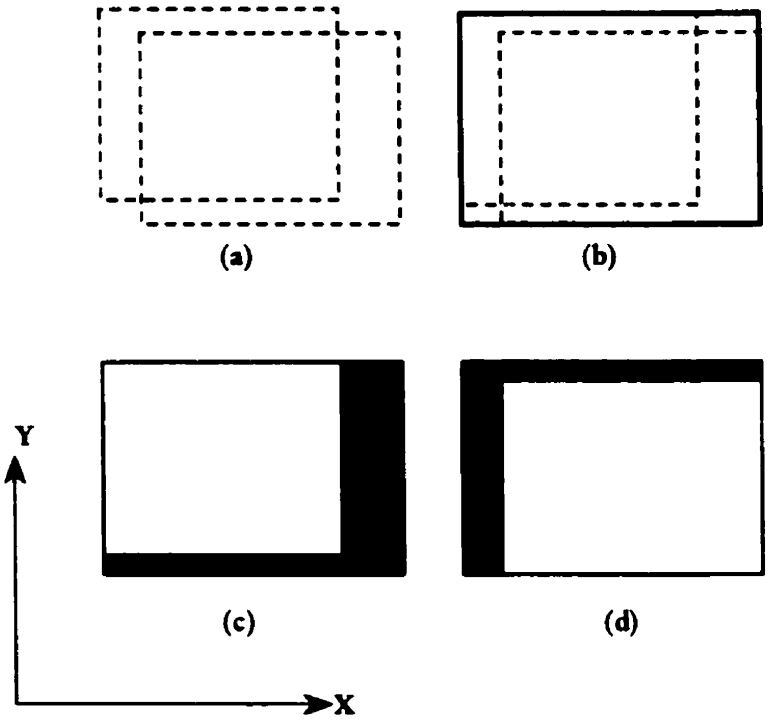

Figure 17. Reformatting extent determination. Illustrated in (a) are the volume extents of 2 datasets. The volume extents (dashed lines) as well as the reformatting extent (solid line), obtained by taking the union of the two, are shown in (b). For each volume, interpolation is performed inside the volume extent (white) as shown in c) and d). The region of the reformatting extent which does not intersect the volume extent (black) is padded with zeros (c and d).

image coordinates of the two slices determined in (3), the voxel intensity is interpolated by following two steps.

1. Since the image coordinates do not directly correspond to a pixel position, or a node as shown in Figure 18, the intensity at the image coordinates is obtained by performing a 2D bilinear interpolation [55] between the four surrounding pixels (Figure 18).

2. The voxel intensity is then determined by performing a linear interpolation [55] along Z between the two image coordinate intensities, using the distances between the slices and the voxel (Figure 18).

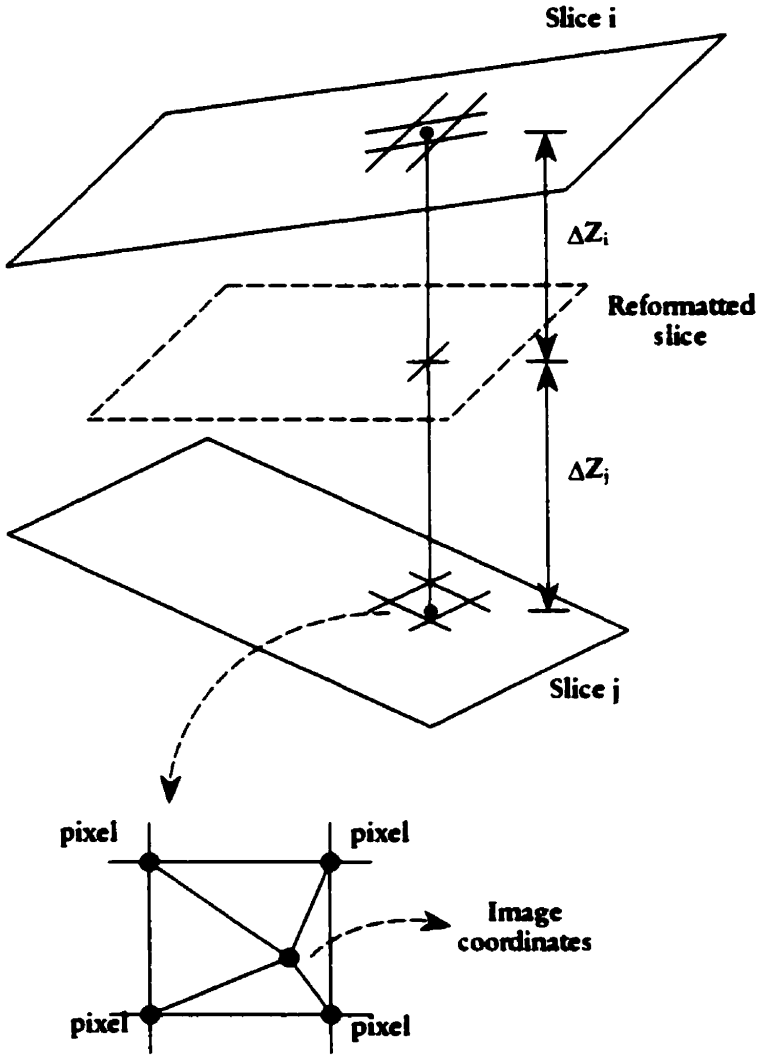

Figure 18. Interpolation procedure. The voxel intensity is obtained by interpolating between the slices that bracket the voxel. A bilinear interpolation is performed in order to get the image coordinate intensity for each slice. The voxel intensity is then determined by performing a linear interpolation along Z between the two image coordinate intensities, using the distances between the slices and the voxel.

Points which are not between two slices are padded with zeros. Since the reformatting extents are the same for both reformatted volumes, voxel (i,j,k) of the reformatted MRA volume data corresponds to voxel (i,j,k) of the reformatted MR/CT volume data. The fusion between the volumes is therefore complete.

The frame space coordinates (x_i,y_j,z_k) corresponding to voxel (i,j,k) of the reformatted volume are determined by the use of the volume transformation matrix (VTM).

$$\begin{bmatrix} x \\ y \\ z \\ 1 \end{bmatrix} = \mathbf{VTM} \begin{bmatrix} i \\ j \\ k \\ 1 \end{bmatrix} \tag{3}$$

The VTM, a 4x4 matrix, accounts for translation, rotation and scaling between frame space and image space. Since the reformatted volume is aligned with the frame, the VTM is given by

$$\mathbf{VTM} = \begin{bmatrix} v_x & 0 & 0 & x_{min} \\ 0 & v_y & 0 & y_{min} \\ 0 & 0 & v_z & z_{min} \\ 0 & 0 & 0 & 1 \end{bmatrix} \tag{4}$$

In the above expression, $(x_{min},y_{min},z_{min})$ represents the minimum of the (X,Y,Z) reformatting extent in frame space. The reformatting voxel sizes (v_x,v_y,v_z) determine the scaling between the two spaces.

Since fusion is performed employing fiducial markers and that no anatomy information is taken into account, the localisers must by firmly attached to the frame in order to assure consistency.

2.3 DSA target localisation

This module allows target localisation with a pair of DSA images, as described in section 1.3.1. As a first step, the projection geometry is determined for each DSA projection image. These projection geometries are needed for target localisation as well as for the DSA/MRA correlation module.

2.3.1 Projection geometry determination

The DSA localiser contains a series of lead beads on each side of the frame attachment (Figure 19a). The frame space coordinates of the beads are given in Figure 19b. The lead beads, when

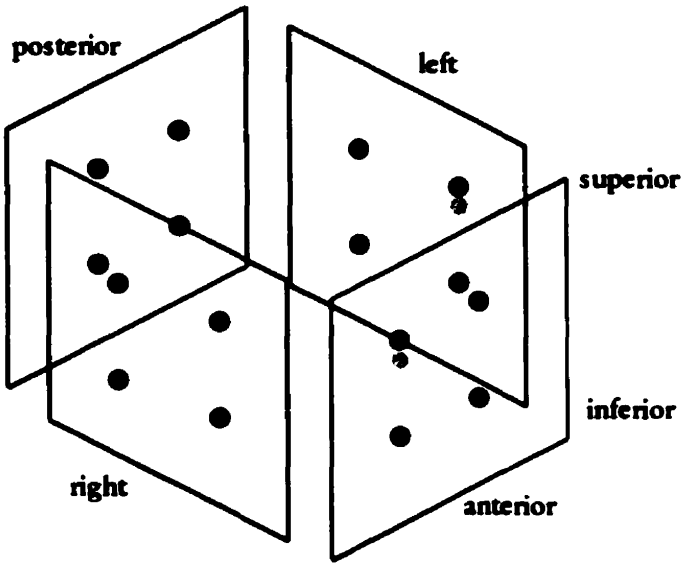

(a)

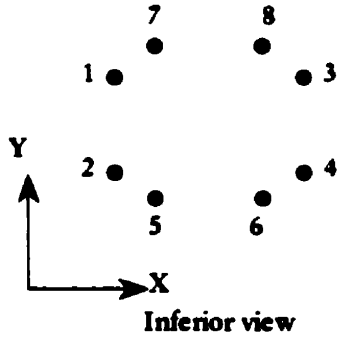

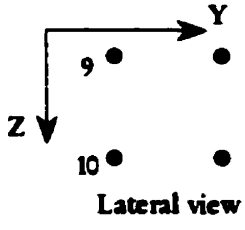

Point	x (mm)	y (mm)	z (mm)
1	4	135	---
2	4	65	---
3	196	135	---
4	196	65	---
5	67.5	-16	---
6	132.5	-16	---
7	67.5	216	---
8	132.5	216	---
9	---	---	65
10	---	---	135

(b)

Figure 19. Leksell DSA localiser. The lead beads on the localiser box are illustrated in (a). A fifth bead, illustrated in shaded form, is found on the anterior plate as well as on the left plate for box face identification on the projection images. The frame space coordinates of the beads are given in (b).

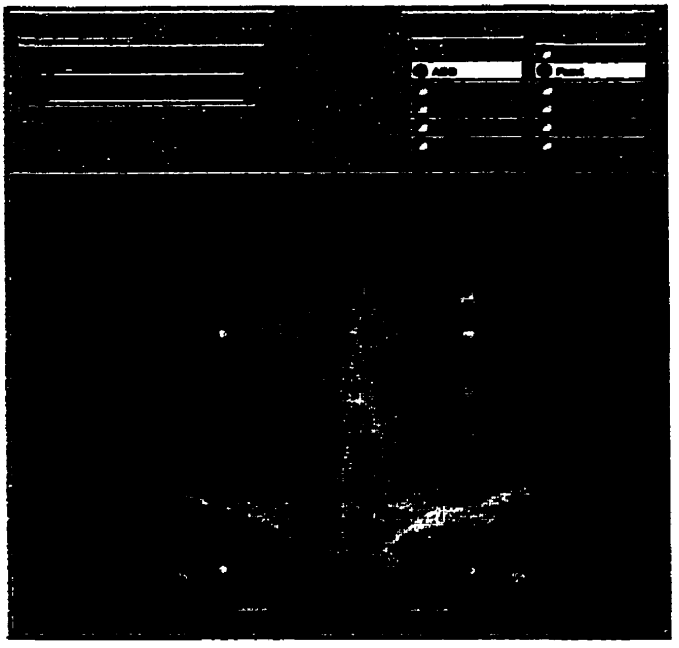

Figure 20. Panel for fiducial marker selection. The eight fiducial markers can be observed on the projection image.

projected onto the image plane, give eight image points (Figure 20). The eight markers are selected by the user and are defined in image space coordinates as (u_i,v_i). These image coordinates are employed to determine a transformation matrix which defines the perspective projection geometry by relating 3D frame coordinates to their projected positions in the image plane [54] (Figure 21). The 4x3 matrix transforms frame space coordinates into image coordinates accounting for perspective magnification.

$$[\alpha u \quad \alpha v \quad \alpha] = [x \quad y \quad z \quad 1] \begin{bmatrix} M_{11} & M_{12} & M_{13} \\ M_{21} & M_{22} & M_{23} \\ M_{31} & M_{32} & M_{33} \\ M_{41} & M_{42} & M_{43} \end{bmatrix} \tag{5}$$

In the above expression, the parameter α is a scaling factor between the two systems. The image coordinates (u,v) are obtained by dividing through by α, the homogeneous coordinate.

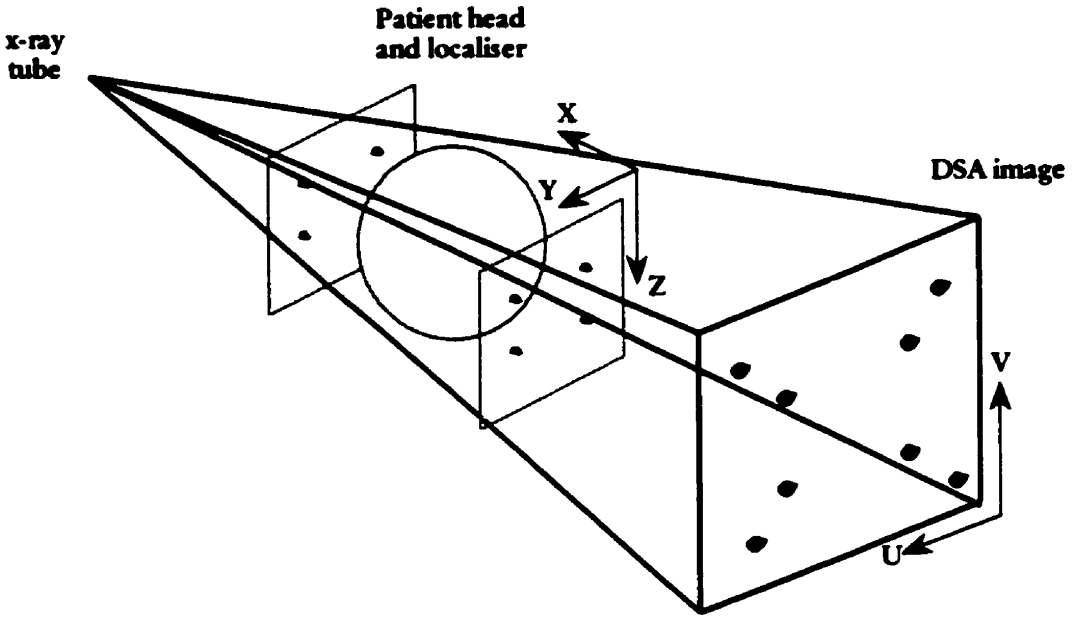

Figure 21. Perspective projection geometry. Of the eight points, the four obtained from the plate closest to the x-ray tube are more magnified than the four obtained from the plate on the opposite side.

Unlike the tomographic images, projection image coordinates cannot correspond to a single position in frame space since a single point in the image plane is the result of a many-to-one mapping of all points along the projected ray.

The matrix multiplication above results in three separate equations. The α parameter is substituted into the first two, generating a system of two equations.

$$(M_{11} - uM_{13})x + (M_{21} - uM_{23})y + (M_{31} - uM_{33})z + M_{41} = uM_{43} \quad (6)$$

$$(M_{12} - vM_{13})x + (M_{22} - vM_{23})y + (M_{32} - vM_{33})z + M_{42} = vM_{43} \quad (7)$$

For a landmark with known stereotactic frame coordinates (x,y,z) and image coordinates (u,v), two equations are available in terms of the 12 M_{ij}. Six such points providing twelve equations are sufficient to solve for the elements of the matrix, however, no more than four points may be coplanar [56]. Since eight fiducial marker points are employed in every stereotactic

projection image, the resulting over-determined system of equations is solved using a least-squares fit to ensure that the information provided by the additional markers is incorporated into the solution. The implementation of this approach employs a single value decomposition (SVD) technique [55] to obtain the desired best fit for the M_{ij} values. Dividing equations (6) and (7) by M_{43} yields a system of equations similar to equating M_{43} to 1 in equations (6) and (7) [57], however the latter reduces the system of equations to eleven variables. M_{43} is therefore set to 1 [57] and equations (6) and (7) are rewritten for the algorithm as shown below.

$$\begin{bmatrix} u_1 \\ v_1 \\ \dots \\ u_8 \\ v_8 \end{bmatrix} = \begin{bmatrix} x_1 & y_1 & z_1 & 1 & 0 & 0 & 0 & 0 & -u_1x_1 & -u_1y_1 & -u_1z_1 \\ 0 & 0 & 0 & 0 & x_1 & y_1 & z_1 & 1 & -v_1x_1 & -v_1y_1 & -v_1z_1 \\ & & & & \dots & & & & & & \\ x_8 & y_8 & z_8 & 1 & 0 & 0 & 0 & 0 & -u_8x_8 & -u_8y_8 & -u_8z_8 \\ 0 & 0 & 0 & 0 & x_8 & y_8 & z_8 & 1 & -v_8x_8 & -v_8y_8 & -v_8z_8 \end{bmatrix} \cdot \begin{bmatrix} M_{11} \\ M_{21} \\ M_{31} \\ M_{41} \\ M_{12} \\ M_{22} \\ M_{32} \\ M_{42} \\ M_{13} \\ M_{23} \\ M_{33} \end{bmatrix} \tag{8}$$

For convenience, the above equation is represented by the following relation.

$$A = BM \tag{9}$$

In order to obtain the desired best fit for the M_{ij} values, the SVD algorithm is employed to minimise the least-squares error in equation (10) with respect to the M_{ij} values.

$$error = \sum_{i=1}^{16} \left(A_i - \sum_{j=1}^{11} B_{ij} M_j \right)^2 \tag{10}$$

2.3.2 Target localisation

After the determination of the projection matrix for each projection geometry, the image coordinates of the target are determined by the user on each DSA image. The projection matrix and target image coordinates provide sufficient information to localise the target within

the frame. The target localisation process consists of determining the intersection point of the two rays between the source and target image coordinates of each DSA image.

The determination of equations (6) and (7) for each projection geometry as well as the target image coordinates on each DSA image yield a total of four equations and three unknowns (x,y,z) for target localisation [57]. This over-determined system of equations is solved employing a least-squares fit [57]. The set of equations is rewritten for the SVD algorithm as shown below.

$$\begin{bmatrix} u_1 - M_{41} \\ v_1 - M_{42} \\ u_2 - M_{41} \\ v_2 - M_{42} \end{bmatrix} = \begin{bmatrix} M_{11} - u_1 M_{13} & M_{21} - u_1 M_{23} & M_{31} - u_1 M_{33} \\ M_{12} - v_1 M_{13} & M_{22} - v_1 M_{23} & M_{32} - v_1 M_{33} \\ M_{11} - u_2 M_{13} & M_{21} - u_2 M_{23} & M_{31} - u_2 M_{33} \\ M_{12} - v_2 M_{13} & M_{22} - v_2 M_{23} & M_{32} - v_2 M_{33} \end{bmatrix} \cdot \begin{bmatrix} x \\ y \\ z \end{bmatrix} \tag{11}$$

For convenience, the above equation is represented by the following relation.

$$A = BX \tag{12}$$

In order to obtain the desired best fit for the (x,y,z) values, the SVD algorithm is employed to minimise the least-squares error in equation (13) with respect to the (x,y,z) values.

$$error = \sum_{i=1}^{4} \left(A_i - \sum_{j=1}^{3} B_{ij} X_j \right)^2 \tag{13}$$

This target localisation method does not require that the two images be orthogonal or parallel to the localiser box faces.

2.4 3D target localisation and delineation

This module allows target localisation and delineation in 3D employing the reformatted volumes. After the fusion of MRA and MR/CT datasets by the Volume fusion module, target contours which are drawn on the MRA volume can be simultaneously visualised on the reformatted MR/CT volume (Figure 22), therefore allowing both vascular and anatomical information to be taken into account in the process. Continuous feedback from the

DSA/MRA correlation module, which simultaneously projects the contours onto the DSA images, enables the user to modify contours accordingly. The drawing of contours can be performed on transverse, sagittal or coronal slices of the reformatted MRA volume. The frame location of the drawn structures is determined by the use of the VTM, described earlier.

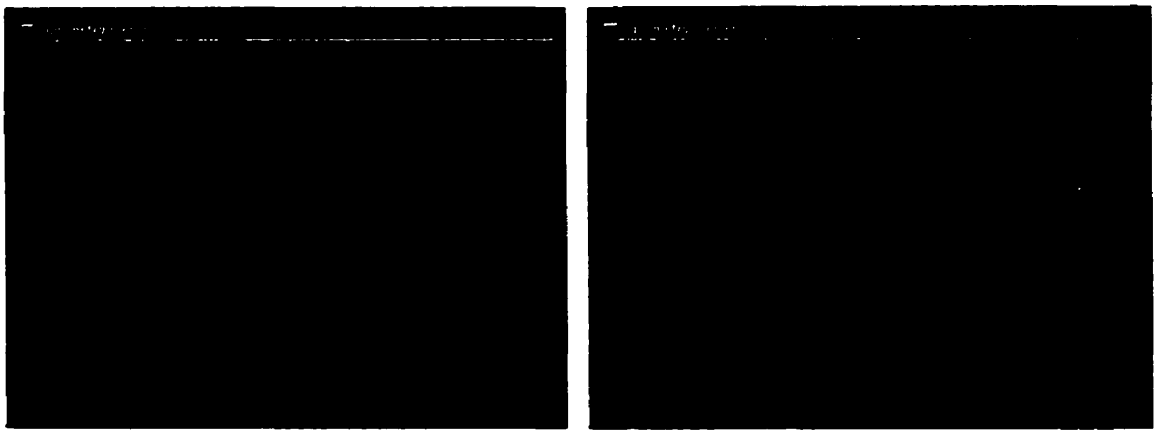

(a) (b)

Figure 22. 3D target delineation. The user delineates the target on the MRA volume (a). The contours appear simultaneously in the MR volume (b). It can be seen that the vasculature is not visible on the MR dataset (b) yet is easily outlined with the help of the fused MRA (a).

2.5 DSA/MRA correlation

To help the user in the process of target delineation , this module correlates DSA and MRA data by (1) ray-tracing through the reformatted MRA volume and (2) by projecting contours, drawn on the reformatted MRA, onto the DSA images. The correlation by ray-tracing enables the examination of possible inconsistencies which could arise from MR distortions, frame slippage, patient movement during the imaging procedure or other sources of image artefacts.

2.5.1 Ray-tracing

AP and LAT projection images of the reformatted MRA volume are obtained by ray-tracing, with the projection geometry used in the acquisition of the DSA images determined by the DSA target localisation module (Figure 23).

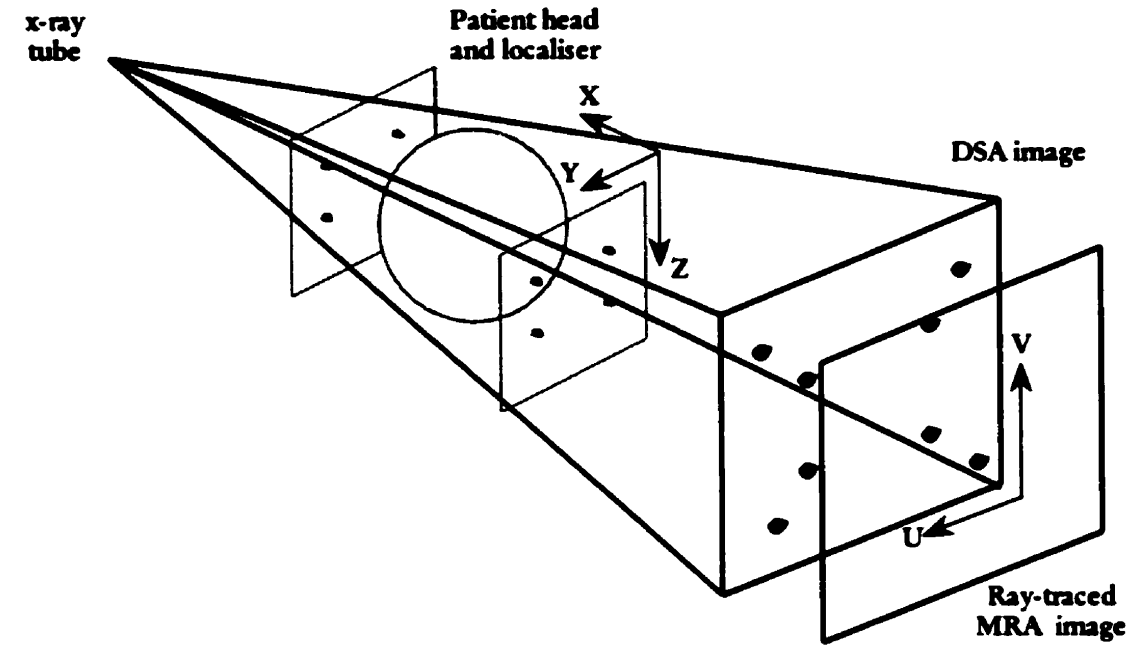

(a)

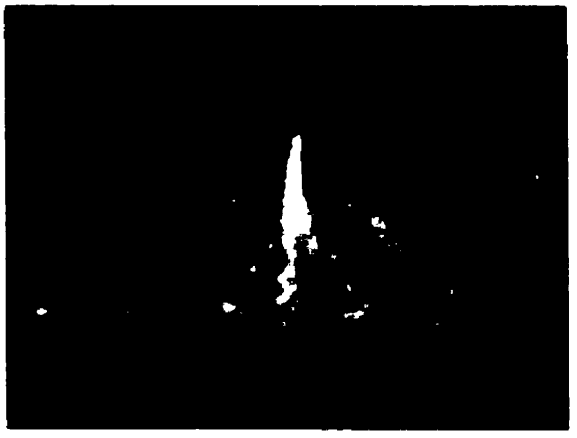

(b)

(c)

Figure 23. Ray-tracing through the MRA volume. Employing the DSA projection geometry illustrated in (a), the ray-traced MRA images (b) are correlated with the DSA images (c). The correlation enables the examination of possible inconsistencies between the DSA datasets and the reformatted MRA volume which could arise from MR distortions, frame slippage during the imaging procedure or other sources of image artefacts.

The ray-tracing algorithm employed in this module was developed by Sherouse et al. [58], similar to the method developed by Siddon [59], for simulating the acquisition of a radiographic image. Rather than considering individual voxels, the algorithm calculates the intersection points of rays with orthogonal sets of equally spaced, parallel planes [59] (Figure 24). The intersections are described as parametric values along the ray and are obtained as a subset of the intersections of the ray [59] (Figure 24). For each voxel intersection length, the corresponding voxel indices are obtained and the products of the intersected length and the particular voxel intensity are summed over all intersections to yield the radiological path [59] (Figure 24).

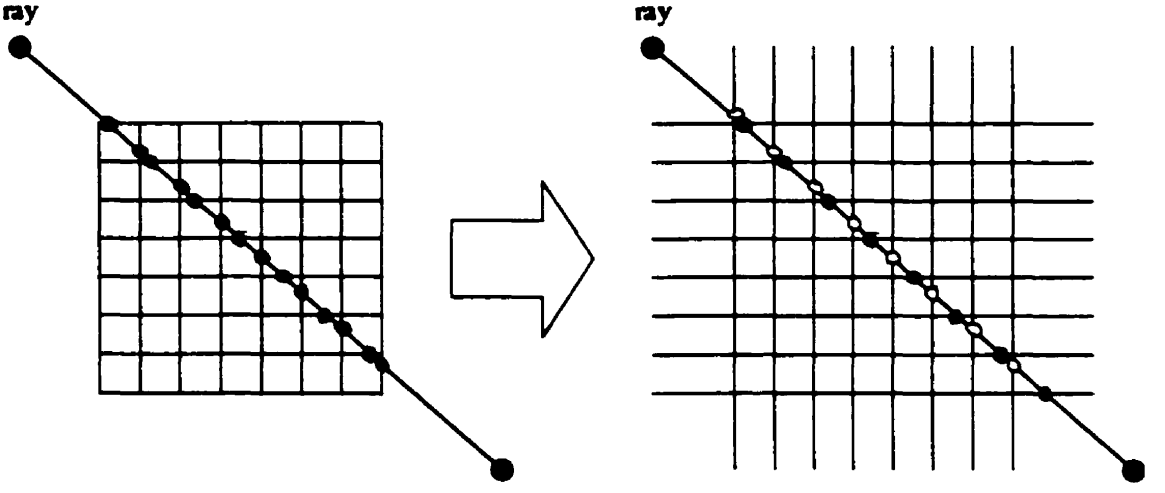

Figure 24. Ray-tracing algorithm [59]. The intersection of the ray with the voxels are a subset of the intersections of the ray with the lines [59]. The intersections of the ray with the lines are given by two equally spaced sets: one set for the horizontal lines (filled circles) and one set for the vertical lines (open circles) [59].

Since the resulting ray-traced MRA image must have the same characteristics as the DSA images, the pixel sizes, beam source position and orientation, image plane position and orientation must be determined and employed by the ray-tracing algorithm. Since these parameters are unknown, they must be derived from the correspondence between a set of image features and a set of object features [60]. The 4x3 projection transformation matrix of equation (5), relating object coordinates to projection image coordinates, describes the DSA image acquisition geometry and therefore provides sufficient information to generate a

matching view of the tomographic volume. However, a matrix decomposition is required to extract these parameters.

2.5.1.1 Matrix decomposition

The imaging geometry, described by the transformation matrix of equation (5), is illustrated in Figure 25 below.

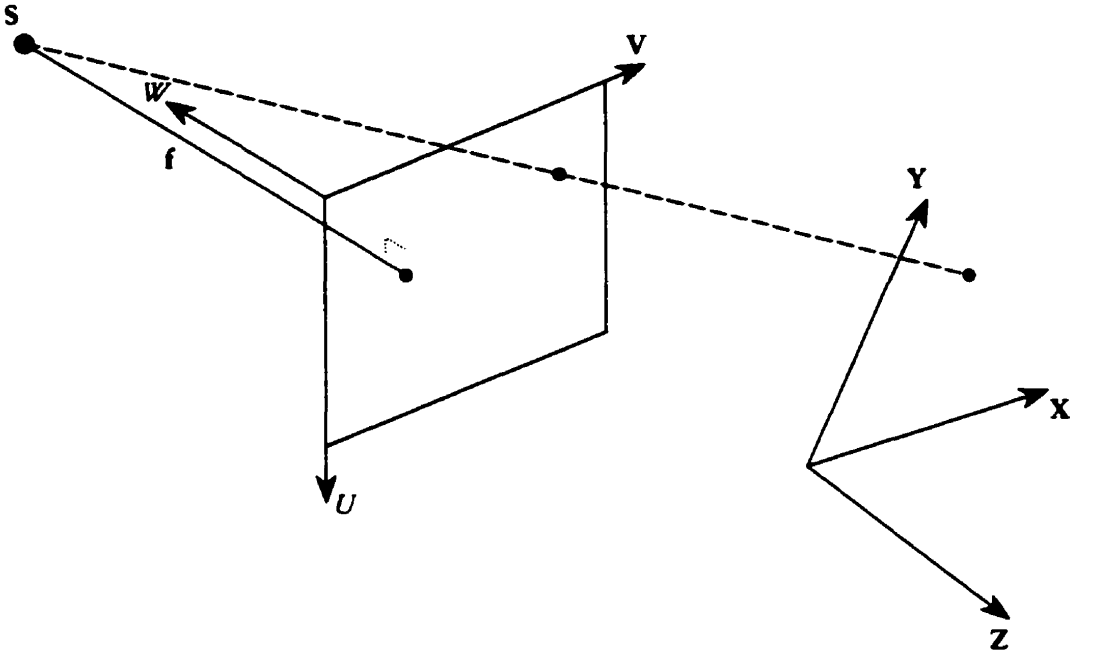

Figure 25. Projection geometry. XYZ represents the frame coordinate system. UVW represents the projection coordinate system, where (u,v) are the image coordinates of an image point and w = 0 defines the image plane. The source position is illustrated as point S. The distance between S and the image plane is denoted as f, the focal length. Each image point is the intersection of the image plane and the line connecting S and the corresponding frame point.

The projection process described in Figure 25 consists of applying consecutive individual transformations to UVW coordinate system which initially coincides with the XYZ coordinate system, in order to obtain the proper positioning of the image plane [60]. The first transformation T translates the UVW coordinate system away from the XYZ coordinate

system and is given by equation (14). T therefore consists of moving the UVW coordinate system by (x_0,y_0,z_0).

$$T = \begin{bmatrix} 1 & 0 & 0 & 0 \\ 0 & 1 & 0 & 0 \\ 0 & 0 & 1 & 0 \\ -x_0 & -y_0 & -z_0 & 1 \end{bmatrix} \tag{14}$$

The second transformation R, which is further decomposed to $R_xR_yR_z$, corresponds to consecutive clockwise rotations of θ about the X axis, ϕ about the new Y axis and ψ about the new Z axis.

$$R_x = \begin{bmatrix} 1 & 0 & 0 & 0 \\ 0 & \cos\theta & -\sin\theta & 0 \\ 0 & \sin\theta & \cos\theta & 0 \\ 0 & 0 & 0 & 1 \end{bmatrix} \tag{15}$$

$$R_y = \begin{bmatrix} \cos\phi & 0 & \sin\phi & 0 \\ 0 & 1 & 0 & 0 \\ -\sin\phi & 0 & \cos\phi & 0 \\ 0 & 0 & 0 & 1 \end{bmatrix} \tag{16}$$

$$R_z = \begin{bmatrix} \cos\psi & -\sin\psi & 0 & 0 \\ \sin\psi & \cos\psi & 0 & 0 \\ 0 & 0 & 1 & 0 \\ 0 & 0 & 0 & 1 \end{bmatrix} \tag{17}$$

The projection matrix P then applies the perspective magnification with focal length f.

$$P = \begin{bmatrix} 1 & 0 & 0 & 0 \\ 0 & 1 & 0 & 0 \\ 0 & 0 & 1 & -\frac{1}{f} \\ 0 & 0 & 0 & 1 \end{bmatrix} \tag{18}$$

The following transformation S scales the image coordinates by K_u in the U direction and K_v in the V direction which reflects an enlargement of the image if K is greater than one or shrinking of the image if K is less than one.

$$S = \begin{bmatrix} K_u & 0 & 0 & 0 \\ 0 & K_v & 0 & 0 \\ 0 & 0 & 1 & 0 \\ 0 & 0 & 0 & 1 \end{bmatrix} \tag{19}$$

The last transformation C crops the image plane which consists of translating the UVW coordinate system within the image plane by (u_0,v_0), the coordinates of the piercing point.

$$C = \begin{bmatrix} 1 & 0 & 0 & 0 \\ 0 & 1 & 0 & 0 \\ 0 & 0 & 1 & 0 \\ -u_0 & -v_0 & 0 & 1 \end{bmatrix} \tag{20}$$

The projection matrix of equation (5) is decomposed into the components given by equation (21) by the method presented by Strat [60]. The individual components of equation (21) are described in equations (14) to (20).

$$M = TRPSC = TR_xR_yR_zPSC \tag{21}$$

The consecutive transformations described by equation (21) define the perspective projection geometry of Figure 25 by transforming 3D frame coordinates (x,y,z) into projection coordinates (u,v,w) as shown in equation (22) below.

$$[\alpha u \quad \alpha v \quad \alpha w \quad \alpha] = [x \quad y \quad z \quad 1] \begin{bmatrix} M_{11} & M_{12} & M_{13} & M_{14} \\ M_{21} & M_{22} & M_{23} & M_{24} \\ M_{31} & M_{32} & M_{33} & M_{34} \\ M_{41} & M_{42} & M_{43} & M_{44} \end{bmatrix} \tag{22}$$

Since the transformation matrix of equation (5) is a 4x3 matrix, it is adjusted to a 4x4 matrix M by the following substitution [60].

$$[\alpha u \quad \alpha v \quad \alpha w \quad \alpha] = [x \quad y \quad z \quad 1] \begin{bmatrix} M_{11} & M_{12} & 0 & M_{14} \\ M_{21} & M_{22} & 0 & M_{24} \\ M_{31} & M_{32} & 1 & M_{34} \\ M_{41} & M_{42} & 0 & M_{44} \end{bmatrix} \tag{23}$$

For convenience, the above equation is represented by the following relation.

$$U = XM \tag{24}$$

In equation (23), the third column of M introduces the third coordinate w resulting in a 3D referential system. Column 1,2 and 4 of M correspond to column 1,2 and 3 of the transformation matrix of equation (5) respectively. The image coordinates are obtained by dividing through by the parameter α. For notational simplicity, we shall assume that all matrix multiplications automatically normalise the image coordinates and therefore the α parameter is omitted from the equation.

The image formation process, as accomplished with the adapted 4x4 transformation matrix, can be written as

$$[u \quad v \quad 0 \quad 1] = orthoproject(XM) \tag{25}$$

In the above expression, the parameter α is omitted for notational simplicity, X is the coordinate of a world point and the orthoproject operator performs an orthographic projection along the W axis such that

$$orthoproject([u \quad v \quad w \quad 1]) = [u \quad v \quad 0 \quad 1] \tag{26}$$

The geometric matrix decomposition consists of determining:

1. the source position $S(s_x,s_y,s_z)$;

2. the image plane orientation (θ,ϕ);

3. the piercing point (u_0,v_0) for cropping;

4. the focal length (f) and scale (K_u,K_v);

5. the rotation within the image plane (ψ).

The technique to determine the source position is illustrated in Figure 26. First, the matrix inverse M^{-1} is computed. An arbitrary frame point $X_1(x_1,y_1,z_1)$ is chosen and its projection coordinates (u_1,v_1,w_1) are determined. If the image coordinates were multiplied by the inverse matrix M^{-1}, the initial frame coordinates would be obtained. Instead, the image coordinates are projected onto the image plane employing the orthoproject operator to obtain $(u_1,v_1,0)$, where (u_1,v_1) are the image coordinates of (x_1,y_1,z_1). This image point is then backprojected by multiplying by M^{-1} to obtain X_{11}. The point X_{11} specifies another frame point which is different from X_1 but constrained to lie along the line connecting X_1 and the source position S. All points lying along the line connecting X_1 and S are transformed by M to points identified by (u_1,v_1,w), where w varies with each point, and vice-versa with M^{-1}. The process described above is repeated with another point X_2 to obtain the point X_{21} which must lie on the line connecting X_2 and S. The points X_1 and X_{11}, and X_2 and X_{21} define two lines that pass

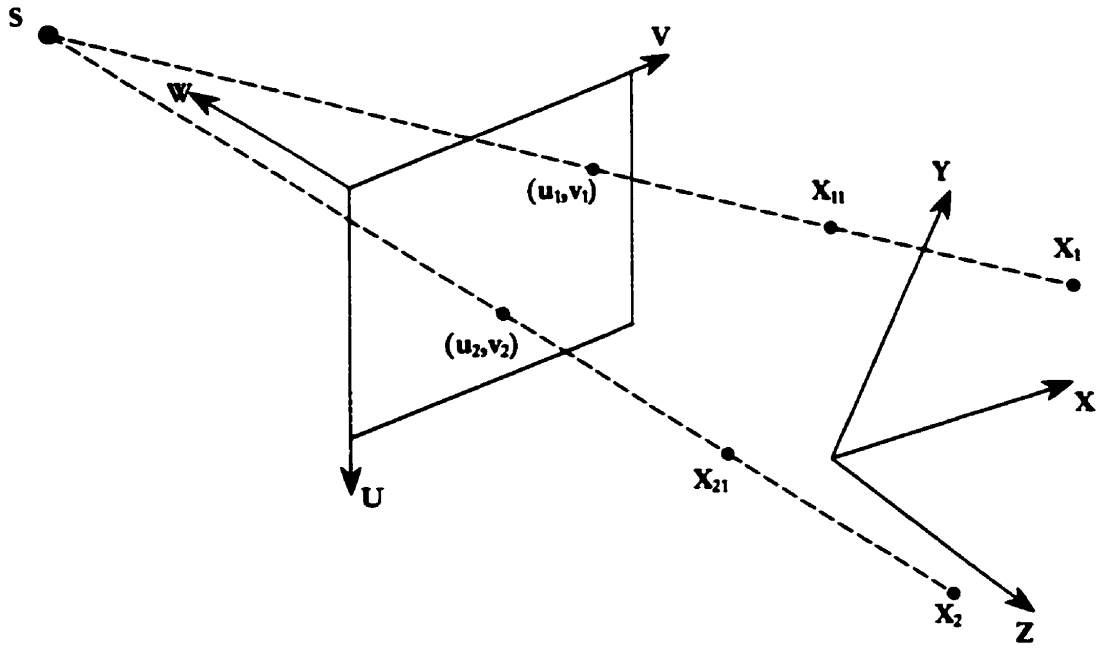

Figure 26. Geometry for the determination of the source position.

through S. The intersection point of the two lines is computed to obtain the frame coordinates of S. This method will fail if either X_1 or X_2 lie in the image plane or if X_1, X_2 and S are colinear. Since the choice of points is arbitrary, valid points that allow the unique determination of S can always be found.

The orientation of the image plane is established by the following observation. Each image point is the intersection of the image plane and the line connecting S and the corresponding frame point. A frame point lying in a plane passing through S and parallel to the image plane would therefore have infinite image coordinates since this geometry would result in a focal length equal to zero (Figure 27). The only way this can happen for a frame point in such an image plane is if the fourth component of the image coordinate is zero.

$$[u \quad v \quad w \quad 0] = [x \quad y \quad z \quad 1] \; M \tag{27}$$

Equation (27) yields the following relation.

$$M_{14}x + M_{24}y + M_{34}z + M_{44} = 0 \tag{28}$$

From equation (28), the vector $\mathbf{n} = (M_{14}, M_{24}, M_{34})$ is normal to the image plane and parallel to the source's direction of view. The orientation of $\mathbf{n}$, which is the image plane orientation, can be calculated in terms of rotation about the axes by using spherical coordinates such that

$$\theta = \arctan \frac{M_{24}}{-M_{34}} \tag{29}$$

$$\phi = \arcsin \frac{-M_{14}}{\sqrt{M_{14}^2 + M_{24}^2 + M_{34}^2}} \tag{30}$$

The angle ϕ therefore limits the matrix decomposition to Y axis rotations within the interval $\left[-\pi/2, \pi/2\right]$. The final rotation parameter, ψ, is the rotation within the image plane about the new Z axis. This angle cannot be determined from the normal to the image plane. Instead, it requires a more complex derivation that involves the determination of the piercing point and relative scale factors.

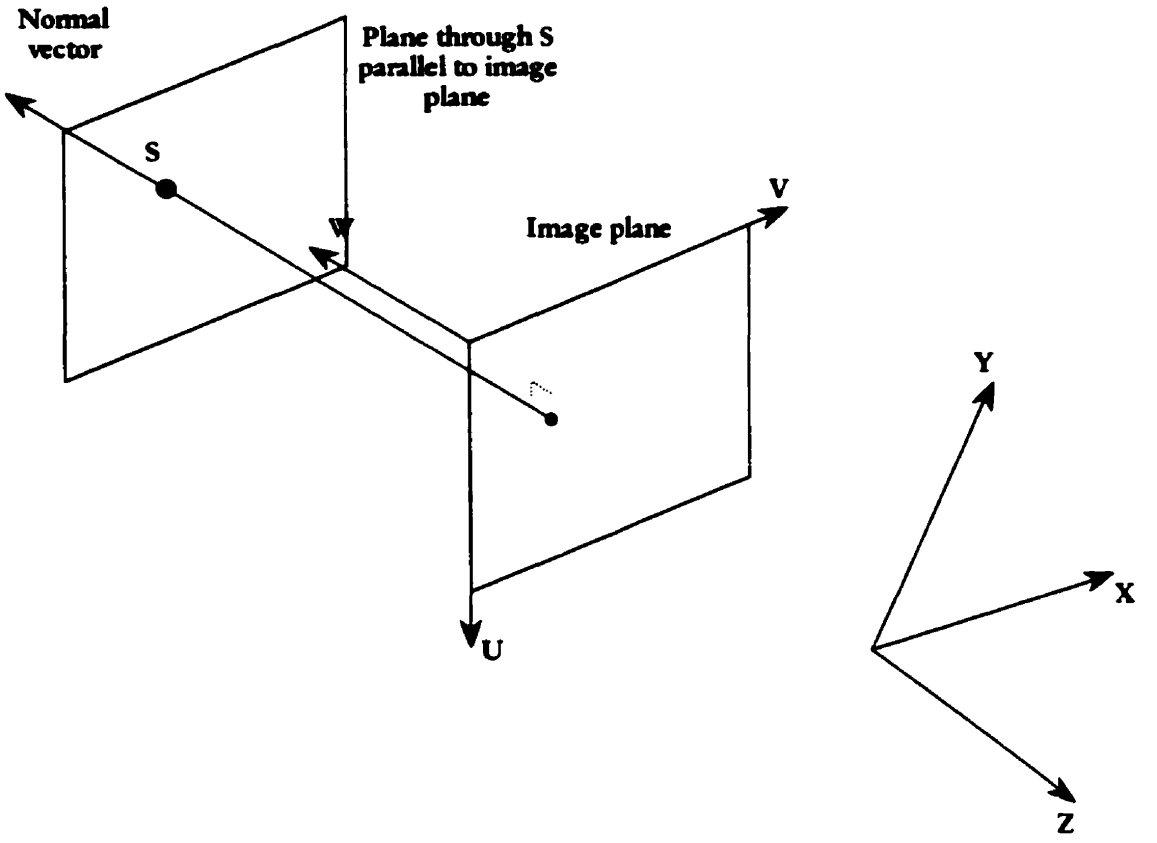

Figure 27. Determination of image plane orientation.

The piercing point (u_0,v_0) is the point in the image plane pierced by the principal ray (Figure 28). The principal ray, which is perpendicular to the image plane, passes through the source and points in the same direction as the normal vector of the image plane. To find the piercing point, a point P along the principal ray is determined.

$$\overrightarrow{OP} = \overrightarrow{OS} + k\overrightarrow{N} \tag{31}$$

In the expression above, $\overrightarrow{OP}$ is the vector between the frame space coordinate system origin and the point P, $\overrightarrow{OS}$ is the vector between the origin and the source S, k is a scalar other than zero and $\overrightarrow{N}$ is a vector that possesses the same components as the normal vector of the image plane. The source cannot be used as a point along the principal ray since this point has an

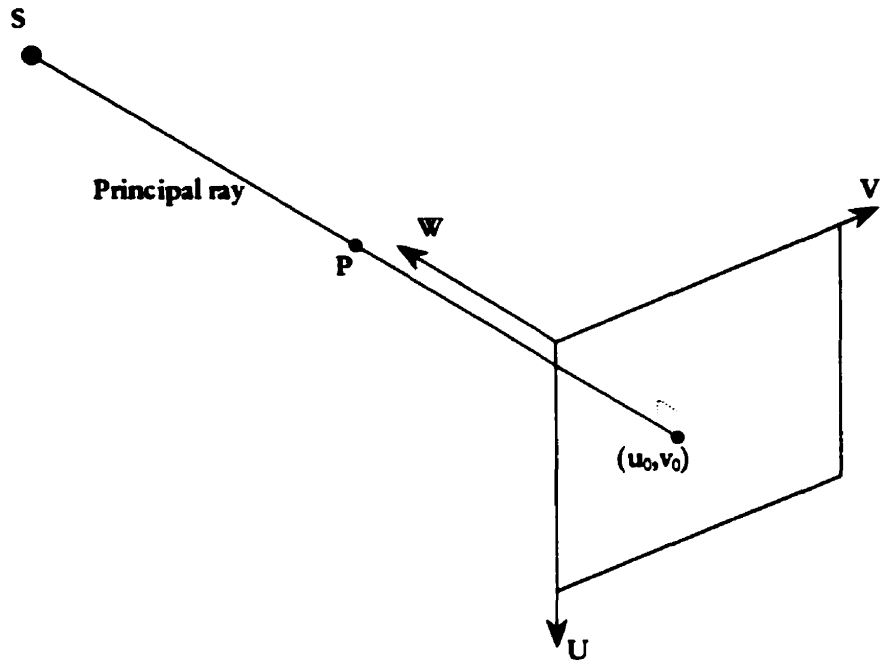

Figure 28. Determination of the piercing point.

infinite amount of image coordinates and therefore, k must be a scalar other than zero. The piercing point U_0 is obtained by equation (32) below with the use of the orthoproject operator of equation (26) since any point along the principal ray must project onto the piercing point in the image. The extent at which the image was cropped is given by (u_0,v_0).

$$U_0 = orthoproject(PM) = [u_0 \quad v_0 \quad 0 \quad 1] \tag{32}$$

Since there is no difference between scaling the image at a constant focal length and varying the focal length with constant scaling, doubling the focal length is equivalent to enlarging the picture by a factor of two. Figure 29 shows the geometry for computing the U component of the scale factor. First, an arbitrary frame point X_1, not along the principal ray, is chosen and its orthoprojected image point $(u_1,v_1,0)$ is computed. Conversion of these image units to frame units requires dividing by scale factors K_u and K_v along the U and V axes respectively such that

$$u_1' = \frac{u_1}{K_u} \qquad v_1' = \frac{v_1}{K_v} \tag{33}$$

In the above expression, u'_1 and v'_1 are the distances of an image point from the image origin, measured in frame units. Next, the angle α_u between the principal ray and the ray from S to X_1 projected in the plane $v = v_0$ is computed. First, the orthoprojected image point $(u_1,v_1,0)$ of X_1 is projected onto v_0 in order to get $(u_1,v_0,0)$. The image point $(u_1,v_0,0)$ is then multiplied by the inverse matrix M^{-1} in order to get a backprojected point X_{11} in frame space. The angle α_u is obtained by computing the angle between the principal ray and the ray between S and X_{11}. From Figure 29, the following relation must hold.

$$\tan\alpha_u = \frac{u_1' - u_0'}{f} = \frac{\frac{u_1}{K_u} - \frac{u_0}{K_u}}{f} \tag{34}$$

If the focal length is known, the scale factor is

$$K_u = \frac{u_1 - u_0}{f \tan\alpha_u} \tag{35}$$

If the scale factor is known, the focal length is

$$f = \frac{u_1 - u_0}{K_u \tan\alpha_u} \tag{36}$$

The computation of K_v, the V component of the scale factor, is identical. Neither K_u nor K_v can be determined individually without knowledge of the focal length, but their ratio can be calculated by

$$\frac{K_u}{K_v} = \left(\frac{u_1 - u_0}{v_1 - v_0}\right)\frac{\tan\alpha_v}{\tan\alpha_u} \tag{37}$$

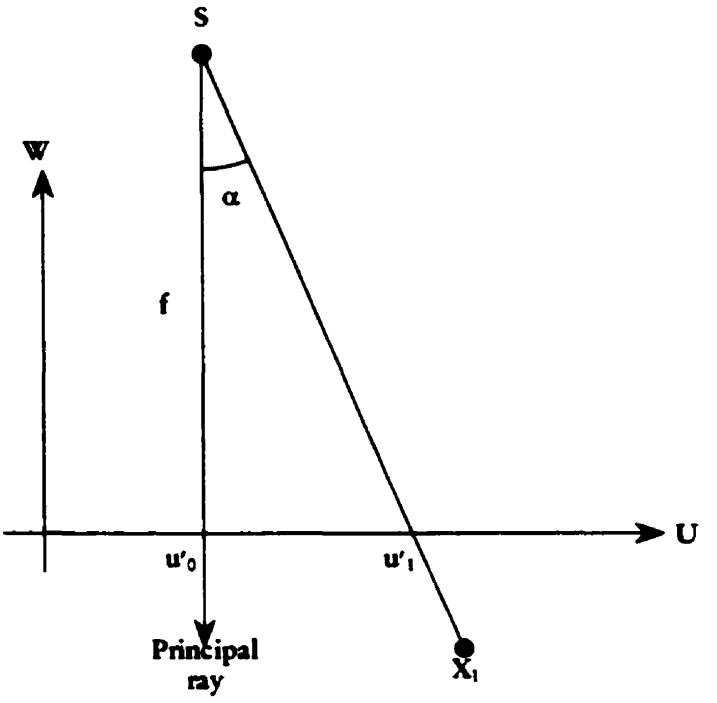

Figure 29. Geometry for determination of scale factors.

Once the piercing point and scaling factor ratios are computed, the rotation in the image plane ψ can subsequently be determined. The value of ψ is obtained by choosing a frame point and comparing its projection onto the image plane under two different situations, as illustrated in Figure 30. First, the coordinates of the source S and an arbitrary focal length f are employed to reconstruct the translation matrix T. T corresponds to a translation of the UVW coordinate system to the source position S followed by a translation of length f in the direction of the normal vector of the image plane. The angles θ and ϕ are employed to reconstruct the rotation matrices R_x and R_y and the chosen focal length is used to construct a perspective projection matrix P'. A projection transformation model M_1 can be employed to compute the projection P_1 of an arbitrary frame point.

$$M_1 = TR_xR_yP' \tag{38}$$

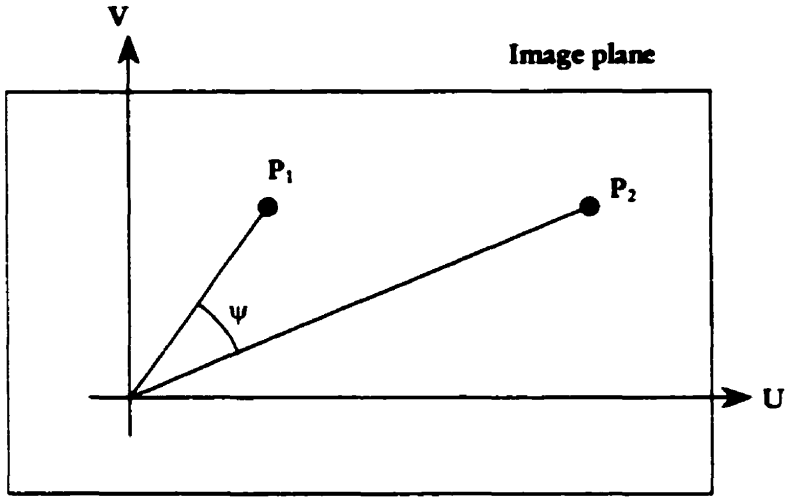

Figure 30. Determination of rotation within the image plane.

Next, the previously determined piercing point is employed to reconstruct the matrix C. Then, the effects of cropping are eliminated from the original projection transformation matrix M of equation (21) by multiplying M by C^{-1} to obtain

$$M' = MC^{-1} = TRPSCC^{-1} = TRPS \tag{39}$$

Next, the effects of unequal scaling in the U and V directions are eliminated by constructing a scale transformation matrix S'

$$S' = \begin{bmatrix} 1 & 0 & 0 & 0 \\ 0 & \frac{K_u}{K_v} & 0 & 0 \\ 0 & 0 & 1 & 0 \\ 0 & 0 & 0 & 1 \end{bmatrix} \tag{40}$$

and multiplying M' by S' to obtain a second projection transformation matrix M_2.

$$M_2 = M'S' = TRPSS' = TRPS'' \tag{41}$$

In the equation (41), S'' is given by

$$S'' = \begin{bmatrix} K_u & 0 & 0 & 0 \\ 0 & K_u & 0 & 0 \\ 0 & 0 & 1 & 0 \\ 0 & 0 & 0 & 1 \end{bmatrix} \tag{42}$$

Finally, M_2 is employed to compute a projection P_2 of the previously chosen frame point.

The angle ψ can now be determined from the following observation. The only differences between M_1 and M_2 are their focal lengths, a scale factor and a rotation about the W axis. Although the scale factor is unknown, it is equal in the U and V directions because this was compensated for in computing M_2. Together the scale factor and focal length differences serve only to change the size of the image and impose no other distortions. Observe that P_1 is the image point that would be obtained if there were no rotation about the W axis, no scaling and no cropping of the image. Similarly, P_2 is the image point that is obtained by starting with the true image point associated with the chosen object point and undoing the effects of cropping and unbalanced scaling. Any difference between P_1 and P_2 must be the result of different-sized images or of rotation about the W axis. Since this rotation is centred about the origin of this coordinate space, the angle ψ can be determined by measuring the angle between the vectors from the UVW coordinate system origin to points P_1 and P_2. The different focal lengths and scale factors can affect only the distance of the points from the origin and cannot alter the angle between the vectors when measured from the origin. Therefore, ψ can be obtained by

$$\psi = \arccos \frac{\overrightarrow{OP_1} \bullet \overrightarrow{OP_2}}{\left|\overrightarrow{OP_1}\right| \cdot \left|\overrightarrow{OP_2}\right|} \tag{43}$$

The angle ψ therefore limits the matrix decomposition to Z axis rotations within the interval $[0, \pi]$. Since the geometric parameters have been determined, they can now be assigned to the ray-tracing algorithm.

2.5.1.2 Geometric parameters for ray-tracing algorithm

For the algorithm employed in this module [58], the source position and image plane orientation must be given in the form of a frame to beam 4x4 coordinate transformation matrix (FB) [61]. The matrix FB defines a change of referential system and therefore accounts

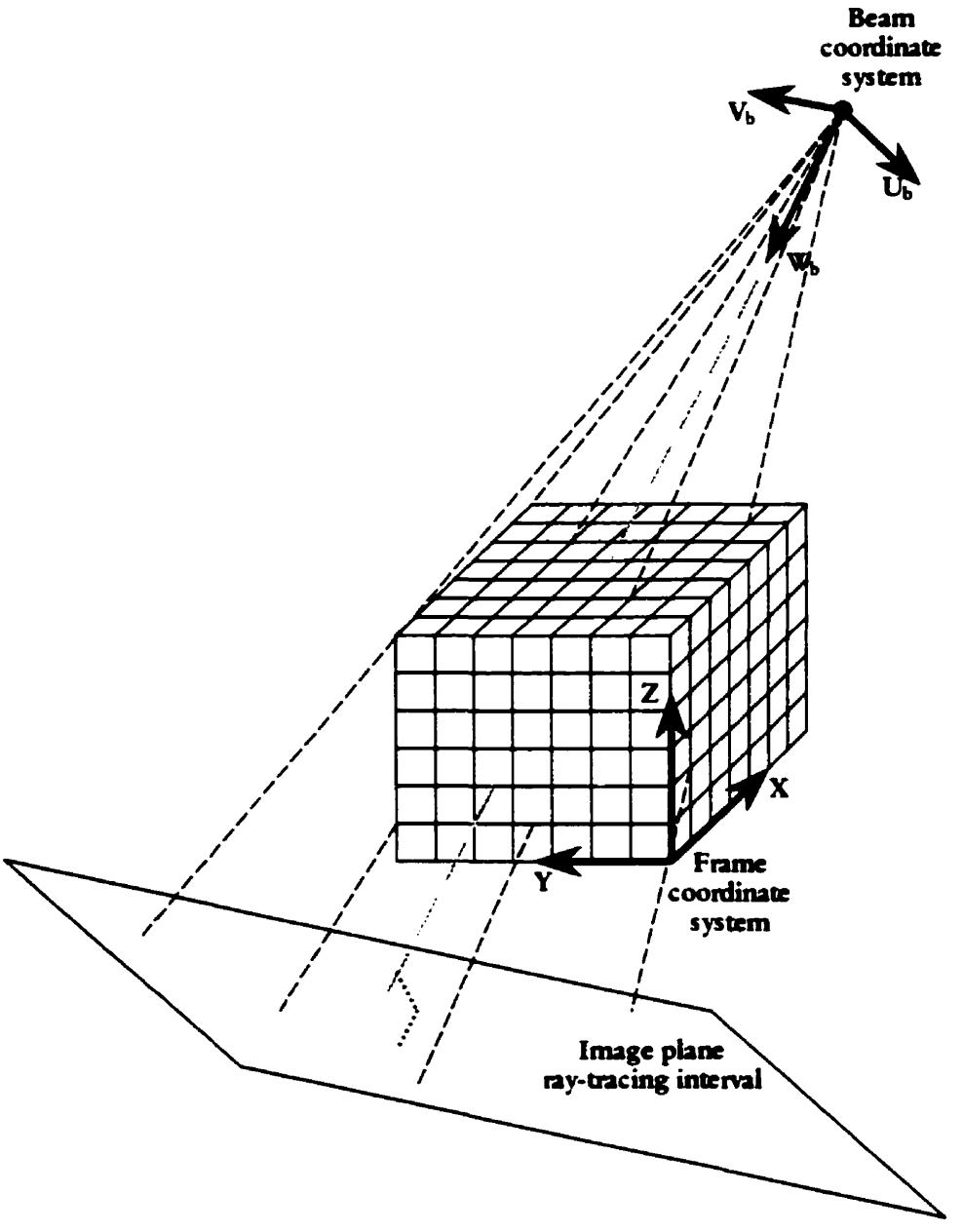

Figure 31. Coordinate system transformation. The transformation between the frame coordinate system and the beam coordinate system must be provided in order to produce the radiographic image. The transformation accounts for translation, rotation and scaling between the referential systems and defines the beam source position and orientation.

for translation, rotation and scaling between the beam coordinate system and the frame coordinate system (Figure 31) [61]. The beam coordinate system origin is positioned at the source position. The W_b axis points towards the object and has the same characteristics as the principal ray of the perspective projection [61]. The U_b and V_b axes are positioned with the same orientation as the U and V axes of the image plane.

The construction of the frame to beam coordinate transformation matrix FB is performed by employing the geometric parameters obtained in the preceeding section and applying them to Figure 31. The following transformations are applied in the following order to construct the FB matrix.

1. Translation of the beam coordinate system away from the frame coordinate system to the source position $S(s_x,s_y,s_z)$ [61];

2. Consecutive rotations of (θ,ϕ,ψ) along (X,Y,Z) respectively [61];

3. Scaling factor of -1 along Z. In the matrix decomposition, the W axis points away from the object [60] but for the ray-tracing algorithm, the corresponding W_b axis must point towards the object [61].

The remaining geometric parameters are employed to determine the pixel size, source to film distance and image plane ray-tracing interval along the U_bV_b coordinate system in order for the ray-traced image to have the same characteristics as the corresponding DSA projection image. The pixel sizes are determined using equation (35) employing an arbitrary focal length f. The image plane ray-tracing interval along the U_bV_b coordinate system at $w_b = f$ must have the same amount of pixels as the DSA image and must be positioned in such a way that the W_b axis intersects the piercing point in the image plane, as illustrated in Figure 28.

2.5.2 Contour projections

After the recovery of the projection geometry, MRA contours can be projected onto the DSA images (Figure 32). This functionality enables the correlation of the contoured 3D volume with the target extent observable on the DSA images. Therefore, this module serves as a

simultaneous feedback to the 3D target localisation and delineation module enabling the contours to be modified accordingly.

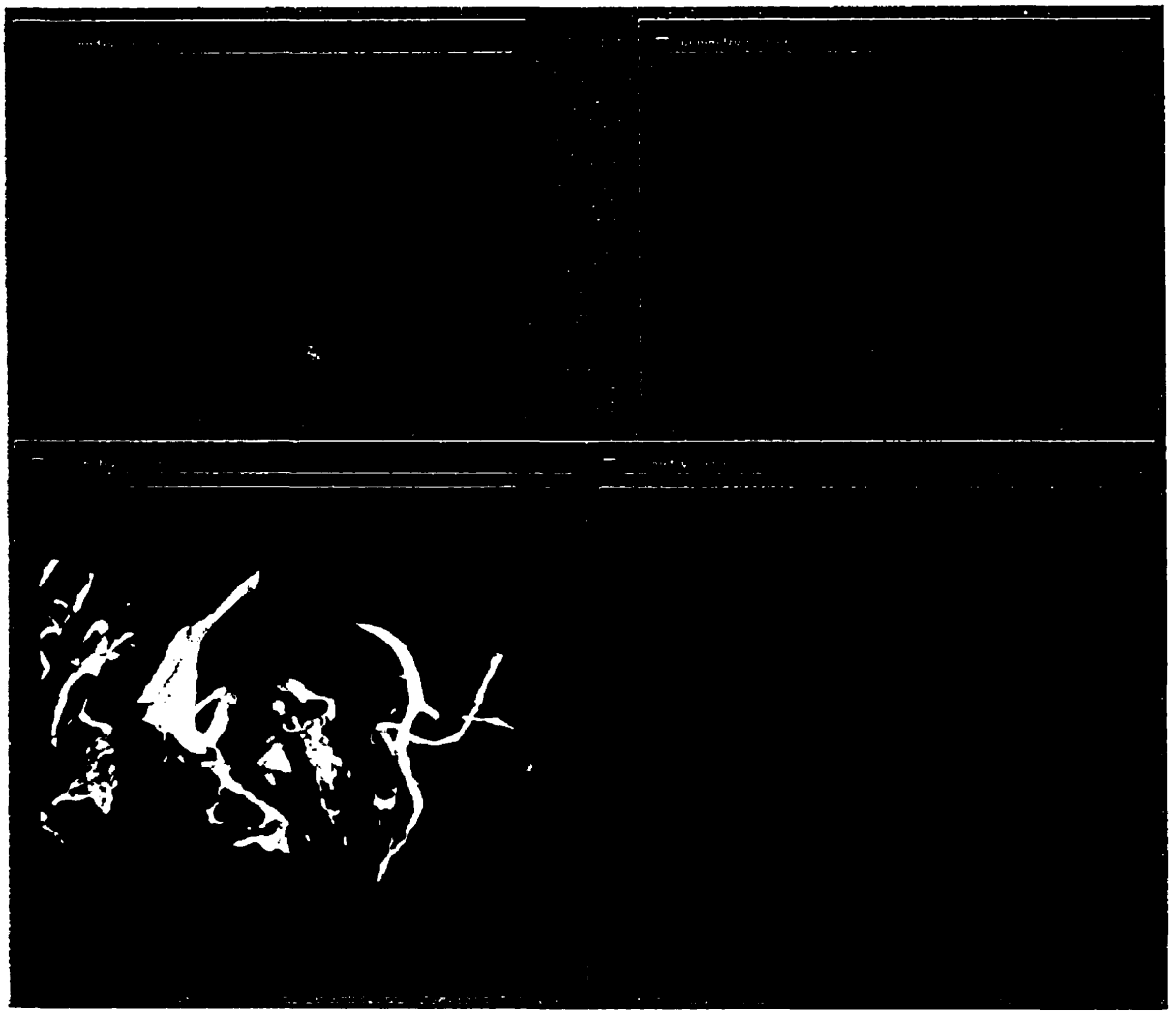

Figure 32. Panel for 3D target localisation and delineation and contour correlation. The contours, which are drawn on the MRA (bottom left window), simultaneously appear on the MR (bottom right window) with the help of the 3D target localisation and delineation module. The 3D surface representation of the vasculature is removed when the contours are to be drawn (Figure 22). As the contours are drawn on the MRA, their projections simultaneously appear on the DSA images (top left and right), with the help of the DSA/MRA correlation module, which enables the correlation of the contoured volume with the target extent observable on the DSA images. The contours drawn on the MRA can be modified accordingly.

The frame position (x,y,z) of each contour point (i,j,k) is determined using the VTM of equation (3) and is projected onto the image plane of the DSA image. The contours are projected employing the transformation matrix M of equation (5).

2.6 Summary

In this chapter, the tools of the developed visualisation system were presented. The system consists of four modules: (1) Volume fusion, (2) DSA target localisation, (3) 3D target localisation and delineation and (4) DSA/MRA correlation. The Volume fusion module fuses the MRA and MR/CT volumes. The DSA target localisation module determines the target position and projection geometry from a pair of DSA images. The next module performs 3D target localisation and delineation within the fused volumes with feedback from the DSA/MRA correlation module, which simultaneously projects the contours onto the DSA images. The DSA/MRA correlation module is also responsible for visual correlation of MRA and DSA data by ray tracing through the MRA volume.

Chapter Three

3 APPLICATIONS

3.1 Introduction

This chapter validates the developed system tools described in the previous chapter and presents examples of their application in clinical cases. The MRA/MR/CT volume localisation and the 2D DSA target localisation were validated by comparing the results obtained with the developed system to those obtained with a clinically used in-house treatment planning software [62, 63]. The ray-tracing process is validated by evaluating the error between the image fiducial marker positions and the positions of the projected fiducial markers as predicted by (1) the SVD algorithm with the projection matrix of equation (5), (2) the matrix decomposition employing equation (21) and (3) the ray-tracing algorithm [58]. A phantom example validates the entire procedure by comparing results obtained with the developed system to those obtained by the clinically commissioned BrainScan software (BrainLab, Heimstetten, Germany) as well as by performing a visual check of a phantom landmark position within the frame. Two examples of patients which had previously undergone radiosurgery and that had been planned with only DSA and MR images are presented.

3.2 Validation

The 3D MRA/MR/CT and 2D DSA target localisation processes were validated by comparing results obtained with the developed system to a clinically used in-house treatment

planning software [62, 63]. Since the fiducial markers are user selected, the target locations are expected to differ by a small amount between the two systems. The 3D localisation process comparison, as shown in Figure 33, was performed with ten prominent anatomical features and presented an average difference in distance between points of 0.7 ± 0.2 mm and of 0.7 ± 0.3 mm for the initial images and reformatted images respectively. The uncertainty in fiducial marker selection by the user is approximately 0.7 ± 0.3 mm with a pixel size of 0.93 mm. The 2D localisation process, shown in Figure 34, was validated with eleven prominent image features presenting an average difference in distance between points of 0.7 ± 0.4 mm.

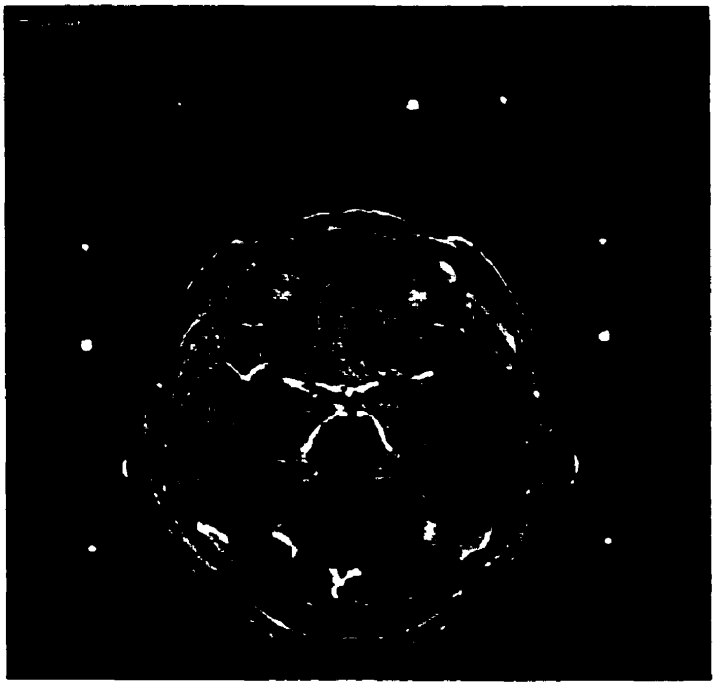

(a)

Target 1	
x	71.2 mm
y	112.3 mm
z	121.5 mm

(b)

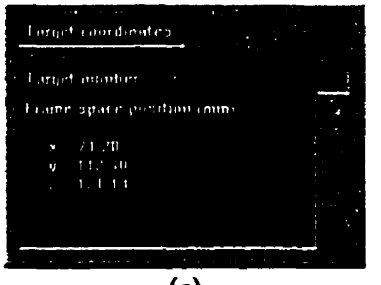

(c)

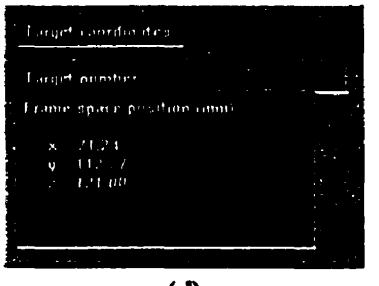

(d)

Figure 33. The 3D localisation process comparison between the developed system and the clinically used in-house treatment planning software [62, 63]. A prominent anatomical feature, shown in (a), shows good agreement between the in-house treatment planning software (b) and the developed system with both initial (c) and reformatted (d) images.

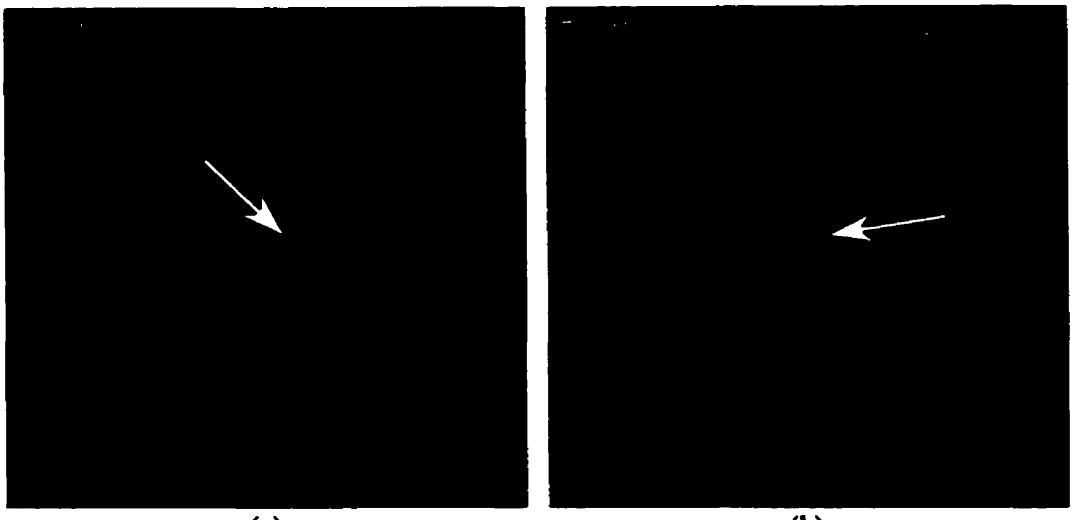

(a) (b)

Target 1	
x	91.0 mm
y	99.7 mm
z	93.9 mm

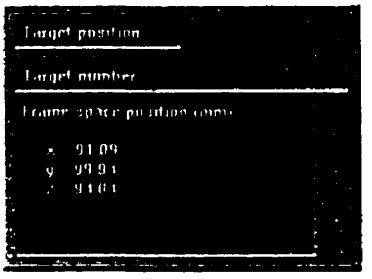

(c) (d)

Figure 34. The 2D localisation process comparison between the developed system and the clinically used in-house treatment planning software [62, 63]. A prominent image feature, shown in (a) and (b) by the solid arrows, shows good agreement between the in-house treatment planning software (c) and the developed system (d).

The ray-tracing process is validated by evaluating the error between the image fiducial marker positions and the positions of the projected fiducial markers as predicted by (1) the SVD algorithm with the projection matrix of equation (5), (2) the matrix decomposition employing equation (21) and (3) the ray-tracing algorithm [58]. Six projection geometries, yielding a total of forty-eight points, were evaluated and systematic errors of 0.5 ± 0.2 pixels, 1.6 ± 1.2 pixels and 1.8 ± 1.3 pixels were introduced by the SVD algorithm, matrix decomposition and ray-tracing algorithm respectively. The positions of the image fiducial markers and of the projected fiducial markers by ray-tracing are shown in Figure 35.

The contour projections on the DSA images are validated by the results of the SVD algorithm error in the ray-tracing validation since the error corresponds to a comparison between image positions and projected frame positions.

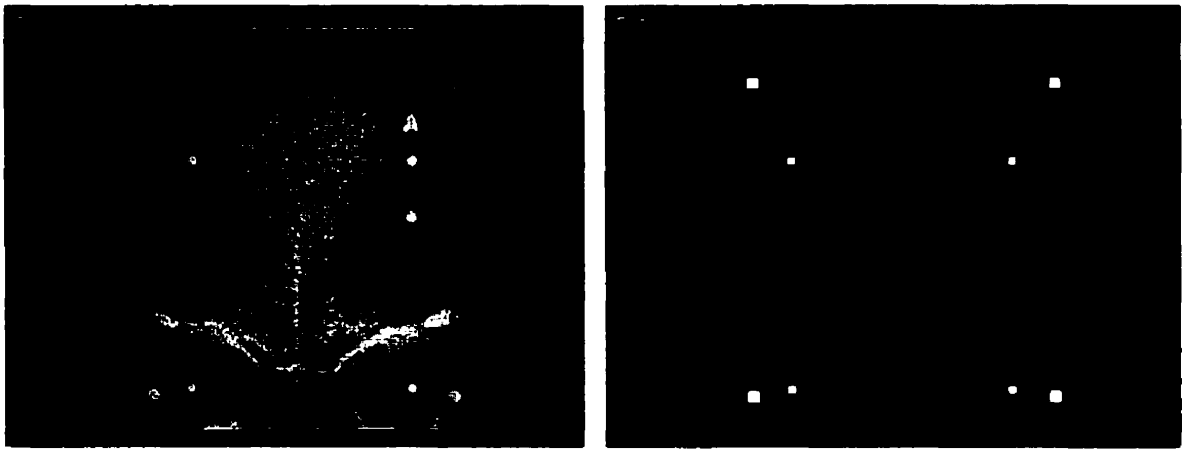

(a) (b)

Figure 35. The positions of the fiducial markers on the image (a) and projected fiducial markers by ray-tracing (b). Since the DSA fiducial markers are user selected, additional errors are introduced in the SVD algorithm and matrix decomposition yielding an error of 1.8 pixels for the ray-tracing algorithm.

3.3 Phantom example

The entire procedure was validated by simulating both 2D and 3D localisation with a specially designed phantom illustrated in Figure 36a.

A CT dataset (Figure 36b) was acquired with a PQ 5000 scanner (Marconi Medical Systems, Cleveland, OH) and the conventional x-ray projection images were acquired with a Therasim 750 simulator (Theratronics, Kanata, Ont), in order to compare 2D and 3D localisation of the aluminium rod tip in the acrylic box.

3.3.1 CT localisation

CT volume localisation was validated with the BrainScan software for both the initial and reformatted volumes (Figure 37). The rod tip, localised at (109.2, 100.4, 65.9) mm within the

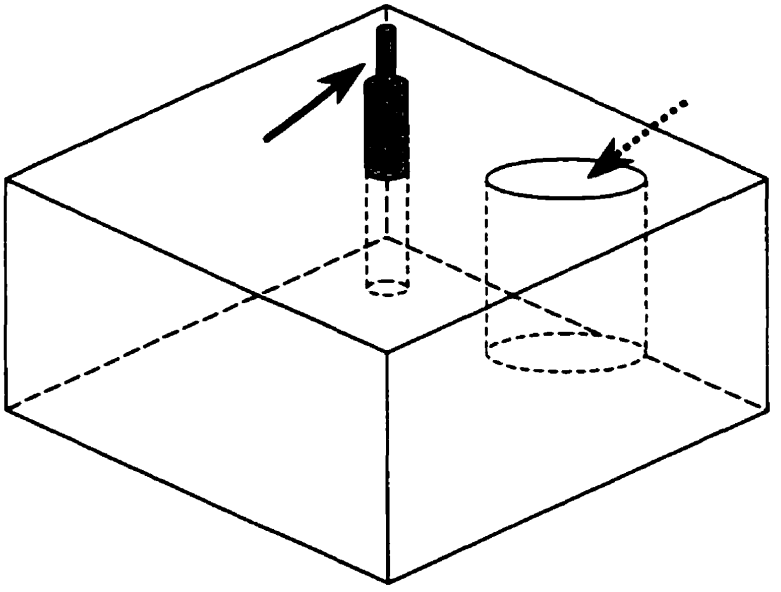

(a)

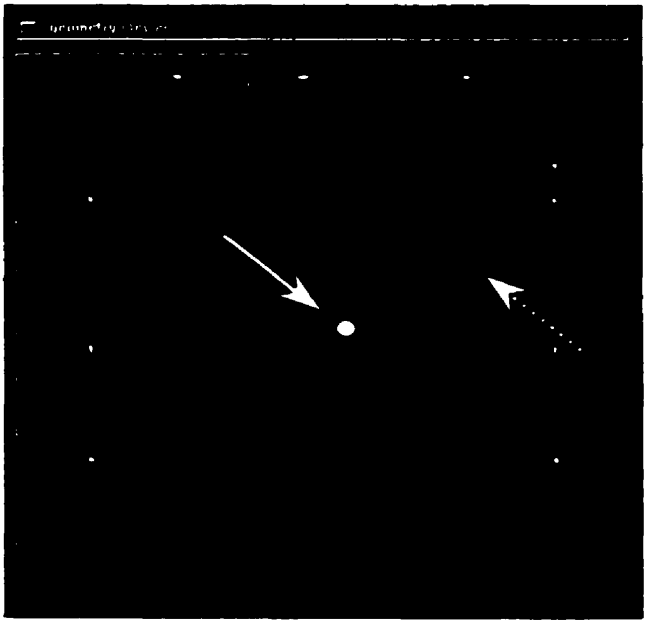

(b)

Figure 36. Phantom employed for the validation. The acrylic box, which was fixed to the stereotactic frame, contains an aluminium rod (solid arrow) as well as an air pocket (dashed arrow) as shown in (a). The air pocket and rod can be visualised on CT images, as shown in (b).

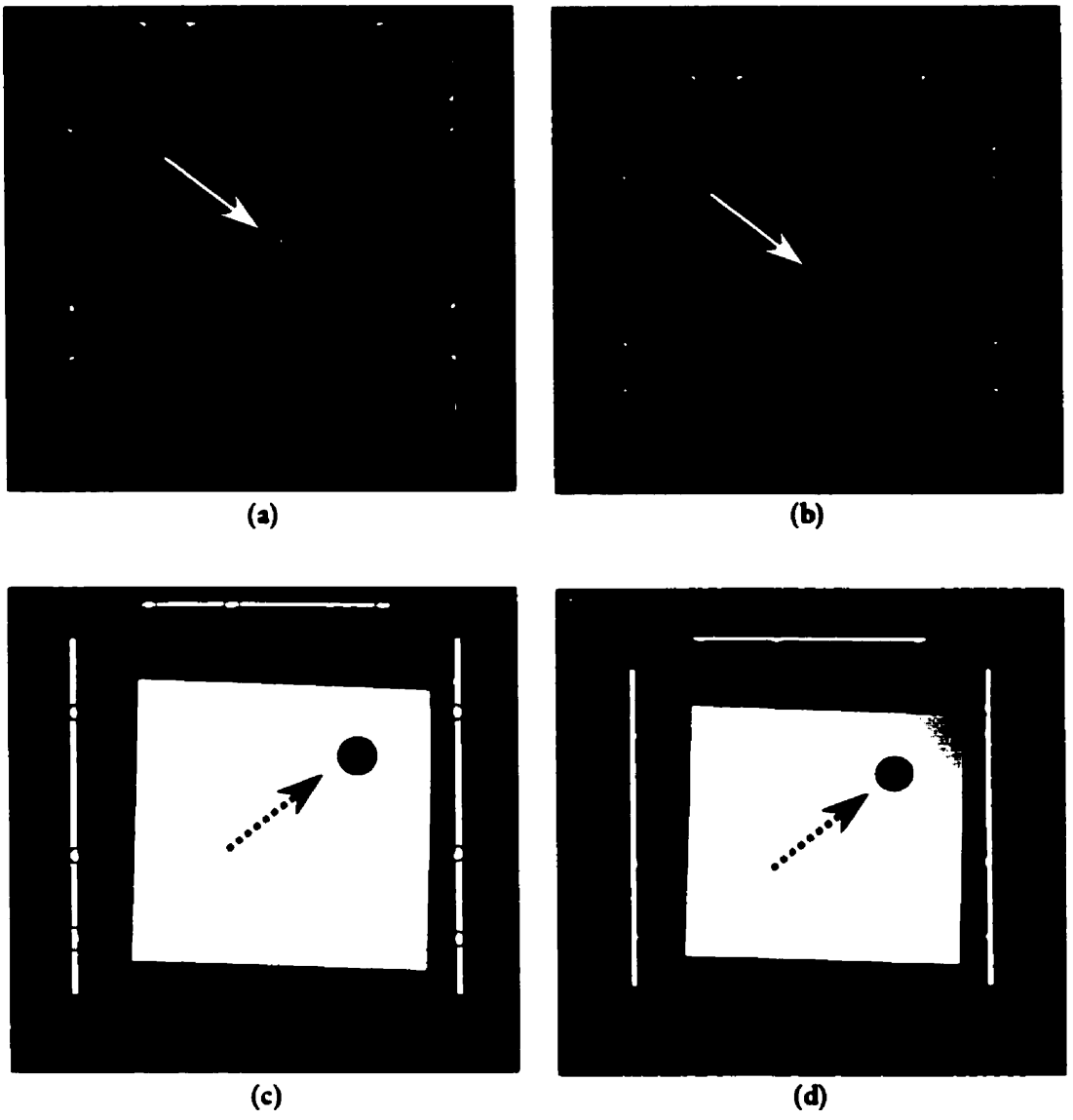

Figure 37. CT volume localisation comparison between the BrainScan software and the developed system. The rod tip and air pocket on the superior surface of the phantom are represented by the solid and dashed arrows respectively. The frame space coordinates of the rod tip and air pocket centre obtained with the BrainScan software (a and c) and the developed system for both the initial (b and d) and reformatted volumes (not shown) are in agreement within 1 mm.

initial volume and at (109.3, 100.5, 66.0) mm within the reformatted volume, is in agreement with the rod tip localised at (108.9, 101.1, 66.1) mm employing the BrainScan software within 1 mm. The location of the air pocket centre on the superior surface of the phantom, localised

at (146.4, 135.9, 83.5) mm and (146.2, 135.9, 83.0) mm within the initial and reformatted volume respectively, is in agreement with the BrainScan software localisation at (146.3, 136.1, 83.7) mm within 1 mm. Since the fiducial markers are user selected, target localisation will differ by a small amount between the two systems.

3.3.2 X-ray projection localisation

Target localisation is performed with the two x-ray projections (Figure 38) employing the method described in section 2.3.2. The aluminium rod tip was localised at (109.0, 100.6, 65.4)

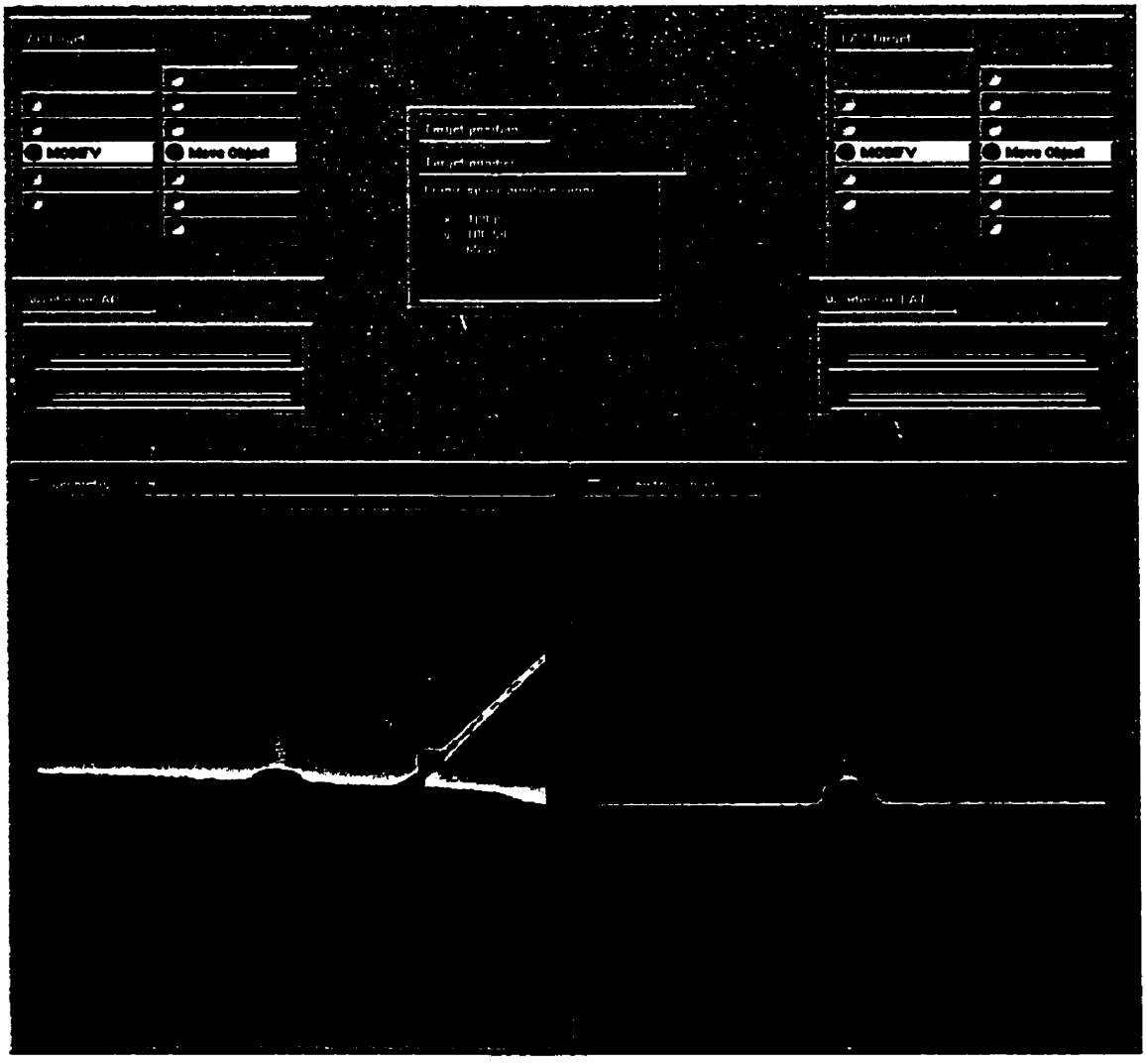

Figure 38. Target localisation panel. The AP (left) and LAT (right) phantom x-ray projections are employed for conventional target localisation. The rod tip was localised at (109.0, 100.6, 65.4) mm.

mm within the stereotactic frame, which is in agreement with the BrainScan software rod tip location given above, yielding a 1 mm difference with the actual location of the rod tip within the frame.

3.3.3 Ray-tracing

Ray-tracing is subsequently executed through the CT volume with the same projection geometry as the x-ray projections. The correlation of the ray-traced images with the x-ray projection images provides a consistency check between the datasets.

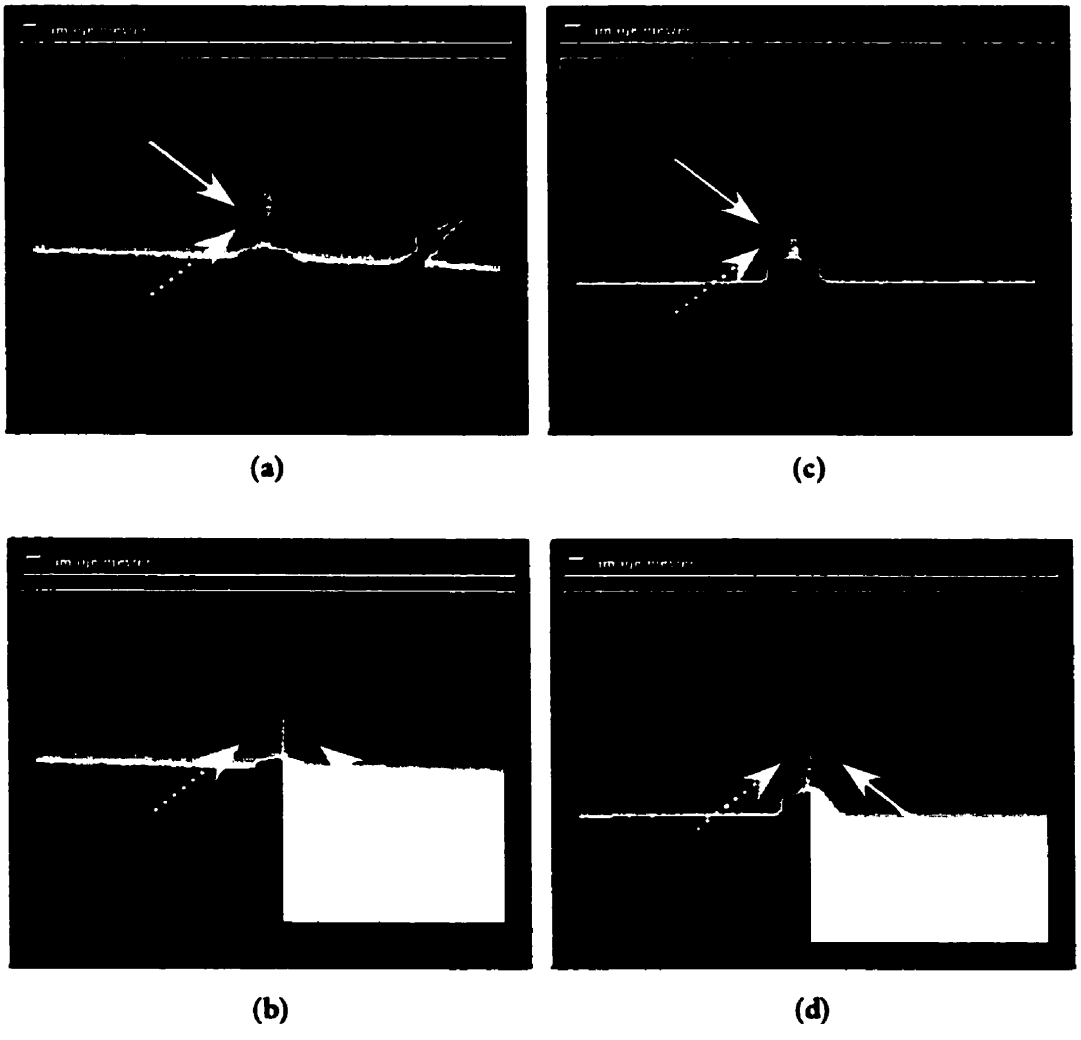

Figure 39. Ray-traced CT images and x-ray projection images. The ray-traced AP (a,b) and LAT (c,d) images (solid arrows) correlate very well visually with the AP (a,b) and LAT (c,d) x-ray projection images (dashed arrows).

As can be seen in Figure 39, the AP and LAT ray-traced images correlate very well visually with the AP and LAT x-ray projection images. The datasets are therefore consistent and the target may be localised and delineated in 3D.

3.3.4 3D target localisation and delineation

Due to the ray-tracing results, the datasets are considered to be consistent and the aluminium rod as well as the air pocket are subsequently localised and delineated in 3D. The contours are

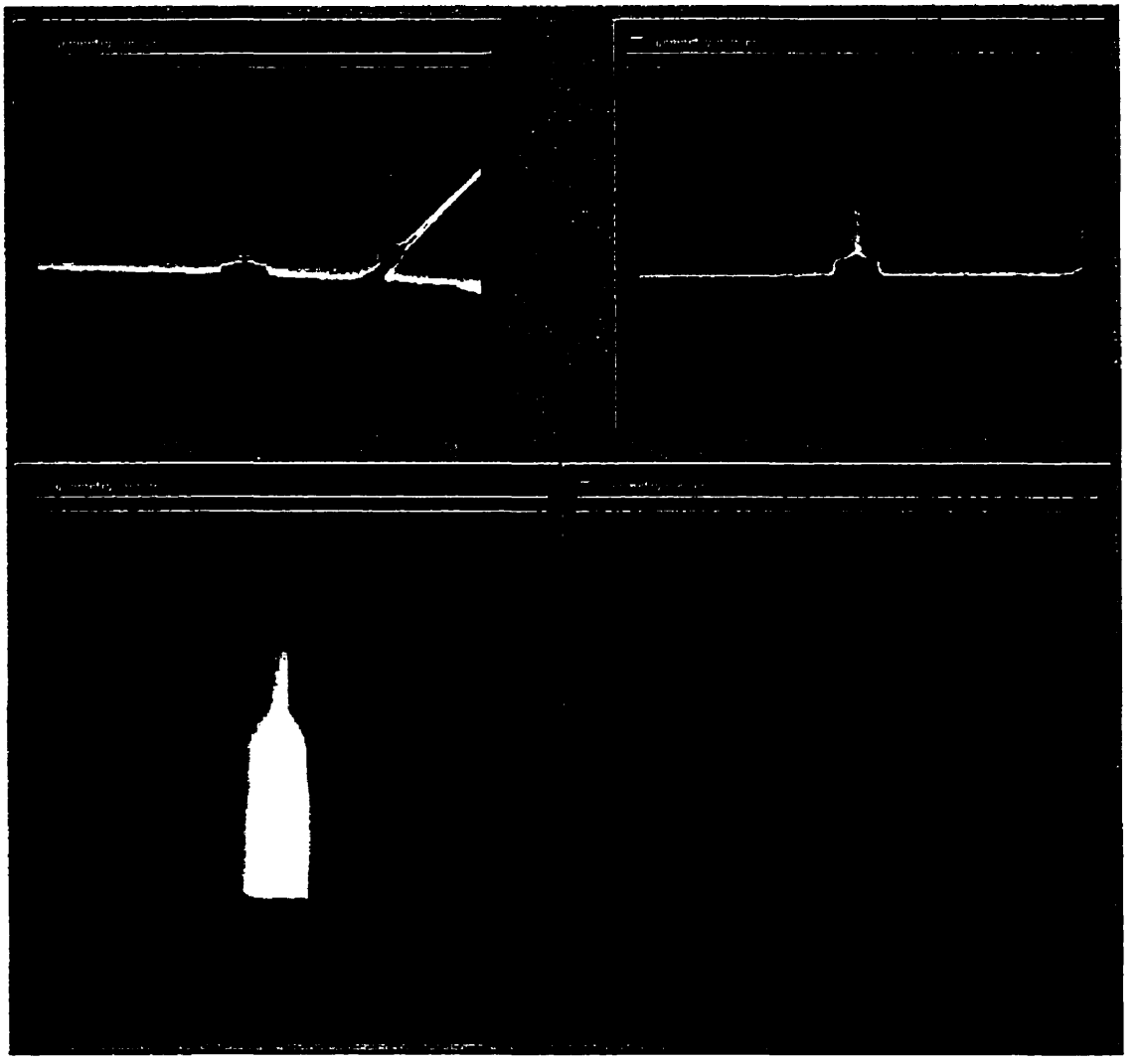

Figure 40. 3D target localisation and delineation panel. The contours (solid arrow) of the rod are drawn within the CT data (bottom left window) and may be simultaneously adjusted due to continuous feedback from the visual correlation of the contour projections (dashed arrows) with the target extent on the x-ray projection images (top left and right windows).

drawn on the CT slices and may be simultaneously adjusted due to continuous feedback from the visual correlation of the contour projections with the target extent on the x-ray projection images. Figure 40 and Figure 41 illustrate the delineation of the rod and the air pocket respectively.

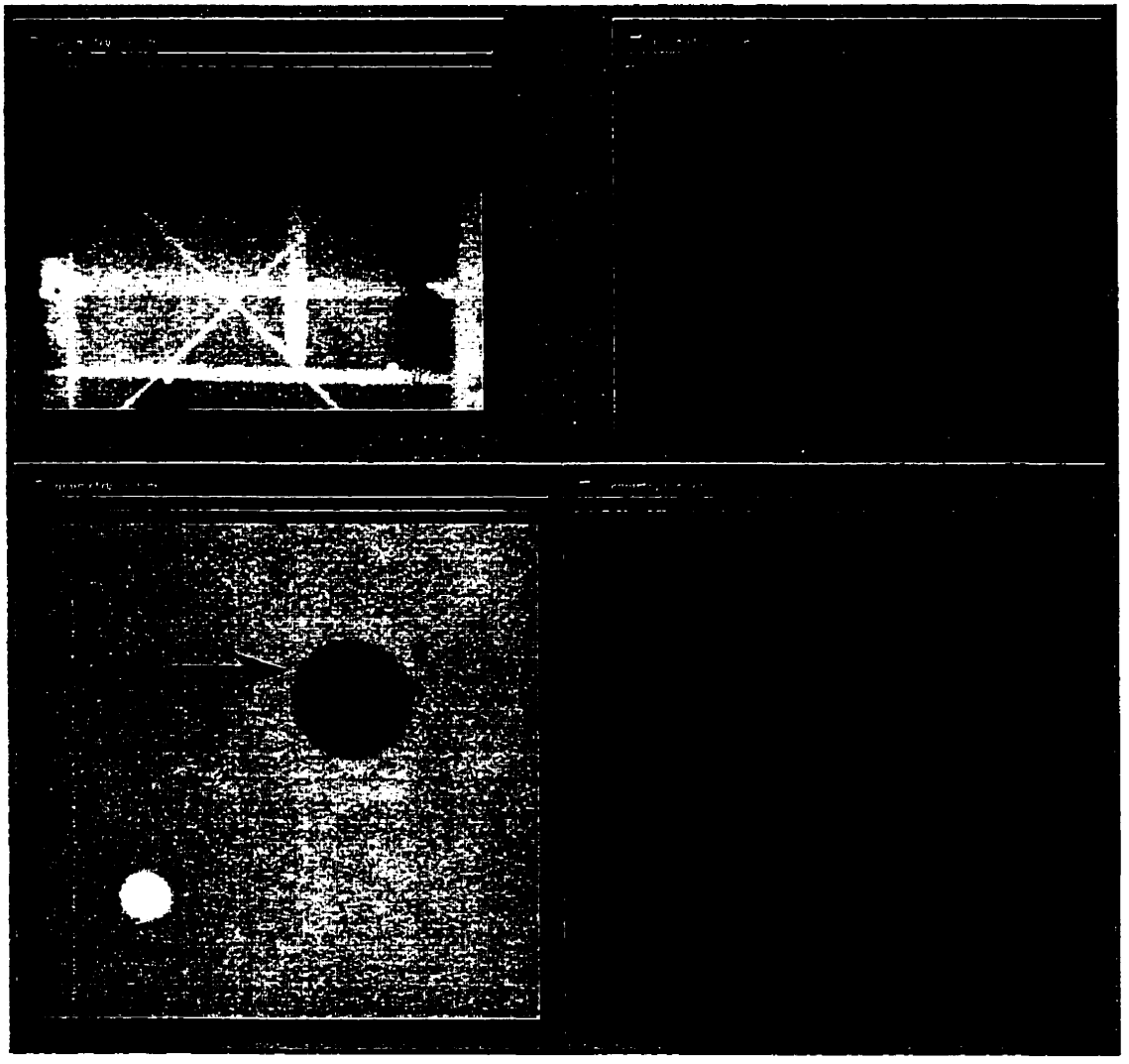

Figure 41. 3D target localisation and delineation panel. The contours (solid arrow) of the air pocket are drawn within the CT data (bottom left window) and may be simultaneously adjusted due to continuous feedback from the visual correlation of the contour projections (dashed arrows) with the target extent on the x-ray projection images (top left and right windows).

The results of Figure 40 are in agreement with the results of the target localisation and ray-tracing correlation. The contour projections of Figure 40 and Figure 41 illustrate good visual correlation between the CT and x-ray projection datasets.

3.4 Patient 1

This patient was previously treated with the McGill dynamic arc radiosurgery technique [11] which delivers almost spherical dose distributions that cannot conform to irregularly shaped

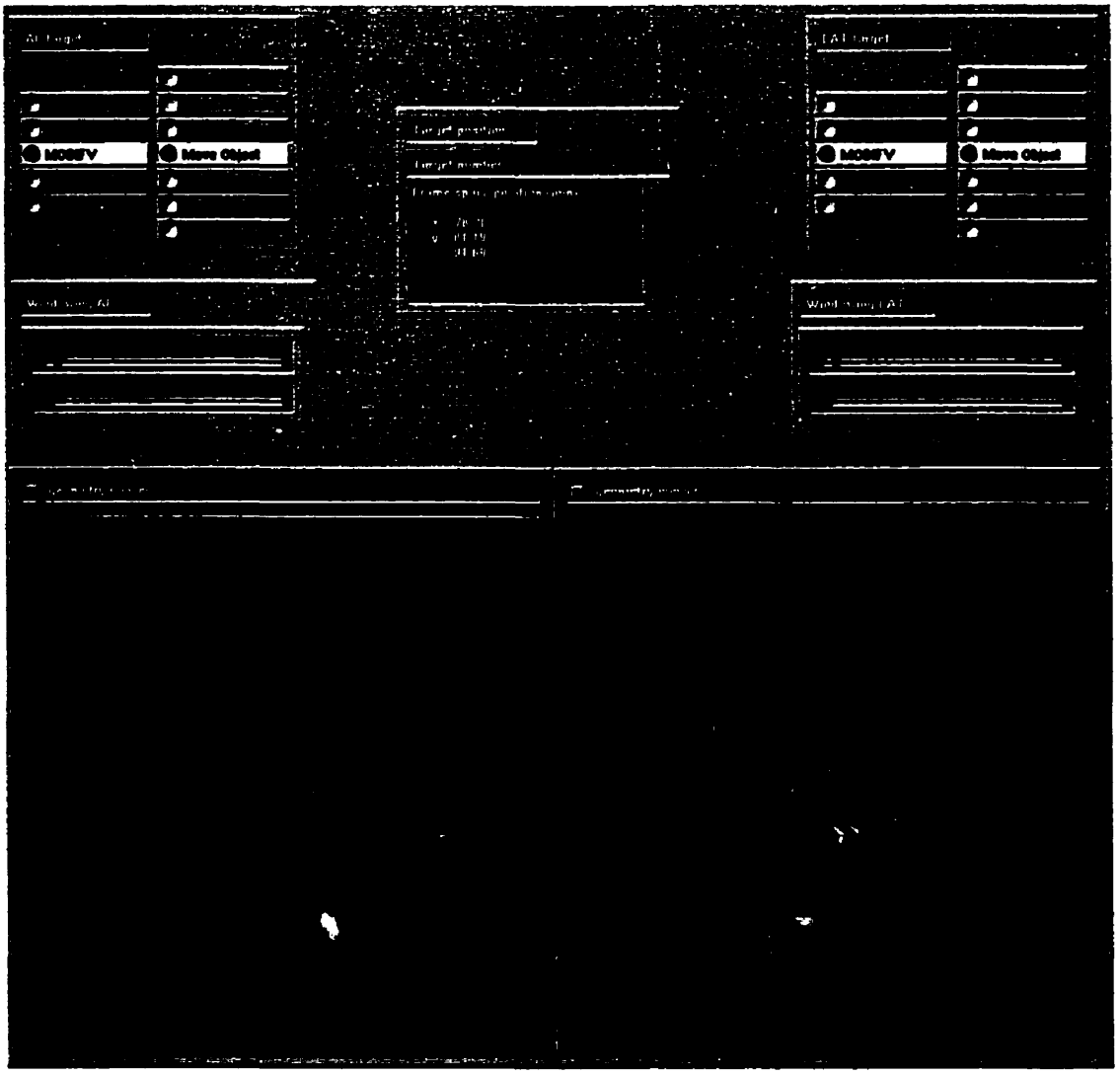

Figure 42. Target localisation panel. The AP (left) and LAT (right) DSA images are employed for conventional target localisation.

targets if only one isocentre is employed. DSA (Figure 42) and MR images were used to localise and plan the treatment of an AVM in the right posterior superior lobe at (7.8, 8.1, 9.1) cm in frame space. An MRA dataset was also acquired at the time of MR scanning employing the 3D TOF technique described in section 1.3.4.

The MR and MRA volumes are fused with the method described in section 2.2. As can be seen on Figure 43, MR images do not provide the vasculature information given by MRA images and MRA images do not provide the anatomical information given by the MR images. The actual treated volume, shown in Figure 43, is positioned at the previously determined AVM coordinates. The volume seems to include healthy tissue which may be due to the

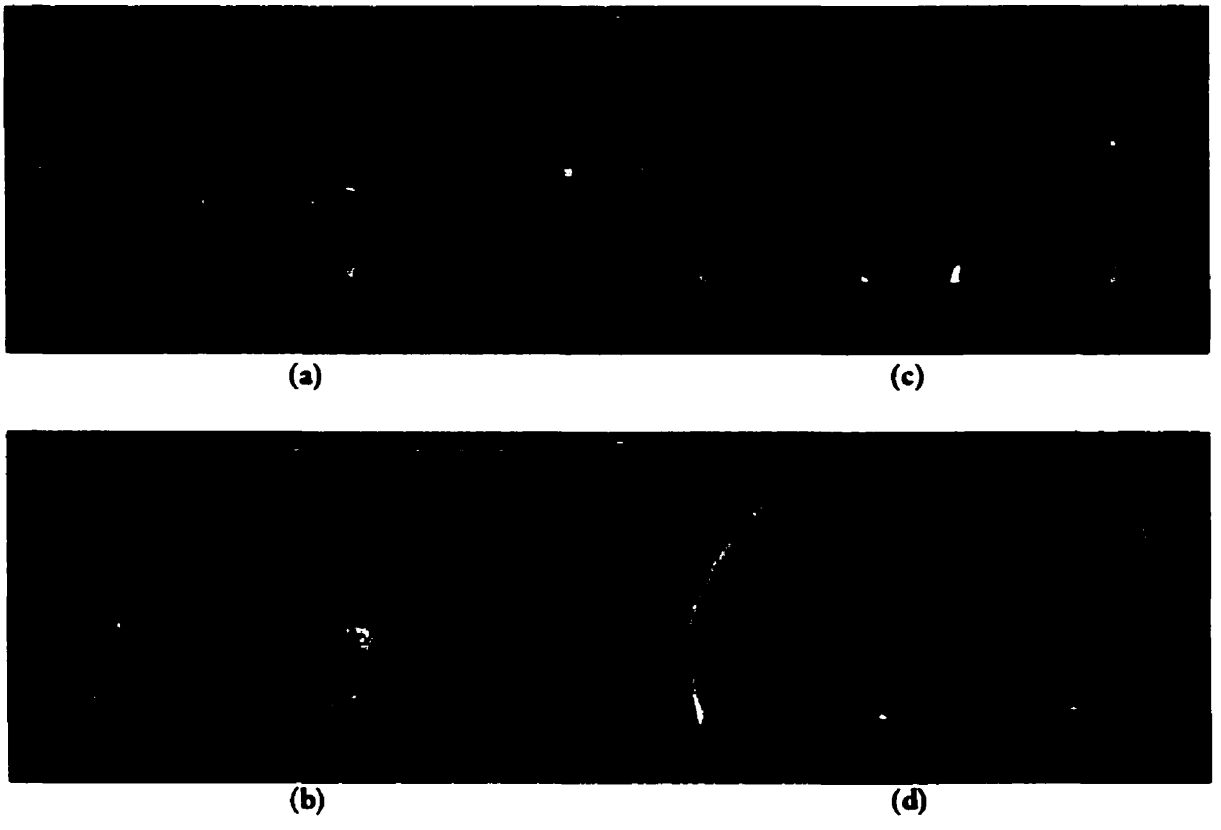

Figure 43. Fused MRA and MR volumes of a patient previously treated with the McGill radiosurgery technique employing only DSA and MR images for which the target was localised at (7.8, 8.1, 9.1) cm in frame space. The MRA coronal (a) and sagittal (b) images are shown with the corresponding MR coronal (c) and sagittal (d) images. The circles on the images illustrate the McGill technique treated volume. The actual treated volume in (a) and (b) seems to include healthy tissue which may be due to the limitations of the DSA localisation method, the treatment technique, or the combination of the two.

limitations of the DSA localisation method, the treatment technique, or the combination of the two.

A comparison of the ray-traced MRA images and DSA images of patient 1 is shown in Figure 44. The AP and LAT ray-traced images correlate very well visually with the AP and LAT DSA images in the vicinity of the AVM. However, there are differences between the images since DSA and MRA offer different vasculature information. The physician must take these considerations into account in the 3D target localisation and delineation process.

(a) (b)

Figure 44. Ray-traced MRA images and DSA images. The AP (a) and LAT (b) ray-traced images (solid arrows) correlate very well visually with the AP (a) and LAT (b) DSA images (dashed arrows) in the vicinity of the AVM. However, there are differences between the images since the modalities offer different vasculature information. The physician must take these considerations into account in the 3D target localisation and delineation process.

A 3D MRA representation of the vasculature is shown in Figure 45. A probe can guide the physician within the fused volumes by projecting its position onto the DSA images. The 3D vascular representation is removed for the contouring process.

The contours of the AVM are subsequently drawn on the MRA slices and simultaneously visualised on the MR slices in order to take the anatomy into account (Figure 46). With continuous feedback, the contours are simultaneously adjusted from the visual correlation of

the contour projections with the AVM extent on the DSA images (Figure 46). Since the contours are drawn on each slice, the AVM target volume is therefore kept at a minimum.

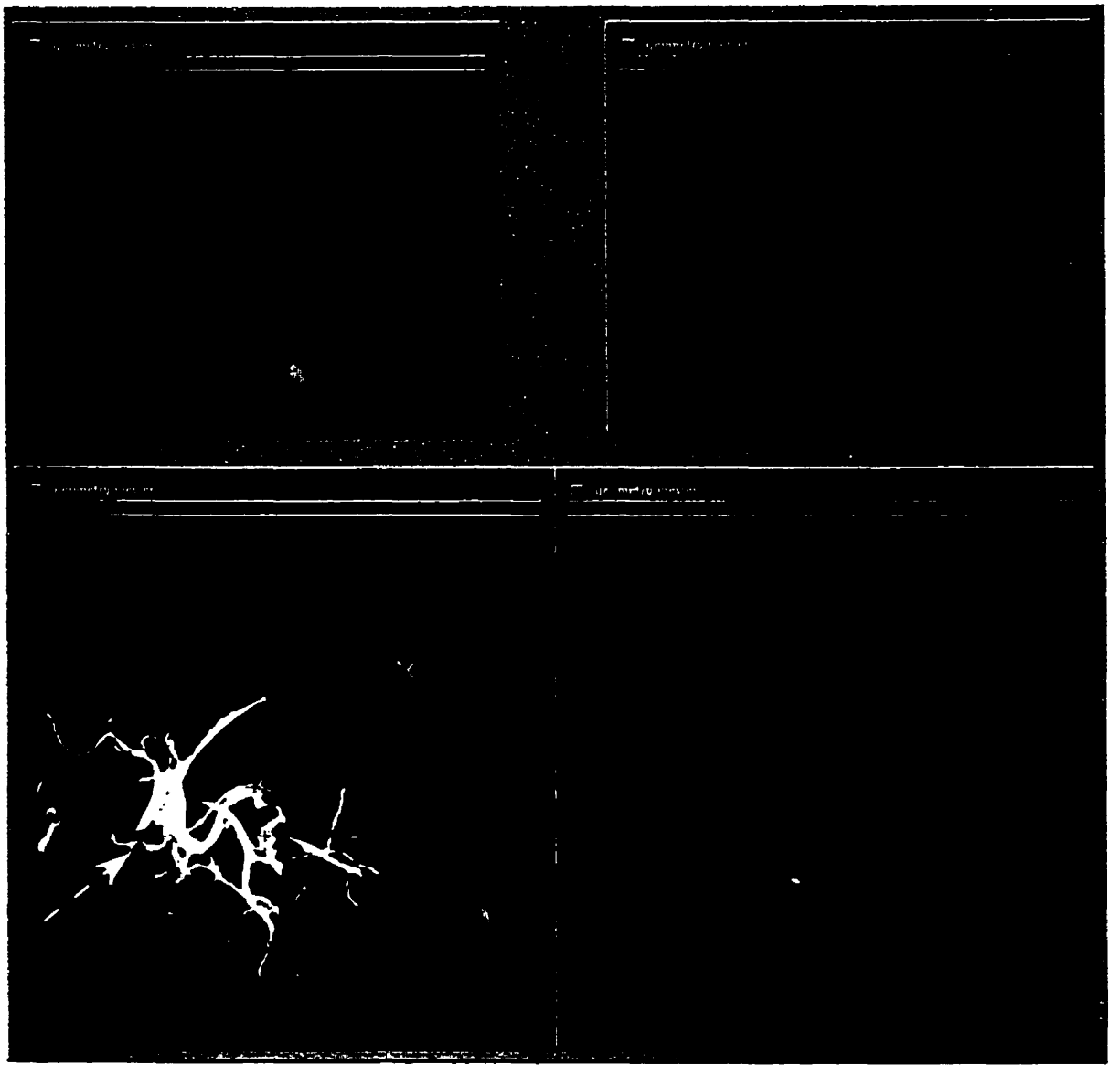

Figure 45. 3D target localisation and delineation panel with probe and 3D vascular representation for patient 1. The MR and DSA images are shown in the bottom right and top windows respectively. The vasculature, shown in the bottom left window by the long-dashed arrow, is superposed onto the MRA images. A probe (solid arrow) guides the physician within the fused volumes by projecting its position (dashed arrows) onto the DSA images. The 3D vascular representation is removed for the contouring process.

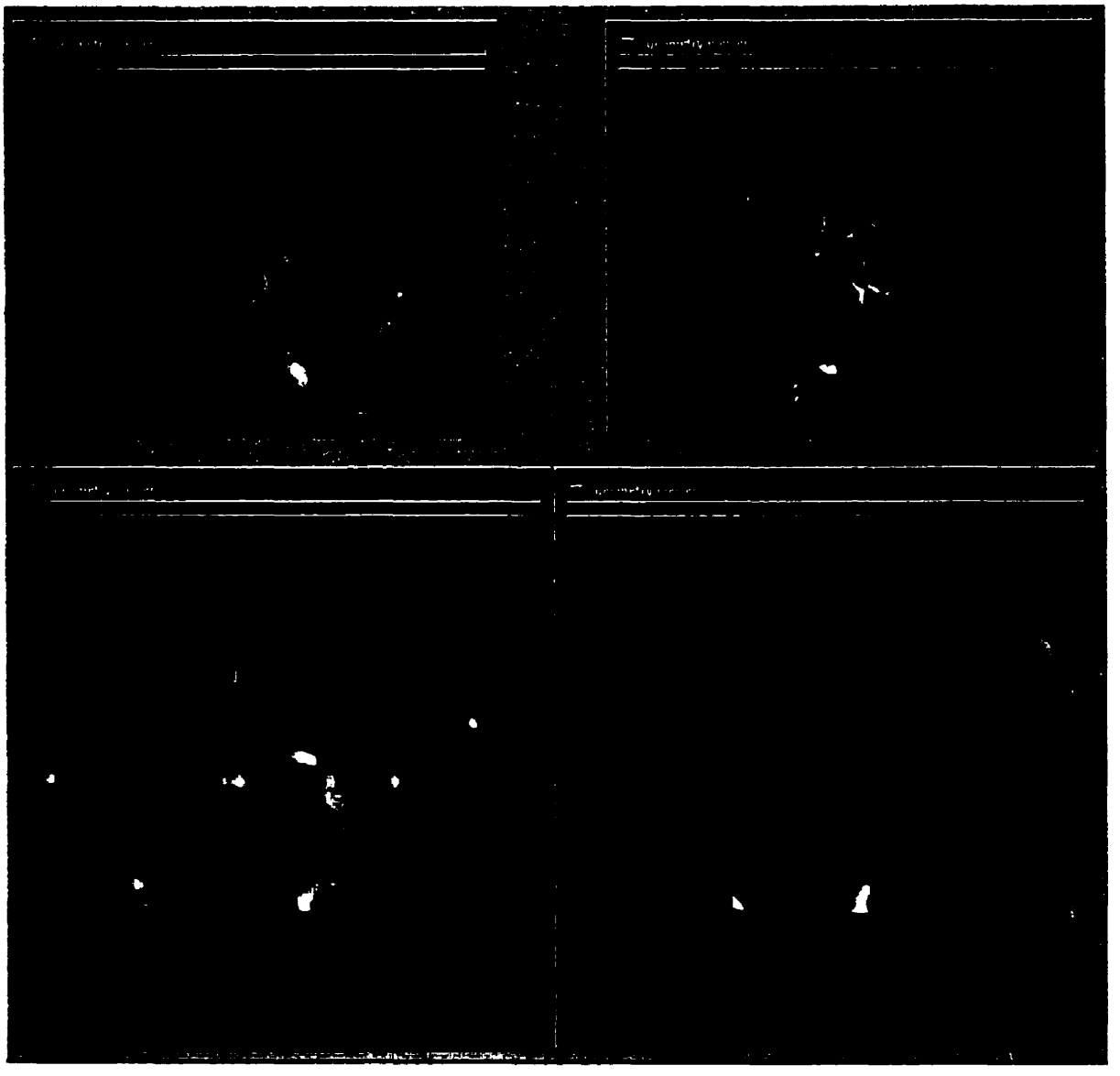

Figure 46. 3D target localisation and delineation panel. The contours, as well as their projections onto the DSA images, are represented by the solid and dashed arrows respectively. The MRA, MR and DSA images are shown in the bottom left, bottom right and top windows respectively. The contour projections correlate well with the AVM extent on the DSA images. Since the contours are drawn on each slice, the target volume is kept at a minimum.

3.5 Patient 2

This patient was also previously treated with the McGill dynamic arc technique [11] employing only DSA (Figure 47) and MR images to treat an AVM in the right posterior superior lobe at

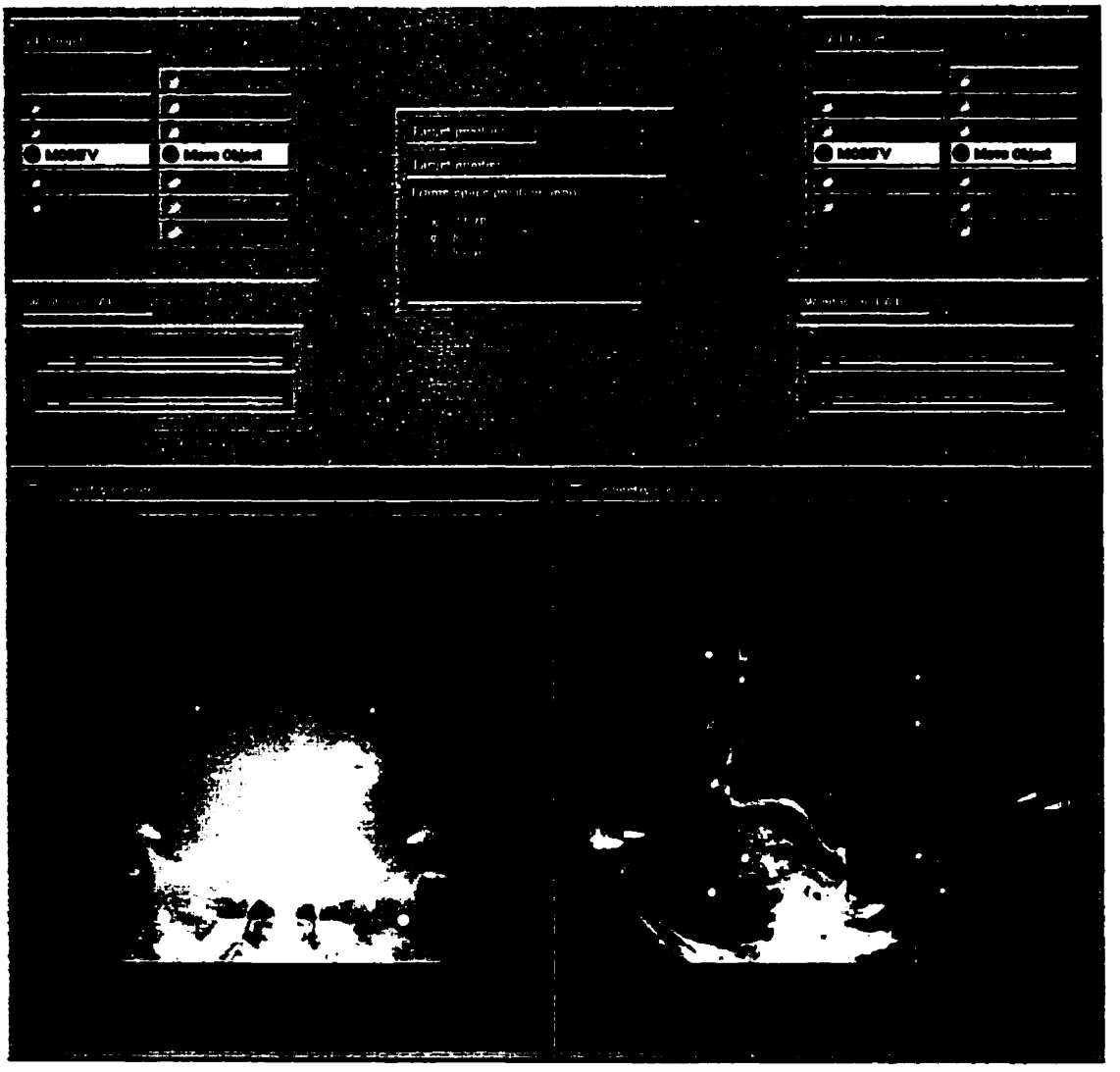

Figure 47. Target localisation panel. The AP (left) and LAT (right) DSA images are employed for conventional target localisation.

(7.7, 6.3, 9.3) cm in frame space. An MRA dataset was also acquired at the time of MR scanning employing the 3D TOF technique.

The actual treated volume, as illustrated in Figure 48, is positioned at the previously determined AVM coordinates. The volume does not seem to include the entire lesion which may be due to the limitations of the DSA localisation method, the treatment technique, or the combination of the two.

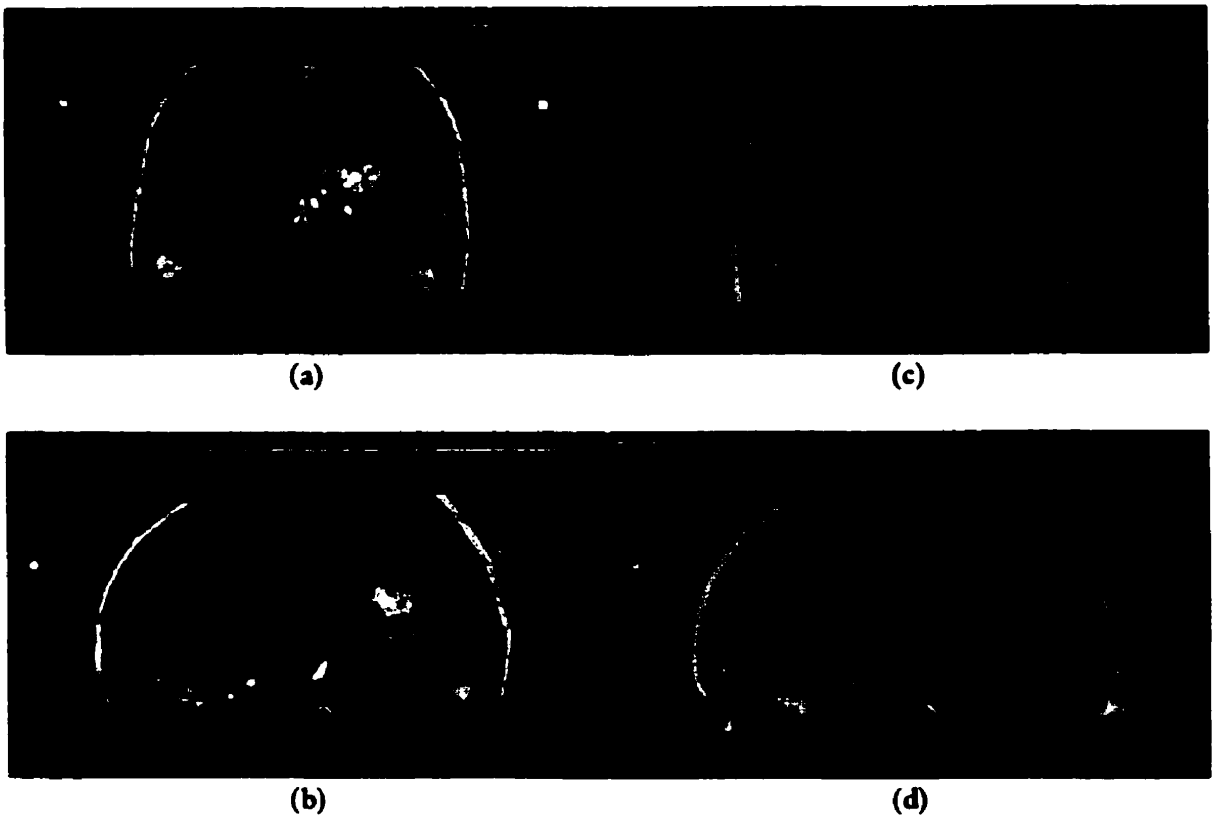

Figure 48. Fused MRA and MR volumes of a patient previously treated with the McGill radiosurgery technique employing only DSA and MR images for which the target was localised at (7.7, 6.3, 9.3) cm in frame space. The MRA coronal (a) and sagittal (b) images are shown with the corresponding MR coronal (c) and sagittal (d) images. The circles on the images illustrate the treated volume by the McGill technique. The treated volume does not seem to include the entire lesion, which may be due to the limitations of the DSA localisation method, the treatment technique, or the combination of the two.

A comparison of the ray-traced MRA images and DSA images of patient 2 is shown in Figure 49. The AP and LAT ray-traced images correlate very well visually with the AP and LAT DSA images. There are differences between the images since the modalities offer different vasculature information. However, the ray-traced MRA images suggest a greater AVM volume and therefore, the physician will take this information into account while drawing the contours.

The AVM is subsequently localised and delineated in the MRA volume (Figure 50). The contour projections, which correlate well with the AVM extent on the DSA images, suggest a

greater AVM volume than shown on the DSA images which is in agreement with the ray-tracing. Since the contours are drawn on each slice, the target volume conforms to the target.

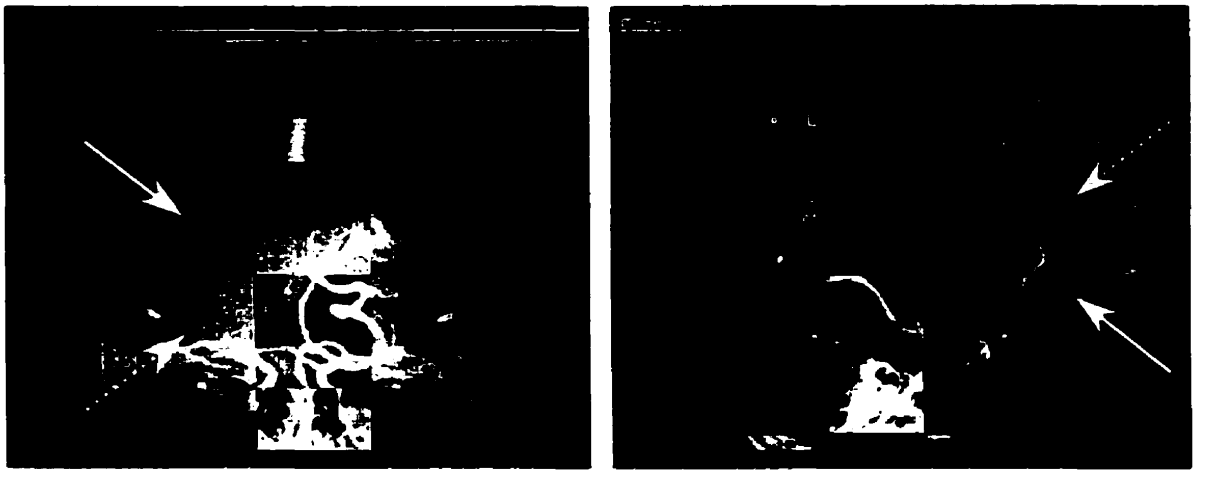

(a) (b)

Figure 49. Ray-traced MRA images and DSA images. The AP (a) and LAT (b) ray-traced images (solid arrows) correlate very well visually with the AP and LAT DSA images (dashed arrows). There are differences between the images since the modalities offer different vasculature information. However, the ray-traced MRA images suggest a greater AVM volume. The physician will therefore take these considerations into account while drawing the contours.

3.6 Summary

In this chapter, the developed system tools were validated and examples of their application in clinical cases were presented. The 3D MRA/MR/CT and 2D DSA target localisation processes were validated by comparing the results obtained with the developed system to those obtained with a clinically used in-house treatment planning software [62, 63]. Employing ten prominent anatomical features, the 3D localisation process presented an average difference in distance between points of 0.7 ± 0.2 mm and of 0.7 ± 0.3 mm for the initial images and reformatted images respectively. The 2D localisation process was validated with eleven prominent image features of a previously obtained phantom study presenting an average difference in distance between points of 0.7 ± 0.4 mm. The ray-tracing process was validated by evaluating the error between the image fiducial marker positions and the positions of the

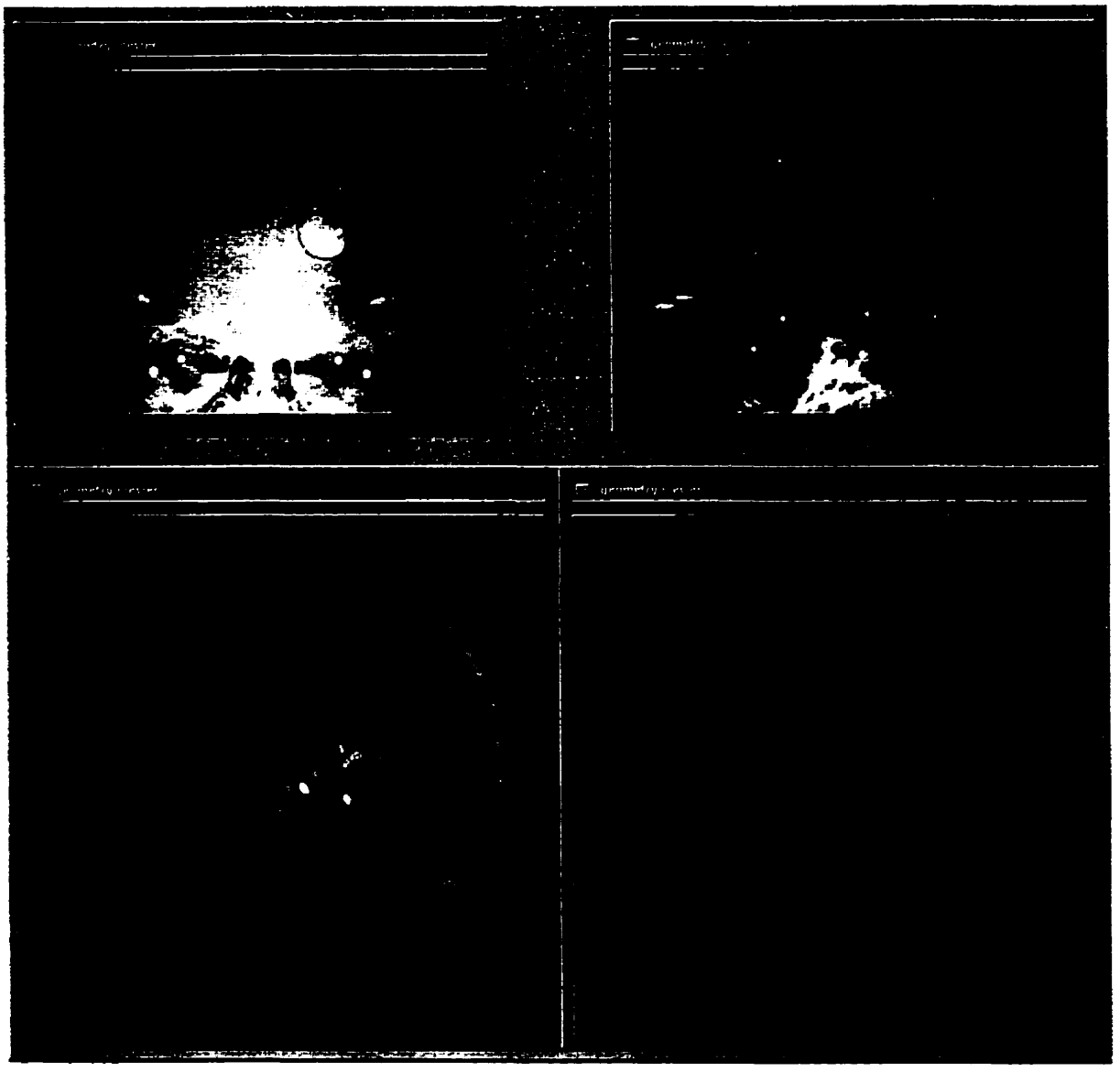

Figure 50. 3D target localisation and delineation panel. The contours, as well as their projections onto the DSA images, are represented by the solid and dashed arrows respectively. The MRA, MR and DSA images are shown in the bottom left, bottom right and top windows respectively. The projected contours, which suggest a greater AVM volume than shown on the DSA images, may be adjusted in order to include the missing lesion portions from the actual treated volume.

projected fiducial markers as predicted by (1) the SVD algorithm with the projection matrix of equation (5), (2) the matrix decomposition employing equation (21) and (3) the ray-tracing algorithm [58]. Six projection geometries, yielding a total of forty-eight points, were evaluated

and systematic errors of 0.5 pixels, 1.6 pixels and 1.8 pixels were introduced by the SVD algorithm, matrix decomposition and ray-tracing algorithm respectively. The contour projections on the DSA images were validated by the results of the SVD algorithm error in the ray-tracing validation since the error corresponds to a comparison between image positions and projected frame positions.

A phantom example validated the entire procedure by comparing results obtained with the developed system to those obtained by the clinically commissioned BrainScan software (BrainLab, Heimstetten, Germany) as well as by performing a visual check of the rod position within the frame.

The chapter also presented two clinical examples of patients which have previously undergone radiosurgery and that have been planned with the McGill dynamic arc radiosurgery technique employing DSA and MR images. Target volumes obtained from the 3D delineation within the fused volumes seem to differ from the treated volumes. A difference in volumes can have significant dosimetric implications particularly for large AVMs.

Chapter Four

4 SUMMARY AND FUTURE WORK

4.1 Summary

A multimodality image fusion and localisation system for radiosurgery treatments of arteriovenous malformations (AVM) has been developed and validated. Within this system, tools have been developed for:

I. Fusion of 3D datasets (MRA/CTA & MR/CT) in order to combine vascular and anatomical information. Head contours are needed for radiosurgery planning and image fusion makes the data of all these techniques available for localisation and planning.

II. Simulation of projections through the 3D datasets described in (I) above employing the projection geometry of the x-ray angiograms. A comparison between the numerically projected 2D images and the x-ray angiograms, as well as the projection of the contours drawn on the MRA dataset onto the angiograms, provide a visual check of potential errors that may be introduced during MRA localisation and definition of the AVM.

Since organ contours are drawn on the MRA images, simultaneously visualised on their MR/CT counterparts, and projected onto the DSA images for visual feedback, the system

allows users to incorporate both vascular and anatomical information in the three-dimensional target localisation and delineation process.

The developed tools have been validated and have proven to be robust. The 3D MRA/MR/CT and 2D DSA target localisation processes were validated by comparing the results obtained with the developed system to those obtained with a clinically used in-house treatment planning software [62, 63]. The volume localisation process presented an average difference in distance between points of 0.7 ± 0.2 mm and of 0.7 ± 0.3 mm for the initial images and reformatted images respectively. This comparison was established with prominent anatomical features. The 2D localisation process presented an average difference in distance between points of 0.7 ± 0.4 mm. Since the fiducial markers are user selected, the target locations are expected to differ by a small amount between the two systems. The ray-tracing process was validated by evaluating the error between the image fiducial marker positions and the positions of the projected fiducial markers as predicted by (1) the SVD algorithm with the projection matrix of equation (5), (2) the matrix decomposition employing equation (21) and (3) the ray-tracing algorithm [58]. Six projection geometries, yielding a total of forty-eight points, were evaluated and systematic errors of 0.5 pixels, 1.6 pixels and 1.8 pixels were introduced by the SVD algorithm, matrix decomposition and ray-tracing algorithm respectively. A phantom example, which validated the entire procedure, was presented.

Two clinical examples of patients which had previously undergone radiosurgery and that had been planned with the McGill technique employing DSA and MR images were presented. Target volumes obtained from the 3D delineation within the fused volumes may differ from the treated volumes. A difference in volumes can have significant dosimetric implications particularly for large AVMs.

4.2 Future work

A potential improvement to the system is to automate the fiducial marker selection for the DSA, MR and CT images in order to increase the efficiency of the process. Another potential improvement is to incorporate an anatomical fusion tool in order to optimise anatomy matching between the 3D datasets.

Patients that had previously undergone radiosurgery for AVMs are to be replanned within this system in order to evaluate the dosimetric implications of the difference in volumes due to the use of 3D information within the system. Since the target volumes obtained from the 3D delineation within the fused volumes seem to differ from the treated volumes, the volume differences can be significant for large, complexly shaped AVMs, and will have to be evaluated. Provided that these differences are indeed found significant, a link between the developed system and the treatment planning system must therefore be established in order to transfer the contours drawn on the reformatted MRA volume to the treatment planning system to evaluate the dosimetric implications of these findings.

References

[1] G. Hademenos, Massoud, Tarik F., *The Physics of Cerebrovascular Diseases: Biophysical Mechanisms of Development, Diagnosis and Therapy*. New York: AIP Press, Springer-Verlag, 1998.

[2] A. Luessenhop, "Natural History of Cerebral Arteriovenous Malformations," in *Intracranial Arteriovenous Malformations, Current Neurosurgical Practise*, C. Wilson, Stein, BM., Ed. Baltimore: Williams and Wilkins, 1984, pp. 12-23.

[3] V. B. Graves and T. A. Duff, "Intracranial arteriovenous malformations. Current imaging and treatment," *Investigative Radiology*, vol. 25, pp. 952-60, 1990.

[4] B. E. Pollock, "Stereotactic radiosurgery for arteriovenous malformations," *Neurosurg Clin N Am*, vol. 10, pp. 281-90, 1999.

[5] R. C. Wallace and E. C. Bourekas, "Brain arteriovenous malformations," *Neuroimaging Clin N Am*, vol. 8, pp. 383-99, 1998.

[6] A. Nanda, "Controversies in neurosurgery: microsurgery versus radiosurgery for arteriovenous malformations--introduction," *Clin Neurosurg*, vol. 45, pp. 11-2, 1999.

[7] P. J. Porter, A. Y. Shin, A. S. Detsky, L. Lefaive, and M. C. Wallace, "Surgery versus stereotactic radiosurgery for small, operable cerebral arteriovenous malformations: a clinical and cost comparison," *Neurosurgery*, vol. 41, pp. 757-64; discussion 764-6, 1997.

[8] D. L. Barrow, "Controversies in neurosurgery: microsurgery versus radiosurgery for arteriovenous malformations--the case for microsurgery," *Clin Neurosurg*, vol. 45, pp. 13-7, 1999.

[9] J. P. Deveikis, "Endovascular therapy of intracranial arteriovenous malformations. Materials and techniques," *Neuroimaging Clin N Am*, vol. 8, pp. 401-24, 1998.

[10] D. Bourque, "Static conformal fields in stereotactic radiosurgery," in *Medical Physics Unit*. Montreal: McGill, 1997, pp. 140.

[11] E. B. Podgorsak, A. Olivier, M. Pla, P. Y. Lefebvre, and J. Hazel, "Dynamic stereotactic radiosurgery," *International Journal of Radiation Oncology, Biology, Physics*, vol. 14, pp. 115-26, 1988.

[12] P. P. Kesava and P. A. Turski, "MR angiography of vascular malformations," *Neuroimaging Clinics of North America*, vol. 8, pp. 349-70, 1998.

[13] W. A. Friedman, "Radiosurgery versus surgery for arteriovenous malformations: the case for radiosurgery," *Clin Neurosurg*, vol. 45, pp. 18-20, 1999.

[14] T. L. Ellis, W. A. Friedman, F. J. Bova, P. S. Kubilis, and J. M. Buatti, "Analysis of treatment failure after radiosurgery for arteriovenous malformations," *J Neurosurg*, vol. 89, pp. 104-10, 1998.

[15] P. Gallina, L. Merienne, J. F. Meder, M. Schlienger, D. Lefkopoulos, and J. J. Merland, "Failure in radiosurgery treatment of cerebral arteriovenous malformations," *Neurosurgery*, vol. 42, pp. 996-1002; discussion 1002-4, 1998.

[16] W. Y. Guo, B. Nordell, B. Karlsson, M. Soderman, M. Lindqvist, K. Ericson, A. Franck, I. Lax, and C. Lindquist, "Target delineation in radiosurgery for cerebral arteriovenous malformations. Assessment of the value of stereotaxic MR imaging and MR angiography," *Acta Radiol*, vol. 34, pp. 457-63, 1993.

[17] F. J. Bova and W. A. Friedman, "Stereotactic angiography: an inadequate database for radiosurgery?," *International Journal of Radiation Oncology, Biology, Physics*, vol. 20, pp. 891-5, 1991.

[18] G. Bednarz, B. Downes, M. Werner-Wasik, and R. H. Rosenwasser, "Combining stereotactic angiography and 3D time-of-flight magnetic resonance angiography in treatment planning for arteriovenous malformation radiosurgery," *International Journal of Radiation Oncology, Biology, Physics*, vol. 46, pp. 1149-54, 2000.

[19] J. Klisch, R. Strecker, J. Hennig, and M. Schumacher, "Time-resolved projection MRA: clinical application in intracranial vascular malformations," *Neuroradiology*, vol. 42, pp. 104-7, 2000.

[20] K. Takano, H. Utsunomiya, H. Ono, M. Okazaki, and A. Tanaka, "Dynamic contrast-enhanced subtraction MR angiography in intracranial vascular abnormalities," *European Radiology*, vol. 9, pp. 1909-12, 1999.

[21] J. C. Steffens, J. Link, and M. Heller, "Contrast-enhanced magnetic resonance angiography of the cervical arteries. A review," *Invest Radiol*, vol. 33, pp. 573-7, 1998.

[22] G. Marchal, H. Bosmans, L. Van Fraeyenhoven, G. Wilms, P. Van Hecke, C. Plets, and A. L. Baert, "Intracranial vascular lesions: optimization and clinical evaluation of three-dimensional time-of-flight MR angiography," *Radiology*, vol. 175, pp. 443-8, 1990.

[23] Y. Suzuki and K. Matsumoto, "[Detection of the venous system of the skull base using three-dimensional CT angiography (3D-CTA): utility of the subtemporal approach]," *No Shinkei Geka - Neurological Surgery*, vol. 28, pp. 17-22, 2000.

[24] G. B. Anderson, D. E. Steinke, K. C. Petruk, R. Ashforth, and J. M. Findlay, "Computed tomographic angiography versus digital subtraction angiography for the diagnosis and early treatment of ruptured intracranial aneurysms," *Neurosurgery*, vol. 45, pp. 1315-20; discussion 1320-2, 1999.

[25] T. Okuyama, K. Saito, A. Hirano, A. Takahashi, T. Inagaki, and S. Inamura, "[Improvement of MRA and 3D-CTA does away with the need for cerebral angiography in many cerebral aneurysm operations]," *No Shinkei Geka - Neurological Surgery*, vol. 26, pp. 607-12, 1998.

[26] H. Tanaka, Y. Numaguchi, S. Konno, D. A. Shrier, D. K. Shibata, and U. Patel, "Initial experience with helical CT and 3D reconstruction in therapeutic planning of cerebral AVMs: comparison with 3D time-of-flight MRA and digital subtraction angiography," *Journal of Computer Assisted Tomography*, vol. 21, pp. 811-7, 1997.

[27] R. P. Levy, R. W. Schulte, K. A. Frankel, G. K. Steinberg, M. P. Marks, B. Lane, L. H. Heilbronn, H. J. Meinass, R. A. Galindo, J. D. Slater, and J. M. Slater, "Computed tomography slice-by-slice target-volume delineation for stereotactic proton irradiation of large intracranial arteriovenous malformations: an iterative approach using angiography, computed tomography, and magnetic resonance imaging," *Int J Radiat Oncol Biol Phys*, vol. 35, pp. 555-64, 1996.

[28] V. S. Khoo, E. J. Adams, F. Saran, J. L. Bedford, J. R. Perks, A. P. Warrington, and M. Brada, "A Comparison of clinical target volumes determined by CT and MRI for the radiotherapy planning of base of skull meningiomas," *International Journal of Radiation Oncology, Biology, Physics*, vol. 46, pp. 1309-17, 2000.

[29] R. J. Amdur, D. Gladstone, K. A. Leopold, and R. D. Harris, "Prostate seed implant quality assessment using MR and CT image fusion," *International Journal of Radiation Oncology, Biology, Physics*, vol. 43, pp. 67-72, 1999.

[30] J. P. Lattanzi, D. A. Fein, S. W. McNeeley, A. H. Shaer, B. Movsas, and G. E. Hanks, "Computed tomography-magnetic resonance image fusion: a clinical evaluation of an innovative approach for improved tumor localization in primary central nervous system lesions," *Radiation Oncology Investigations*, vol. 5, pp. 195-205, 1997.

[31] K. Kagawa, W. R. Lee, T. E. Schultheiss, M. A. Hunt, A. H. Shaer, and G. E. Hanks, "Initial clinical assessment of CT-MRI image fusion software in localization of the prostate for 3D conformal radiation therapy," *International Journal of Radiation Oncology, Biology, Physics*, vol. 38, pp. 319-25, 1997.

[32] H. Y. Lau, K. Kagawa, W. R. Lee, M. A. Hunt, A. H. Shaer, and G. E. Hanks, "Short communication: CT-MRI image fusion for 3D conformal prostate radiotherapy: use in patients with altered pelvic anatomy," *British Journal of Radiology*, vol. 69, pp. 1165-70, 1996.

[33] M. C. Schell, Bova, F.J., Larson, D.A., Leavitt, D.D., Lutz, W.R., Podgorsak, E.B., Wu, A., "Stereotactic Radiosurgery," , Woodbury AAPM Report No. 54, June 1995.

[34] E. Podgorsak, Podgorsak, MB., "Stereotactic Irradiation," in *The Modern Technology of Radiation Oncology*, J. V. Dyk, Ed. Madison: Medical Physics Publishing, 1999, pp. 1072.

[35] D. R. Blatt, W. A. Friedman, and F. J. Bova, "Modifications based on computed tomographic imaging in planning the radiosurgical treatment of arteriovenous malformations," *Neurosurgery*, vol. 33, pp. 588-95; discussion 595-6, 1993.

[36] J. I. Fabrikant, R. P. Levy, G. K. Steinberg, M. H. Phillips, K. A. Frankel, J. T. Lyman, M. P. Marks, and G. D. Silverberg, "Charged-particle radiosurgery for intracranial vascular malformations," *Neurosurg Clin N Am*, vol. 3, pp. 99-139, 1992.

[37] J. T. Bushberg, Seibert, J. A., Leidholdt, E. M., Boone, J. M., *The Essential Physics of Medical Imaging*. Baltimore: Williams and Wilkins, 1994.

[38] A. Macovski, *Medical Imaging Systems*. Englewood Cliffs: Prentice-Hall, 1983.

[39] M. O. Leach, "Spatially Localised Nuclear Magnetic Resonance," in *The Physics of Medical Imaging, Medical Science*, S. Webb, Ed. New York: IOP, 1988, pp. 633.

[40] V. S. Khoo, D. P. Dearnaley, D. J. Finnigan, A. Padhani, S. F. Tanner, and M. O. Leach, "Magnetic resonance imaging (MRI): considerations and applications in radiotherapy treatment planning," *Radiother Oncol*, vol. 42, pp. 1-15, 1997.

[41] G. Bednarz, M. B. Downes, B. W. Corn, W. J. Curran, and H. W. Goldman, "Evaluation of the spatial accuracy of magnetic resonance imaging-based stereotactic target localization for gamma knife radiosurgery of functional disorders," *Neurosurgery*, vol. 45, pp. 1156-61; discussion 1161-3, 1999.

[42] C. Maurer, G. B. Aboutanos, B. M. Dawant, S. Gadamsetty, R. A. Margolin, R. J. Maciunas, and J. M. Fitzpatrick, "Effect of geometrical distortion correction in MR on image registration accuracy," *J Comput Assist Tomogr*, vol. 20, pp. 666-79, 1996.

[43] D. Dean, J. Kamath, J. L. Duerk, and E. Ganz, "Validation of object-induced MR distortion correction for frameless stereotactic neurosurgery," *IEEE Trans Med Imaging*, vol. 17, pp. 810-6, 1998.

[44] L. Walton, A. Hampshire, D. M. Forster, and A. A. Kemeny, "A phantom study to assess the accuracy of stereotactic localization, using T1-weighted magnetic resonance imaging with the Leksell stereotactic system," *Neurosurgery*, vol. 38, pp. 170-6; discussion 176-8, 1996.

[45] J. Michiels, H. Bosmans, P. Pelgrims, D. Vandermeulen, J. Gybels, G. Marchal, and P. Suetens, "On the problem of geometric distortion in magnetic resonance images for stereotactic neurosurgery," *Magn Reson Imaging*, vol. 12, pp. 749-65, 1994.

[46] C. J. Bakker, M. A. Moerland, R. Bhagwandien, and R. Beersma, "Analysis of machine-dependent and object-induced geometric distortion in 2DFT MR imaging," *Magn Reson Imaging*, vol. 10, pp. 597-608, 1992.

[47] R. J. Maciunas, J. M. Fitzpatrick, S. Gadamsetty, and C. R. Maurer, Jr., "A universal method for geometric correction of magnetic resonance images for stereotactic neurosurgery," *Stereotact Funct Neurosurg*, vol. 66, pp. 137-40, 1996.

[48] D. S. Cohen, J. H. Lustgarten, E. Miller, A. G. Khandji, and R. R. Goodman, "Effects of coregistration of MR to CT images on MR stereotactic accuracy," *J Neurosurg*, vol. 82, pp. 772-9, 1995.

[49] B. K. Rutt, "Vascular System MR Imaging," presented at the 1992 AAPM Summer School on The Physics of MRI, Banff, Alberta, Canada, 1992.

[50] M. J. Graves, "Magnetic resonance angiography," *Br J Radiol*, vol. 70, pp. 6-28, 1997.

[51] Y. Bercier, Patrocinio, H., Belanger, P., Hristov, D., "Multimodality Image Fusion and Localisation Environment for Radiosurgery Treatments of Large AVMs," presented at The XIIIth International Conference on The Use of Computers in Radiation Therapy, Heidelberg, 2000.

[52] Y. Bercier, Patrocinio, H., Belanger, P., Hristov, H., "Multimodality image fusion for radiosurgery localisation of large AVMs," presented at The World Congress on Medical Physics and Boimedical Engineering, Chicago, 2000.

[53] K. Otto, "3-dimensional anatomy-based verification in stereotactic radiosurgery," in *Medical Physics*. Montreal: McGill, 1997, pp. 101.

[54] C. J. Henri, D. L. Collins, and T. M. Peters, "Multimodality image integration for stereotactic surgical planning," *Medical Physics*, vol. 18, pp. 167-77, 1991.

[55] W. H. Press, Teukolsky, S.A., Vetterling, W.T., Flannery, B.P., *Numerical Recipes in C: The Art of Scientific Computing*, Second ed. Cambridge: Press Syndicate of the University of Cambridge, 1992.

[56] L. P. Adams, "X-ray stereo photogrammetry locating the precise, three-dimensional position of image points," *Med Biol Eng Comput*, vol. 19, pp. 569-78, 1981.

[57] C. J. Henri, "Application of stereoscopic digital subtraction angiography to stereotactic neurosurgery planning," in *Medical Physics Unit*. Montreal: McGill, 1989, pp. 118.

[58] G. W. Sherouse, "GRATIS," , Release 4 ed, 1992.

[59] R. L. Siddon, "Fast calculation of the exact radiological path for a three-dimensional CT array," *Med Phys*, vol. 12, pp. 252-5, 1985.

[60] T. M. Strat, "Recovering the Camera Parameters from a Transformation Matrix," in *Readings in Computer Vision: Issues, Problems, Principles, and Paradigms*, M. A. Fischler, Firschein, O., Ed. Los Altos, 1987, pp. 93-100.

[61] G. W. Sherouse, "Coordinate transformation as a primary representation of radiotherapy beam geometry [see comments]," *Med Phys*, vol. 19, pp. 175-9, 1992.

[62] G. B. Pike, E. B. Podgorsak, T. M. Peters, C. Pla, and A. Olivier, "Three-dimensional isodose distributions in stereotactic radiosurgery," *Stereotact Funct Neurosurg*, vol. 55, pp. 519-24, 1990.

[63] G. B. Pike, E. B. Podgorsak, T. M. Peters, C. Pla, A. Olivier, and L. Souhami, "Dose distributions in radiosurgery," *Med Phys*, vol. 17, pp. 296-304, 1990.